Government of Western Australia

Department of
Mines and Petroleum

REPORT
131

THE YUINMERY VOLCANOGENIC MASSIVE SULFIDE PROSPECTS: MINERALIZATION, METASOMATISM AND GEOLOGY

by LY Hassan

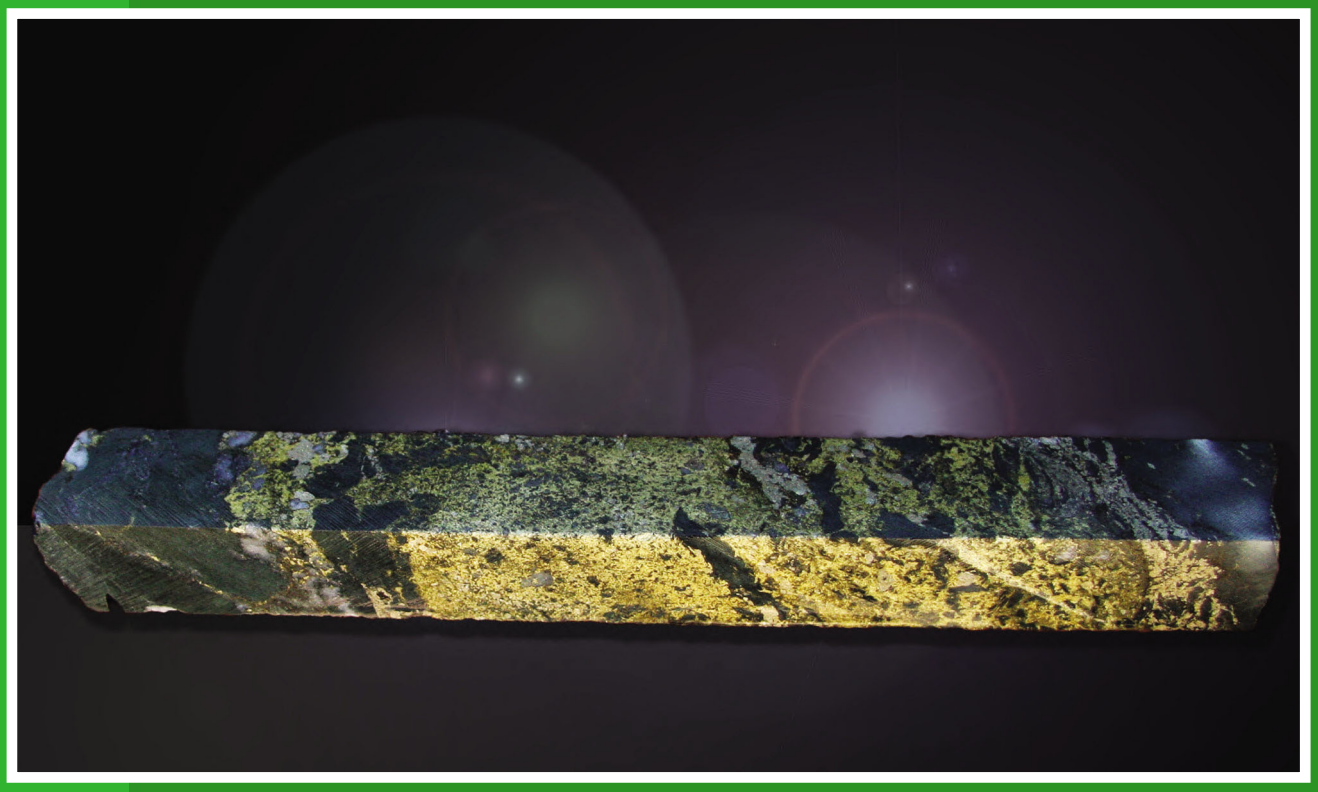

Geological Survey of Western Australia

Government of **Western Australia**
Department of **Mines and Petroleum**

REPORT 131

THE YUINMERY VOLCANOGENIC MASSIVE SULFIDE PROSPECTS: MINERALIZATION, METASOMATISM AND GEOLOGY

by
LY Hassan

Perth 2014

Geological Survey of Western Australia

MINISTER FOR MINES AND PETROLEUM
Hon. Bill Marmion MLA

DIRECTOR GENERAL, DEPARTMENT OF MINES AND PETROLEUM
Richard Sellers

EXECUTIVE DIRECTOR, GEOLOGICAL SURVEY OF WESTERN AUSTRALIA
Rick Rogerson

REFERENCE
The recommended reference for this publication is:
Hassan, LY 2014, The Yuinmery volcanogenic massive sulfide prospects: mineralization, metasomatism and geology: Geological Survey of Western Australia, Report 131, 65p.

National Library of Australia Cataloguing-in-Publication entry

Author:	Hassan, L. Y. (Lee Yvonne) 1951- author.
Title:	The Yuinmery volcanogenic massive sulfide prospects: mineralization, metasomatism and geology / L Y Hassan.
ISBN:	9781741685664 (ebook)
Subjects:	Sulfides--Western Australia. Geological surveys--Western Australia.
Other Authors/Contributors:	Geological Survey of Western Australia.
Dewey Decimal Classification:	549.32

ISSN 1834–2280

Grid references in this publication refer to the Geocentric Datum of Australia 1994 (GDA94). Locations mentioned in the text are referenced using Map Grid Australia (MGA) coordinates, Zone 50. All locations are quoted to at least the nearest 100 m.

Copy editor: K Hawkins
Cartography: A Symonds, M Prause
Desktop publishing: RL Hitchings
Printed by Images on Paper, Perth, Western Australia

Published 2014 by Geological Survey of Western Australia
This Report is published in digital format (PDF) as part of a digital dataset on USB and is available online at <www.dmp.wa.gov.au/GSWApublications>.

Further details of geological publications and maps produced by the Geological Survey of Western Australia are available from:
Information Centre
Department of Mines and Petroleum
100 Plain Street
EAST PERTH WESTERN AUSTRALIA 6004
Telephone: +61 8 9222 3459 Facsimile: +61 8 9222 3444
www.dmp.wa.gov.au/GSWApublications

Cover image: High-grade copper ore, Just Desserts deposit. Quarter drillcore from 137.4 m in diamond drillhole YD09-01; length of core 21 cm

Contents

Appendices*

---

* Appendices 1–8 are provided separately on a USB. The Report may be accessed directly on our website independently of the USB.

Figures

Tables

Plate

The Yuinmery volcanogenic massive sulfide prospects: mineralization, metasomatism and geology

by

LY Hassan

Abstract

The Yuinmery volcanogenic massive sulfide (VMS) project includes the Just Desserts deposit (where Empire Resources Ltd has reported a resource of 1.07 Mt at 1.82% Cu and 0.78 g/t Au) and the Trajan, A Zone, B Zone, C Zone, Augustus, Gamagee, and Pippin Zone (Smith Well) prospects, all of Archean age. Pyrite is the dominant sulfide in the mineralized horizons although pyrrhotite is also abundant in places. Chalcopyrite is characteristic of the higher grade ore at Just Desserts. Sphalerite, magnetite, gold and molybdenite, and bismuth, silver, gold, nickel, and cobalt tellurides are also present in the mineralized zones. The mineralization was formed in a subaqueous environment during periods of volcanic quiescence marked by the presence of chemical sedimentary rocks or exhalites and changes in the composition of the volcanic rocks. The Just Desserts, Trajan, and C Zone mineralization is hosted by calc-alkaline basalt, basaltic hyaloclastite, and banded iron-formation (BIF), which are overlain by calc-alkaline andesite. The contact can be traced along strike from Just Desserts to C Zone, which is on the heel of a syncline. A Zone may be the off-faulted northern extension of this horizon. B Zone appears associated with chemical sedimentary rocks higher up in the stratigraphy. Augustus is possibly at an equivalent stratigraphic position to B Zone, although geological relationships here are disrupted by faulting and intrusion by gabbro and pyroxenite. Recrystallized BIF at Augustus is underlain by tholeiitic basalt. Remnants of rhyolite in the gabbro suggest that the BIF at Augustus may have been overlain by rhyolite. Trace element geochemistry is consistent with the eruption of both the calc-alkaline volcanic rocks and the tholeiitic basalt in an oceanic arc-rift setting.

Textures indicate that at least some of the sulfides were deposited on the sea floor around hydrothermal vents while the chemical sedimentary rocks were still in a plastic state. Mineralization infilling the matrix of hyaloclastites and within fractures in chert may have formed in the substrate beneath the sea floor.

Iron-rich talc is the main silicate mineral associated with mineralization at Just Desserts and C Zone. It may have formed directly in the chemical sedimentary rocks from hydrothermal fluids although it also appears to replace chlorite. Chlorite is present throughout the succession, except in talc-rich zones beneath mineralization. Chlorite is a product of regional greenschist facies metamorphism, although the localized alteration of feldspars to chlorite and quartz beneath the mineralization is indicative that chlorite is also a product of alteration associated with the mineralization. The chlorite composition is a function of lithology, although in the basalts beneath the C Zone, the chlorite is more iron rich in proximity to mineralization. Other minerals associated with mineralization are quartz, Ca-poor amphiboles, minor apatite, ferroan dolomite, white and brown micas, stilpnomelane, hisingerite, and tourmaline. Cummingtonite and anthophyllite are abundant in the BIF associated with mineralization. Although the cummingtonite crystals cut across the magnetite–chert laminae, they appear to have formed and fractured while the BIF was still in a plastic state. Patchy zones of cordierite + anthophyllite ± cummingtonite ± hypersthene within the andesites and basalts appear metasomatic in origin rather than metamorphic and are interpreted as the pathways along which very hot hydrothermal fluids flowed. The mineralizing solutions were rich in magnesium, iron, silica, and sulfur. They also contained copper, zinc, lead, gold, silver, tellurium, bismuth, molybdenum, nickel, boron, carbonate, and phosphorous.

The HyLogger has proved useful for studying the alteration assemblages. A portable HyLogger could be used on drillcore and cuttings in the field as an exploration tool to pick up talc and Ca-poor amphiboles that could indicate proximity to mineralization. The possibility that mineralization has been stoped out by intrusions needs to be considered during exploration.

KEYWORDS: andesite, anthophyllite, banded iron-formation, basalt, copper, cordierite, cummingtonite, hypersthene, intrusive rocks, gabbro, gold, massive sulphide deposits, metasomatism, talc, tellurium minerals, volcanic hosted deposits, zinc

Introduction

The Yuinmery project is one of several volcanogenic massive sulfide (VMS) deposits in the Murchison region and southwest of Western Australia being studied by the Mineral Systems team of the Geological Survey of Western Australia (GSWA) with the aim of building genetic models for the environment of ore formation, and providing useful vectors for exploring in greenfields areas. The region has recently undergone 1:100 000-scale mapping by GSWA, although the present mineral systems studies are far more detailed and focused.

The Yuinmery base metal prospects straddle the Paynes Find – Sandstone Road, 475 km northeast of Perth, about 10 km west of Yuinmery Homestead (Fig. 1) in the Youanmi greenstone belt. Western Mining Corporation discovered gossan in association with outcropping chemical metasediments in 1969 (Wroe, 1976). Diamond drilling carried out by Western Mining Corporation between 1974 and 1977 yielded several significant base metal intersections, including the drillcore intercept at 36.6 m, at 0.65% Cu and 0.94 g/t Au from their Just Desserts prospect. Western Mining Corporation also intersected low-grade base metal mineralization at their Aragorn Zone (now known as A Zone), Brandywine Zone (now known as B Zone), Claudius Zone (now known as C Zone), Pippin Zone (now known as Smith Well), and Gamagee Zone (Wroe, 1976, 1978). These prospects are shown on Plate 1.

After Western Mining Corporation relinquished the tenements, exploration was carried out by Esso Australia Ltd, Black Hill Minerals Ltd, Shell Company of Australia Limited, Meekal Pty Ltd, Arboyne NL, and RGC Exploration Pty Ltd. Empire Resources Ltd commenced exploring the area in 2004 and announced a maiden indicated and inferred resource at Just Desserts of 1.07 Mt at 1.82% Cu and 0.78 g/t Au in 2009 (Empire Resources Ltd, 2009a). High-grade zinc mineralization was discovered at A Zone in addition to copper mineralization in 2011 (Empire Resources Ltd, 2011a).

In addition to the essentially stratiform base metal – gold mineralization, there are small gold workings in the area (Plate 1). The Continental, Marloo, and Lady Agnes workings produced 97.04, 6.13, and 12.88 oz Au, respectively, between 1908 and 1910. These occurrences are associated with quartz veins.

Despite the considerable amount of work by exploration companies in the area, there has been very little published on the prospect-scale geology and mineralization at Yuinmery. For the purpose of this study, Empire Resources Ltd donated diamond drillcore from five of their diamond drillholes to GSWA's core library. Hole YD09-01 was drilled for metallurgical purposes through the middle of the Just Desserts mineralization. Unfortunately, most of the mineralized zones from YD09-01 were taken for metallurgical work, although some high-grade mineralization was retained and the intervening zones provided valuable material for the study of alteration. Half or whole core was available for the full length of the other four drillholes, including mineralized zones, except where the start of the hole was drilled using a percussion rig. Holes YD09-03 and YRC10-13D were drilled to test the Just Desserts – Trajan zone at depth. Hole YRC09-01D was drilled to intersect the C Zone and YD10-01 was drilled to test the Augustus prospect. The position of these drillholes is shown on Plate 1 and significant base metal intersections are in Table 1. This drillcore was analysed using the GSWA HyLogger. Selected samples were studied petrographically and chemically to determine the nature of the host rocks and to gain an understanding of the alteration and controls on mineralization at Yuinmery.

Geology

Regional geology

The Yuinmery base metal prospects are in the northwestern Youanmi Terrane within a large, northerly plunging synform within a triangular-shaped segment of the Youanmi greenstone belt that is separated from the main part of the Youanmi greenstone belt by the Youanmi shear zone to the west, bounded to the east by the Yuinmery shear zone, and intruded by granitic rocks to the south (Stewart et al., 1983; 1:100 000-scale map, Ivanic, in prep.; Fig. 1). The greenstones include ultramafic, mafic, and felsic volcanic rocks, and are extensively intruded by mafic igneous complexes (Stewart et al., 1983; Ivanic, in prep.). The volcanic rocks are interpreted by Ivanic (in prep.) as part of the Norie Group, which is interpreted to have a date of ≥2820 to 2805 Ma (Van Kranendonk et al., 2013). The stratigraphic scheme of Wyche et al. (2013) for the northwestern Youanmi Terrane is given in Figure 2. The mafic igneous complexes are part of the Annean Supersuite (Van Kranendonk et al., 2013). The Youanmi Igneous Complex to the west of the Youanmi shear zone was assigned to the c. 2810 Ma Meeline Suite by Ivanic et al. (2010). Zircons from a fine-grained metadolerite, which may be the contact zone of the Youanmi Igneous Complex from near Freddie Well on the western side of the Youanmi shear zone, gave a concordia date of 2825 ± 7 Ma. Wingate et al. (2012) interpreted this date as the maximum age of the complex on the assumption that the zircons were incorporated from the country rock, and that the dolerite is part of the Youanmi Igneous Complex. Elsewhere in the Youanmi Terrane, the Meeline Suite intrudes the ≥2820 Ma to 2805 Ma Norie Group (Van Kranendonk et al., 2013). In the Meekatharra area, the Norie Group comprises tholeiitic and komatiitic basalt of the Murrouli Basalt overlain by felsic volcaniclastic rocks and iron-rich sediments or banded iron-formations (BIFs) of the Yaloginda Formation (Van Kranendonk et al., 2013).

There is only one published date for the part of the Youanmi greenstone belt bounded by the Youanmi shear zone and the Yuinmery shear zone. The Courlbarloo Tonalite, part of the Mt Kenneth Suite, was dated at 2813 ± 5 Ma (Cassidy et al., 2002). This tonalite intrudes both the mafic complex and the volcanic rocks in this area. Thus, this date is the minimum age of the volcanic rocks that have been assigned by Ivanic (in prep.) to the Norie Group.

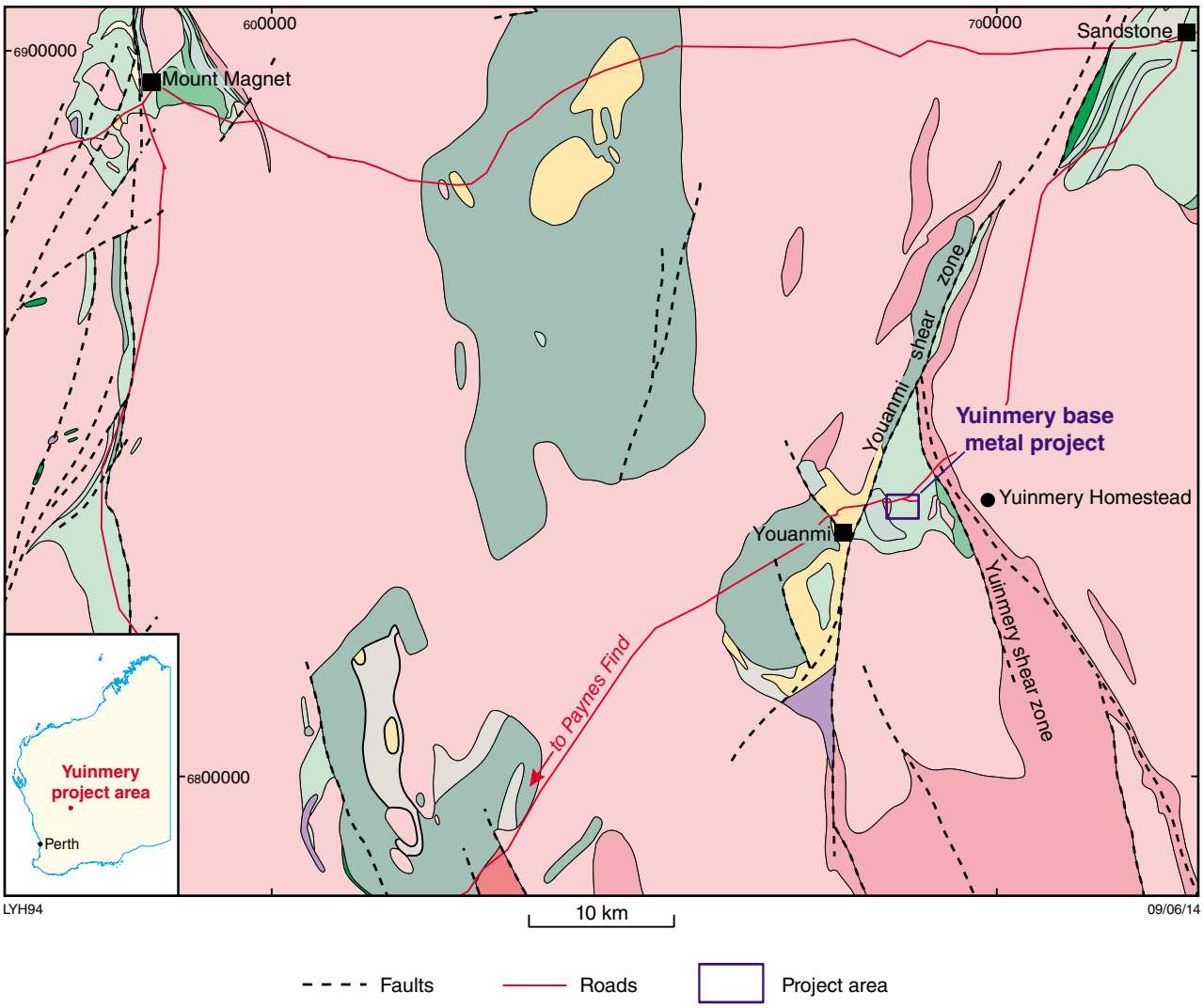

Figure 1. **Location of the Yuinmery volcanogenic massive sulfide (VMS) deposits relative to a simplified geological map of a portion of the northern Youanmi Terrane**

Metamorphic grade is typically low (low greenschist facies) except near the Yuinmery shear zone, where metamorphism is in the low amphibolite facies (Stewart et al., 1983).

Project area geology

An interpreted geological map of the project area (Plate 1) was compiled in Arc Map using georeferenced open-file company maps, drillhole information, and aeromagnetic data. Company maps included outcrop mapping by Bannister (1974, 1988) for Western Mining Corporation and Arboyne NL – Meekal Pty Ltd; Belford (1982) for Esso Australia Ltd; Richards and Elliot (1983) for Shell Company of Australia; and Watkins (1990) for RGC Exploration Pty Ltd. The area has also been recently mapped at the 1:100 000 scale as part of the GSWA mapping program (Ivanic, in prep.). Rocks in the project area are typically deeply oxidized, so that mapping of lithologies is in places inconsistent between maps. For this reason, drillhole data were particularly useful, although it was evident that different geologists logged rocks in different ways, especially the fine-grained volcanic rocks. Drillcore from five diamond holes donated by Empire Resources Ltd was logged as part of this study (Appendix 1). Empire Resources Ltd also provided data on other diamond and reverse circulation (RC) drillholes. Additional drillhole data used included diamond and percussion by Western Mining Corporation, variously logged by DF Evans, WE Bannister, AG Stevens, or M Donaldson, and reported in Western Mining Corporation (1973a), Bannister (1974), and Wroe (1976, 1978); rotary airblast (RAB), percussion and diamond drilling by Esso (Belford, 1982, 1984); RAB drilling by Shell (Richards and Elliot, 1983); and RAB drilling by RGC (Watkins, 1990). The distribution of the diamond drillcore studied and all other drillholes used is shown on Plate 1.

Table 1. Significant intersections in the Yuinmery diamond drillcore studied and drillhole collar coordinates

Significant intersections

Drillhole	*Core from (m)*	*Core to (m)*	*Length (m)*	*Cu (%)*	*Zn (%)*	*Source*
YD09-01	66.30	76.70	10.4	2.40	–	1
YD09-01	105.65	108.60	2.95	3.37	–	1
YD09-01	115.70	120.90	5.20	3.30	–	1
YD09-01	136.45	142.90	6.45	1.43	–	1
YD09-03	392.30	404.80	12.50	0.70	–	2
YRC10-13D	373.35	373.55	0.20	5.18	0.48	3
YRC10-13D	402.75	405.75	3.00	1.46	–	3, 4
YD09-01D	250.90	251.90	1.00	0.26	0.65	4
YD09-01D	260.40	261.80	1.40	0.73	–	4
YD10-01	261.81	262.45	0.64	1.05	–	5
YD10-01	269.40	269.78	0.38	3.44	–	5
YD10-01	279.68	280.38	0.70	1.22	–	5

NOTE: – assayed; not considered significant by Empire Resources Ltd

SOURCES: 1 Empire Resources Ltd (2009a)
2 Empire Resources Ltd (2010a)
3 Empire Resources Ltd (2011b)
4 Empire Resources Ltd (2011, written comm. 1 July) Yuinmery database dated May 2011
5 Empire Resources (2010b)

Drillhole collar coordinates

Drillhole	*Northing*	*Easting*	*RL*	*Az*	*Dip*
YD09-01	6837044	685820	470.0	225	–70
YD09-03	6837095	686143	470.0	225	–60
YRC10-13D	6836965	686285	470.0	225	–60
YRC09-01D	6836345	686620	470.0	180	–75
YD10-01	6837136	687774	470.0	220	–70

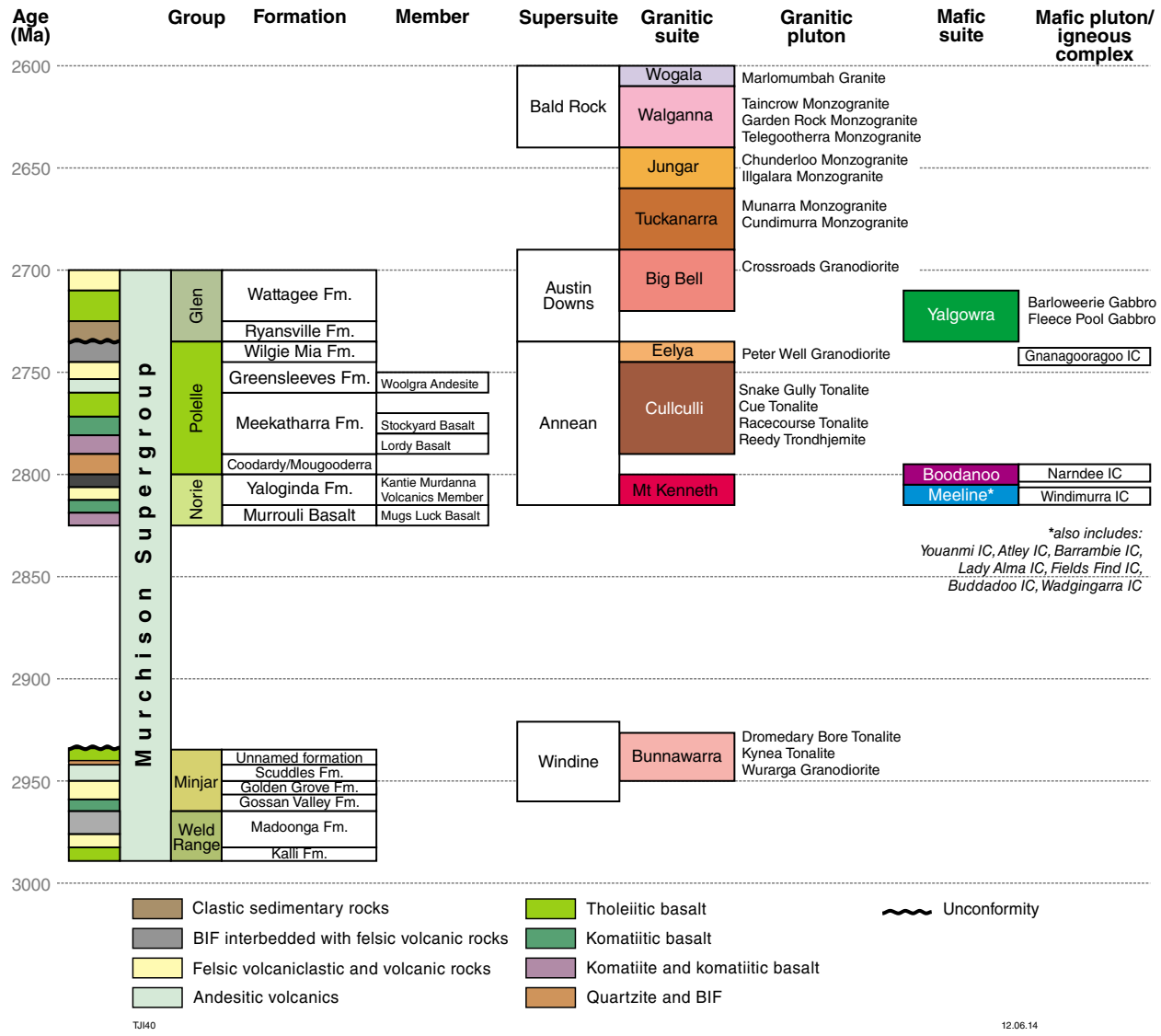

Figure 2. Stratigraphic scheme for the northern Youanmi Terrane (after Wyche et al., 2013)

Empire Resources Ltd (2012) produced an interpreted solid geological map of the project area. Although this map is largely diagrammatic and could not be properly georeferenced, it provided a useful starting point. The Empire Resources Ltd (2012) map shows the volcanic rocks above the main mineralized zone as 'upper felsic volcanics' and the volcanic rocks below the main mineralized horizon as 'lower felsic volcanics'. In this report, these volcanic rocks are informally called 'upper volcanics' and 'lower volcanics', respectively, because geochemistry has indicated that the lower volcanics are predominantly basalts, as discussed below.

Gabbro, pyroxenite, and granophyre intrude the volcanic rocks (Wroe, 1976). Ivanic (in prep.) interprets about two-thirds of the project area as underlain by a mafic-ultramafic complex. The distribution of gabbro, as determined from company outcrop mapping and drillhole data, is quite extensive (Plate 1) and could be even more extensive than shown in areas of no outcrop and where no drillhole information was available. However, the studied drillholes and numerous other company drillholes in the area suggest the mafic-ultramafic complex is less extensive than shown by Ivanic (in prep.), especially near mineralization where he shows it as the host of all prospects except the A Zone.

The close association of base metal mineralization with chemical sedimentary rocks including chert and BIF was first recognized by Western Mining Corporation (Wroe, 1976). These chemical sedimentary rocks are called 'exhalite' by Empire Resources Ltd (2012). Exhalites were defined by Ridler (1971) as chemical sedimentary rocks of predominantly volcanic origin. At Just Desserts, there are three closely spaced outcropping horizons of gossanous chert. The chert and BIF outcrops and drillhole

intersections are sufficiently continuous to show that the Just Desserts, Trajan, and C Zone are at roughly the same stratigraphic level. Empire Resources Ltd (2012) interpreted the A Zone as an off-faulted extension of the Just Desserts horizon. Empire Resources Ltd (2012) interpreted B Zone as a separate mineralized horizon higher up in the sequence, which they also interpret to host their Augustus prospect. The Pippin Zone (Smith Well) has been interpreted as an extension of the Gamagee Zone (Wroe, 1976) although it is unclear whether the Pippin Zone and Gamagee Zone are on a faulted extension of the Just Desserts horizon, which has been offset to the north (Plate 1), or whether they are the B Zone, which has been offset to the south. The boundary between the upper and lower volcanics in the northeastern part of the area is also uncertain, although it is shown on Plate 1 in the approximate position given by Empire Resources Ltd (2012).

Descriptions of the volcanic rocks and associated chemical sedimentary rocks, and of the intrusive rocks, are given below. The logs of the studied diamond drillholes on which these descriptions are based are given in Appendix 1. Sample numbers are given for all samples that were studied microscopically. Those that were also analysed are marked with an asterisk.

Lower volcanics

Volcanic rocks in the Just Desserts – Trajan – C Zone area

Where least altered, at some distance below mineralization in the Just Desserts, Trajan, and C Zone area, the lower volcanics are massive, coherent, dark greenish grey, fine-grained rocks. Under the microscope, some show randomly oriented plagioclase laths and fine-grained ilmenite and have tiny amygdales filled with cummingtonite and chlorite (Fig. 3). Others are microcrystalline or consist of chlorite and dusty opaques after glass. In places, there are zones with macroscopically visible amygdales (Fig. 4). The amygdales typically consist of quartz although some also contain chlorite, fibrous amphiboles, or oxides. The amygdaloidal zones are commonly overlain by rocks with vague brecciated texture (Fig. 4a), which are interpreted as chilled flow-top breccias or autobreccias. Extensive zones of breccia are present in the lower volcanics, especially in the upper part beneath and between the mineralized zones. These breccias are typically monolithic and commonly have a jigsaw fit (Fig. 5). They are interpreted as hyaloclastites, although an origin by hydraulic fracturing cannot be ruled out. Hyaloclastites are indicative of a subaqueous environment of extrusion and are commonly mistaken for pyroclastics in the host-rock successions of VMS deposits (Cas, 1992).

Most of the lower volcanics in the studied drillholes, including some very altered volcanic rocks and hyaloclastites, plot as basalt on the volcanic discrimination diagram of Pearce (1996), with only one sample (from YD09-03) plotting just over the boundary in the andesite – basaltic andesite field (Fig. 6; methods used are discussed in the Geochemistry section and analyses are given in Appendix 2). This was a surprising result considering that these rocks had been logged and mapped as acid volcanic rocks and acid tuff breccias by Bannister (1974), interpreted on a 1:250 000-scale map as felsic volcanics (Stewart et al., 1983) and mapped as Lower felsic volcanics by Empire Resources Ltd (2012). Ivanic (in prep.) also mapped felsic volcanic rocks at the A Zone and to the west of Just Desserts and assigned them to the Yuinmery Volcanics Member of the Yaloginda Formation of the Norie Group. A probable reason for the misidentification is that the rocks are very fine grained and typically altered, making identification difficult in fresh drillcore and almost impossible in weathered surface samples. It is worth noting that fine-grained mafic rock was logged by M Donaldson in percussion hole MYMP 13 drilled to the south of the Gamagee Zone (Western Mining Corporation Ltd, 1973a); therefore, basalt could be widespread in the lower volcanic rocks. Belford (1982) mapped the volcanic rocks in the upper part of the lower volcanics predominantly as andesites and 'dacitic to andesitic ash falls', and those in the lower part of the lower volcanics as 'rhyolitic to dacitic ash flows'. None of the studied drillholes went deep enough to test these 'rhyolitic to dacitic ash flows'. One outcrop that was mapped by Belford (1982) as 'rhyolitic to dacitic ash flows' was checked in the field. These rocks are very ferruginous with a moderate to strong cleavage (sample location LYHYUI000024, MGA 685473E 6836557N; Plate 1; Fig. 7) and are best described as oxidized chloritic schist of uncertain protolith.

No rocks from the lower volcanics that could be unequivocally called pyroclastics were seen in drillcore, although some laminated rocks interbedded with the chert and BIF may be waterlain tuffs or volcaniclastic sedimentary rocks. Altered foliated rock from near the end of diamond drillhole YD09-03 contains wispy chloritic areas that are possibly after glass shards (Fig. 8), although this rock could be sheared basalt. Although this foliated rock now contains abundant quartz, abundant fine-grained ilmenite and leucoxene indicate that it originally had a mafic chemistry. The quartz could be the result of silicification or may be sheared, quartz-filled amygdales. There is poor surface exposure of oxidized conglomerate, with rounded fragments of uncertain original composition in fine-grained matrix to the southwest of Just Desserts at sample location LYHYUI000025 (MGA 685407E 6836506N; Plate 1; Fig. 9). This conglomerate may be a reworked volcanic breccia although alternatively it could be a debris-flow deposit formed as a result of syn-depositional faulting. A volcanic breccia with a rounded cobble of chert from near A Zone at sample location LYHYUI000017 (MGA 685522E 6838478N; Plate 1; Fig. 10) possibly resulted from a basaltic lava that picked up a chert cobble.

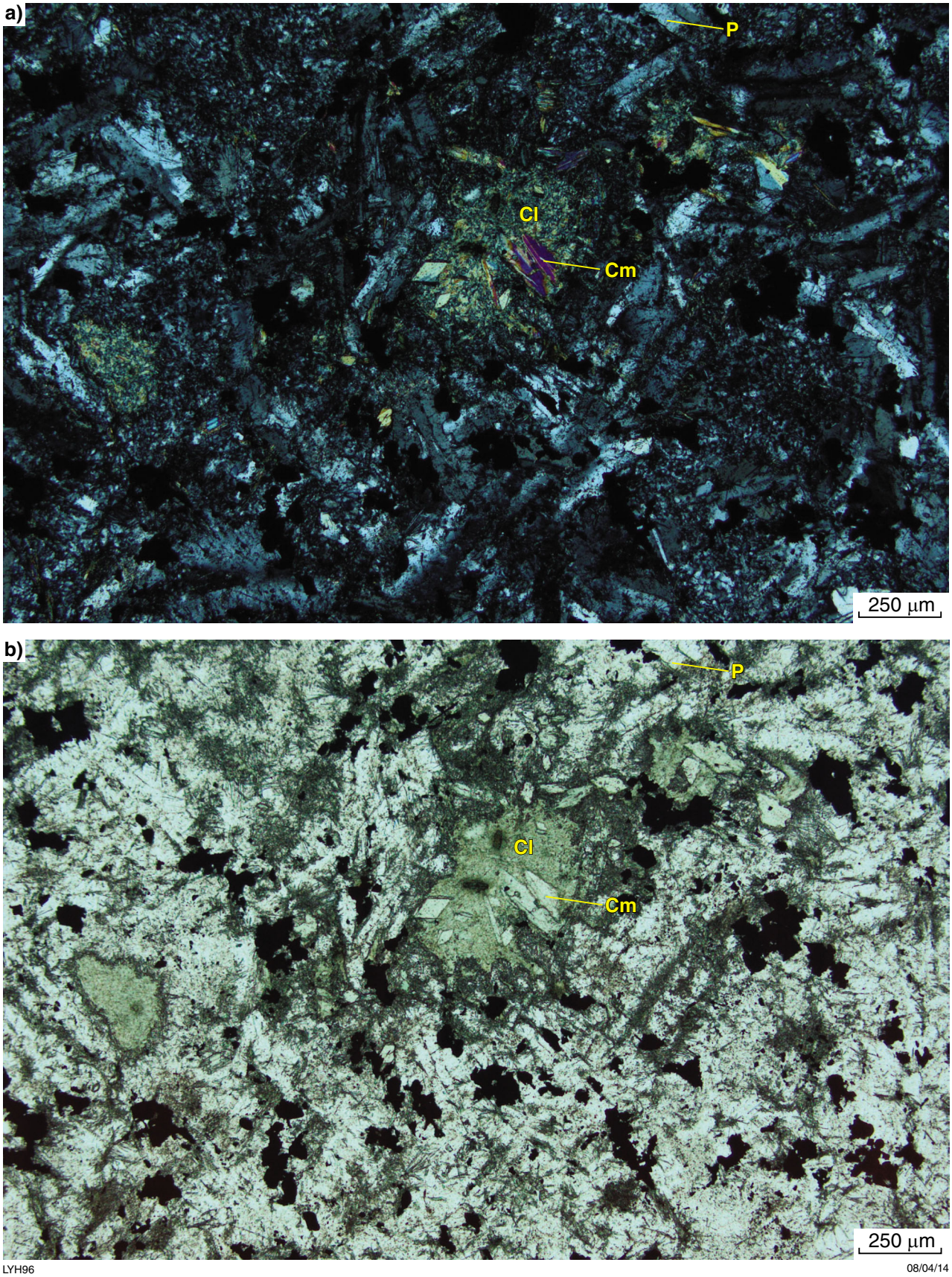

Figure 3. **Basalt with randomly oriented plagioclase laths (P) and aggregates of cummingtonite (Cm) and chlorite (Cl) that appear to infill tiny amygdales (GSWA 206873 from 301.4 m in YRC09-01D): a) plane-polarized light; b) crossed polars**

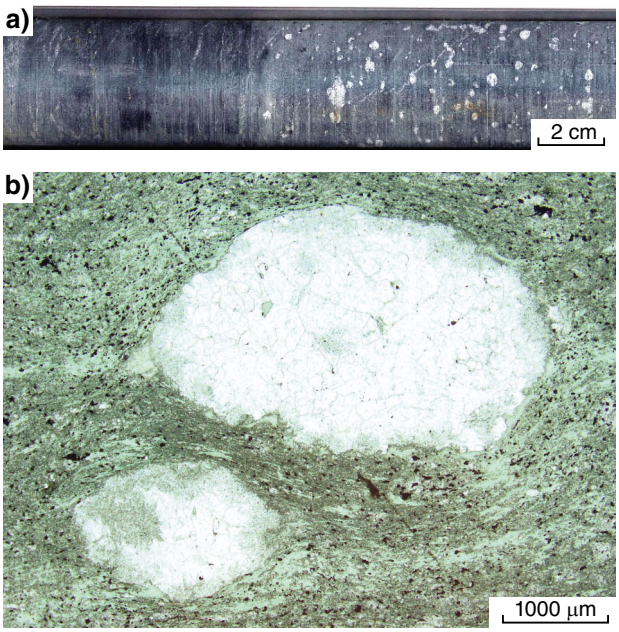

Figure 4. **Amygdaloidal basalt with amygdales filled with quartz overlain by breccia, interpreted as glassy flow-top breccia (GSWA 208064 from 412.9 m in YRC09-03): a) drillcore; b) plane-polarized light**

Figure 5. **Hyaloclastite (GSWA 20859 from 401.3 m in YD09-03)**

Chemical sedimentary rocks

Chemical sedimentary rocks are characteristic of the upper part of the lower volcanic rocks. They consist of finely laminated magnetite and chert layers alternating with carbonate laminae and silicate-rich layers (Fig. 11). The chert layers have laminae of relatively coarse-grained recrystallized quartz alternating with laminae of fine-grained quartz that in places has fine, dusty magnetite defining the laminae (Fig. 12). The silicate-rich layers are composed of various amounts of chlorite, talc, anthophyllite, and fine-grained quartz, and are interpreted as silicate-facies BIF either derived from fine-grained, waterlain tuff, or directly precipitated as gels from mineral-rich volcanic emanations. The chemical sedimentary rocks commonly show folding and brecciation interpreted as due to syndepositional slumping (Fig. 11). Figure 13 is a scanned thin section of a breccia showing a fragment of chloritic rock with thin magnetite laminae that was apparently in a plastic state when it was slump folded and incorporated in the breccia. Sulfides and quartz form the matrix to the breccia. Sulfides can also be seen forming the matrix of the breccia in the middle of the second row of core in Figure 11. The sulfides are discussed further in the section on mineralization.

Upper volcanics

Volcanic rocks in Just Desserts – Trajan – C Zone area

Belford (1982) mapped most of the upper volcanics as dacitic–andesitic ash falls. The upper volcanics in the drillcore studied from the Just Desserts – Trajan and C Zone areas are typically massive, coherent, microcrystalline greenish grey rocks that, in places, contain abundant amygdales that indicate they were lavas (Fig. 14). There are also zones of breccia with angular to curvilinear fragments ranging from several centimetres to just a few millimetres across (Fig. 15). Although it is possible that these breccias are pyroclastics, many have a jigsaw fit, suggesting that they are hyaloclastites. Massive coherent volcanic rocks and interpreted hyaloclastites from the upper volcanics in the Just Desserts – Trajan and C Zone areas plot in the andesite – basaltic andesite field of Pearce (1996) and are distinctly more evolved than the lower volcanics in this drillcore (Fig. 6; methods used are discussed in the Geochemistry section and analyses are included in Appendix 2).

Volcanic rocks in Augustus area

Superficially, some of the volcanic rocks intersected in drillhole YD10-01 from the Augustus prospect resemble those described above; they are massive, fine-grained, grey rocks, although chemically and petrographically, they are different from both the lower volcanics and upper volcanics described above. The example from 295.6 m illustrated in Figure 16 has small phenocrysts of a colourless amphibole in a matrix of tabular plagioclase, quartz, and chlorite with fine-grained disseminated oxides (Fig. 16a,b). In places, it has small amygdales filled with quartz and sulfides (Fig. 16c). It plots as a basalt on the discrimination diagram of Pearce (1996) although it is less alkaline than the basalts from the lower volcanics (Fig. 6; analyses are included in Appendix 2).

Altered breccias at the end of YD10-01 have been logged as possible mafic lapilli tuffs; alternatively, they could be tectonically brecciated and intensely altered basalts related to syndepositional faulting.

The only felsic rock in the studied drillcore is a possibly remanent, 3 m-thick interval within gabbro in YD10-01. It has phenocrysts of albite (Fig. 17a) and rounded quartz (Fig. 17b) in a matrix of fine-grained quartz, albite, and white mica; spherulites are developed in places (Fig. 17a).

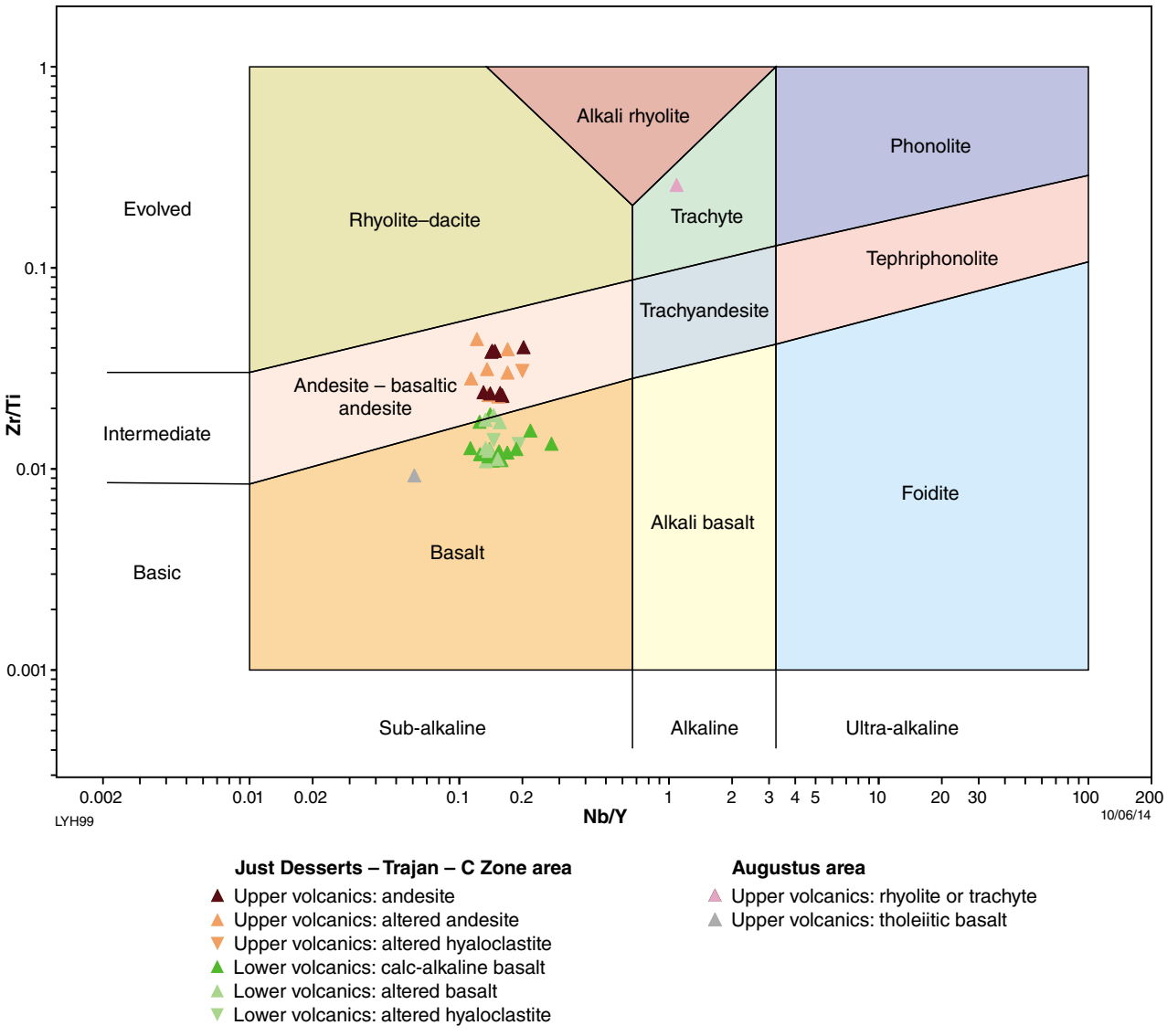

Figure 6. **Rocks of the upper and lower volcanics plotted on the volcanic discrimination diagram of Pearce (1996)**

Figure 7. **Outcropping ferruginized volcanic rocks from the lower part of the lower volcanics southwest of Just Desserts at site LYHYUI000024**

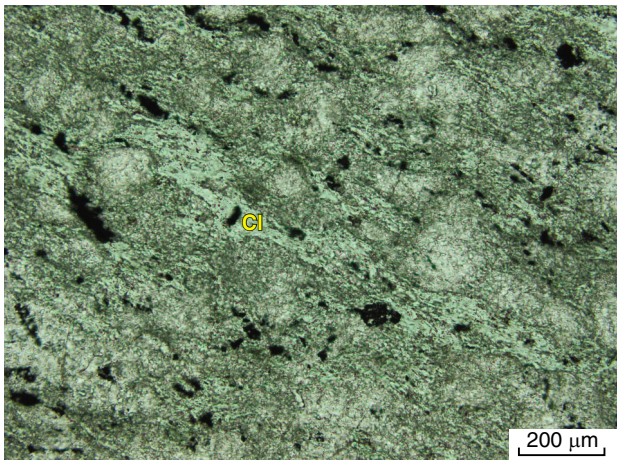

Figure 8. **Possible tuff with chlorite (Cl) after glass shards; alternatively, possible sheared basaltic rock (GSWA 208074 from 469.7 m in YD09-03); plane-polarized light**

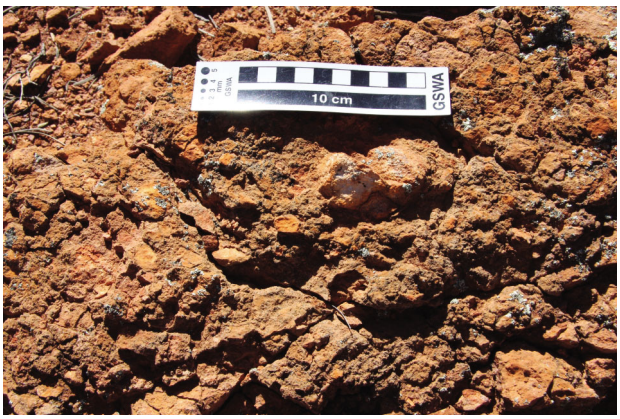

LYH102 25/03/14

Figure 9. **Conglomerate with rounded fragments in fine-grained matrix from the lower part of the lower volcanics southwest of Just Desserts at site LYHYUI000025**

LYH103 25/03/14

Figure 10. **Breccia with rounded cobble of chert from the upper part of the lower volcanics near A Zone at site LYHYUI000017**

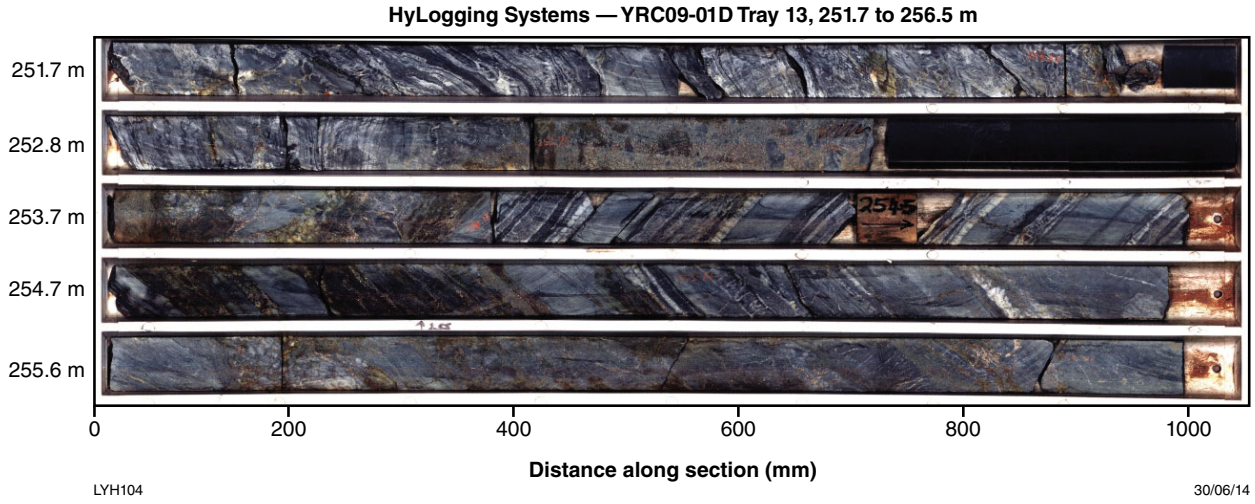

LYH104 30/06/14

Figure 11. **Drillcore from YRC09-01D, C Zone, showing chemical sedimentary rocks consisting of finely laminated magnetite and chert layers alternating with greenish grey silicate-rich layers. In places, layers show folding (right hand half of top row) and brecciation (beginning of top row), interpreted as caused by slumping. Sulfides form the matrix to the breccia in the central part of the second row.**

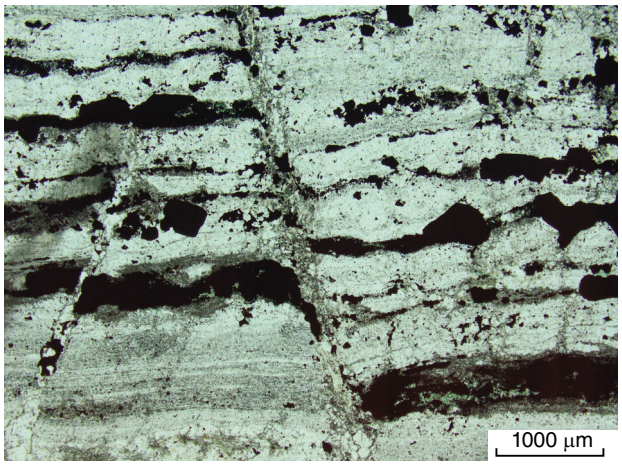

LYH105 08/04/14

Figure 12. **Chert-rich layer (GSWA 208129, 254.2 m in YRC09-01D, C Zone); plane-polarized light; note thin magnetite laminae and dusty magnetite in some of the chert laminae.**

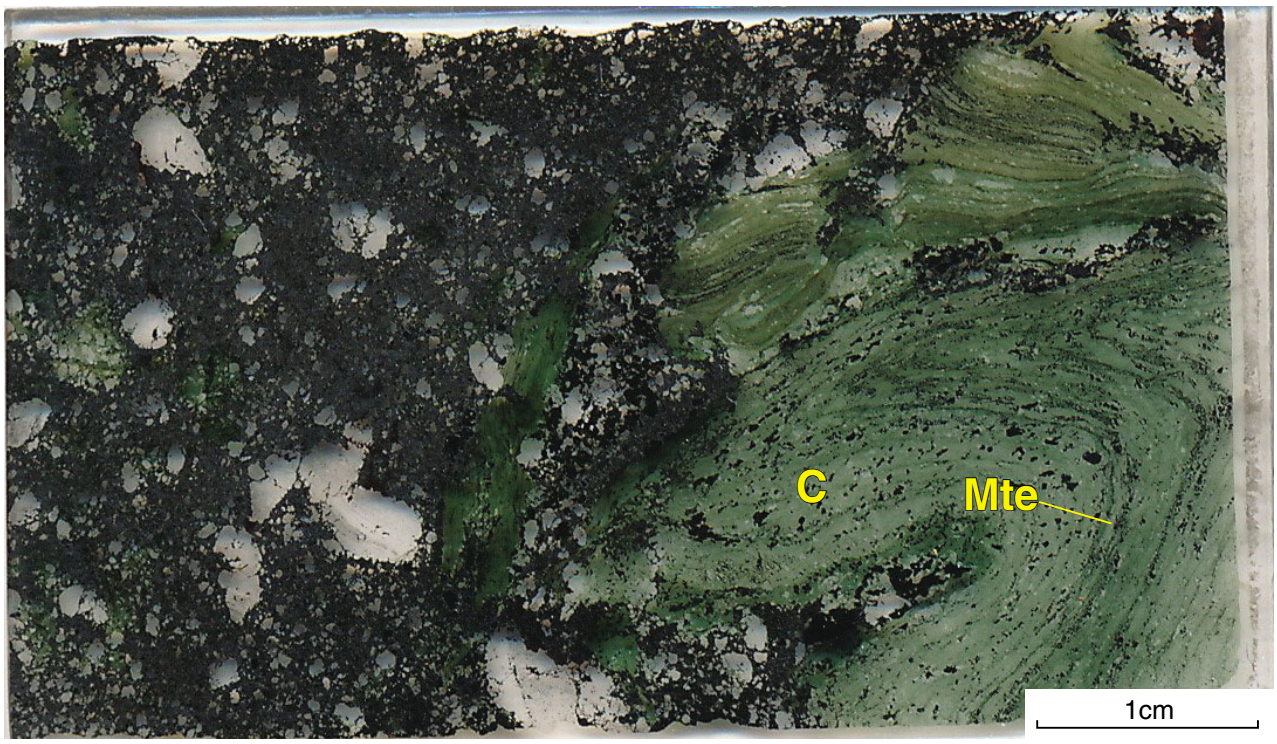

Figure 13. **Scanned thin section of a breccia showing a fragment of siliceous chloritic rock (C) with thin magnetite (Mte) laminae; the rock was apparently in a plastic state when it was slump folded and incorporated in the breccia, possibly on the side of a hydrothermal vent. Sulfides (opaque) and quartz (clear) form the matrix to the breccia (GSWA 208126 from 251.3 m in YRC09-01D, C Zone).**

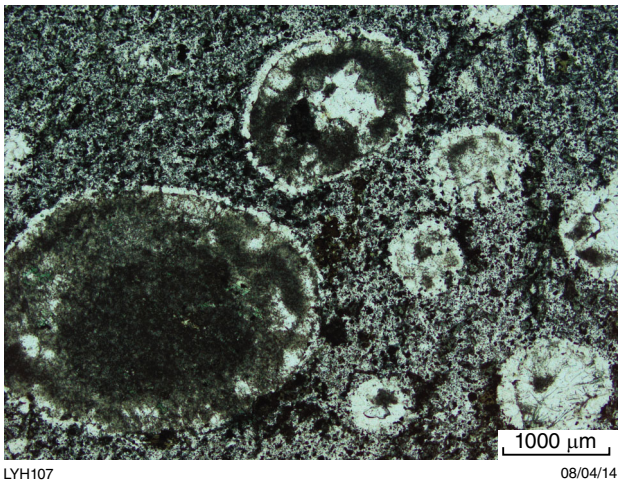

Figure 14. **Amygdaloidal andesite (GSWA 20835 from 119.4 m in YD09-03); plane-polarized light**

The contact between this rock and the gabbro is sharp but ragged and the rock appears invaded by the gabbro (Fig. 17c), suggesting that this rock pre-dated the gabbro and was not intruded. It could either be a remnant of rhyolite that was not completely stoped out by gabbro, or a very large xenolith. This rock plots as a trachyte on the discrimination diagram of Pearce (1996). However, the HyLogger did not detect any alkali feldspar, so, if it were present, it has been replaced by albite. Furthermore, this rock contains 73.7% SiO_2 (Appendix 2), and even if some of this silica were introduced, the presence of quartz phenocrysts suggests that the rock originally contained more than 20% quartz and is therefore a rhyolite (using the classification of Le Maitre, 2002).

Chemical sedimentary rocks in Augustus area

Two small intervals of recrystallized BIF composed of magnetite laminae with interstitial ferroan dolomite alternating with quartz – ferroan dolomite – chlorite laminae (Fig. 18) were intersected in drillhole YD10-01. These are separated by an interval composed of semimassive sulfides, medium-grained magnetite, carbonate, and quartz interstitial to ragged areas of mafic rock (Fig. 19). Leucogabbro or dolerite overlies and underlies the BIF and sulfide-rich interval. The sulfides may be original VMS mineralization, which, along with the BIF, has been intruded by leucogabbro or dolerite; alternatively, the sulfides could represent later hydrothermal mineralization related to the quartz vein.

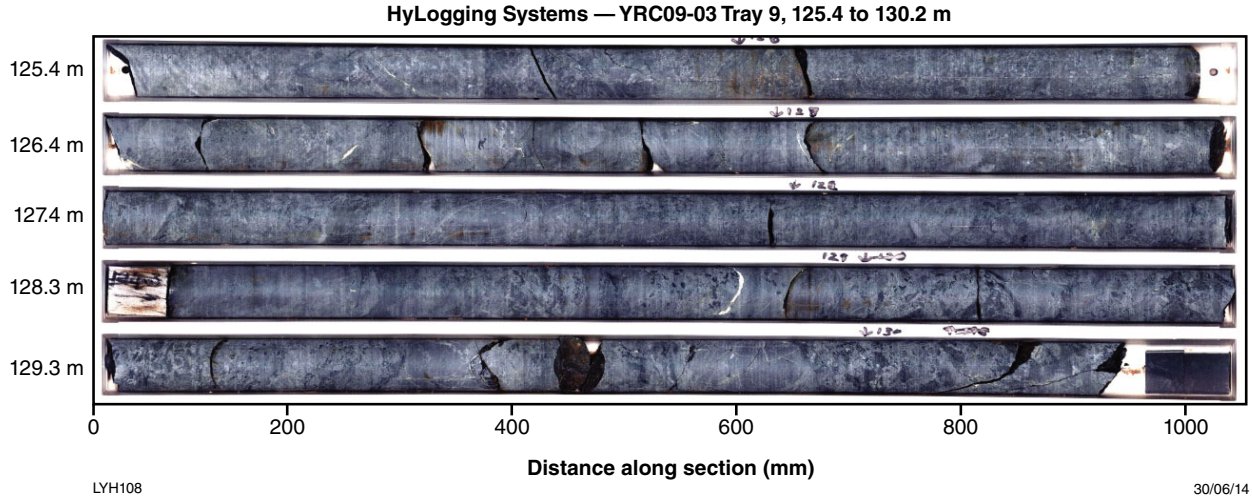

Figure 15. Drillcore from YD09-03 (125.4 – 130.2 m), showing breccia with variable size fragments, many with jigsaw fit, interpreted as hyaloclastite

Intrusive rocks

Gabbro and pyroxenite

Coarse-grained pyroxenite was intersected in diamond drillcore YD10-01 near the Augustus prospect and was also observed on the dumps of the Marloo workings. The pyroxenite consists predominantly of large clinopyroxene plates that have now been partially replaced by amphiboles, although the typical pyroxene cleavage in two directions almost at right angles has been preserved (Fig. 20). There is also minor primary hornblende with typical amphibole cleavage at angles of about 56° and 124° (Fig. 20), orthopyroxene and, in places, magnetite, although very little if any feldspar.

There is a sharp, irregular contact between the pyroxenite and a fine- to medium-grained gabbro (Fig. 21). There is no obvious sign of chilling in either rock type, suggesting either co-emplacement of the pyroxenite and gabbro, or that the gabbro intruded the pyroxenite when the pyroxenite was still hot.

Both the upper volcanics and the lower volcanics have been intruded by gabbro, which is particularly extensive in the upper volcanics (Plate 1). The gabbro is irregular in form and appears to have intruded the volcanic rocks at several levels. The gabbro varies from fine to medium grained, to coarse grained. Where intersected in YD10-01 near the Augustus prospect, the gabbro consists of altered, blocky, zoned plagioclase crystals with interstitial hornblende or ferrohornblende and various amounts of oxides, and is in sharp contact with pyroxenite (Fig. 21). Where intersected near the Just Desserts prospect in YD09-03, the gabbro is composed of plagioclase laths subophitically enclosed in hornblende or ferrohornblende, with minor quartz and accessory oxides (Fig. 22).

Leucogabbro, quartz gabbro, quartz dolerite, and quartz diorite

Rocks that have been variously logged as leucogabbro, quartz gabbro, quartz dolerite, quartz diorite, and ‘intermediate intrusive’ have been mapped separately from gabbro on Plate 1, although they are closely associated with gabbro in many places. They are most abundant in the lower volcanics and close to the contact between the upper volcanics and lower volcanics. Those in the southern part of Plate 1, which were mapped by Watkins (1990) as quartz diorite, may be part of the layered mafic intrusive but, alternatively, could be related to the granite.

Granophyre

A laterally continuous granophyre is closely associated with the mineralized horizons in the Just Desserts – Trajan area. It consists of granophyric intergrowth of quartz and feldspar and randomly oriented plagioclase crystals (Fig. 23). The granophyre was intersected in diamond drillholes YD09-01, YD09-03, and YRC10-13D. It was also intersected by the Western Mining Corporation drillholes in this area (Bannister, 1974). In YD09-01, the granophyre has intruded the hyaloclastites between the main mineralized zones. In YD09-03 and YRC10-13D, the granophyre appears to have stoped out the upper mineralized horizon and thus has had a significant economic impact due to decreased tonnage of mineralization.

Dolerite

In YD10-01, the gabbro has been intruded by fine-grained dolerite with blocky plagioclase crystals that originally may have been zoned, although the plagioclase crystals have now been partially replaced by chlorite with clear rims remaining (Fig. 24).

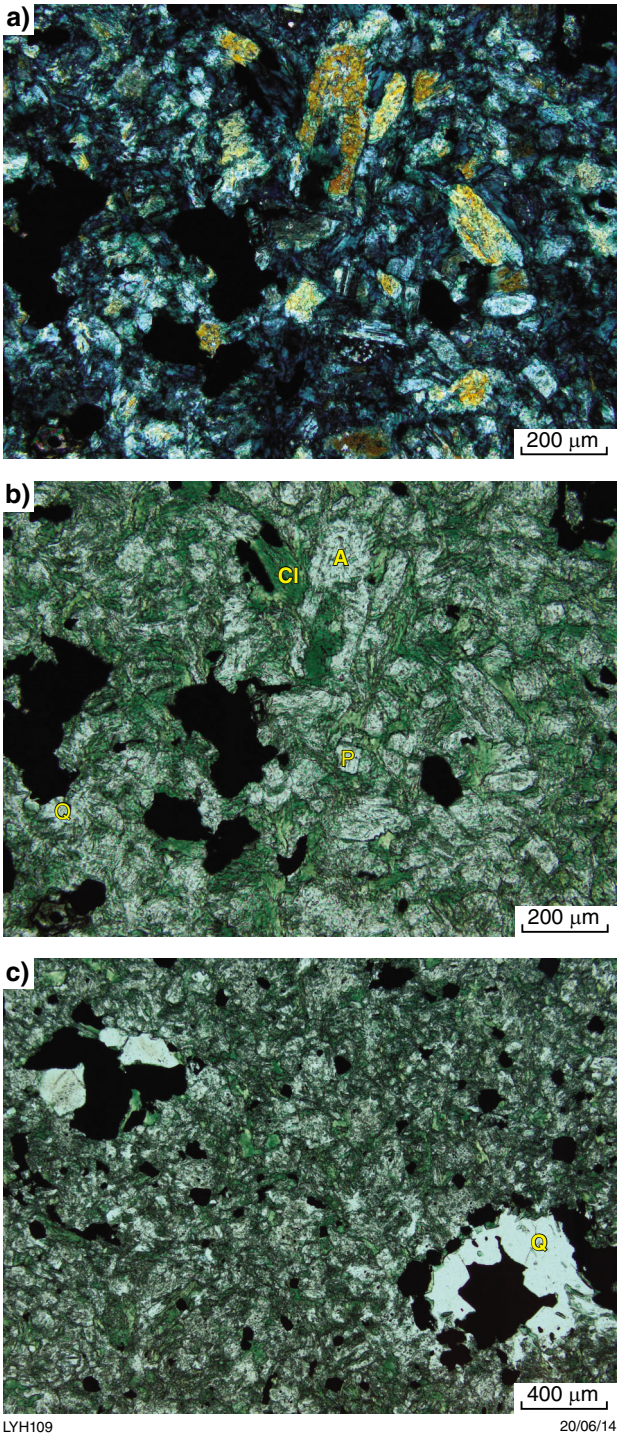

Figure 16. **Basalt (GSWA 208110 from 295.6 m in YD10-01) with small phenocrysts of colourless amphibole (A) in a matrix of tabular plagioclase (P), quartz (Q), and chlorite (Cl) with fine-grained disseminated oxides: a) crossed polars; b) plane-polarized light; c) amygdales filled with quartz and sulfides; plane-polarized light**

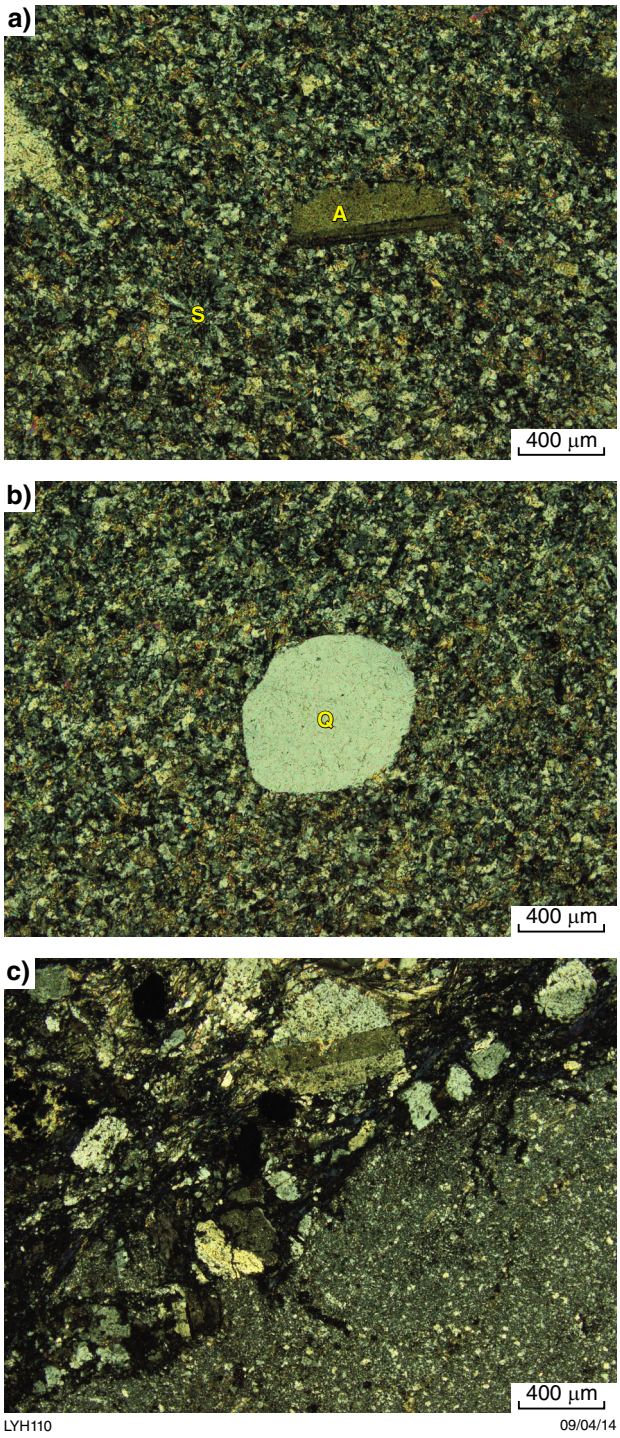

Figure 17. **Rhyolite: a) GSWA 208089 from 161.5 m in YD10-01 showing albite phenocryst (A) and spherulite (S) in fine-grained groundmass of quartz, albite, and muscovite; crossed polars; b) as above showing spheroidal quartz phenocryst (Q); crossed polars; c) GSWA 208090 from 162.5 m in YD10-01 showing irregular contact between rhyolite and gabbro; the gabbro appears to invade the rhyolite, suggesting that the gabbro post-dates the rhyolite; crossed polars**

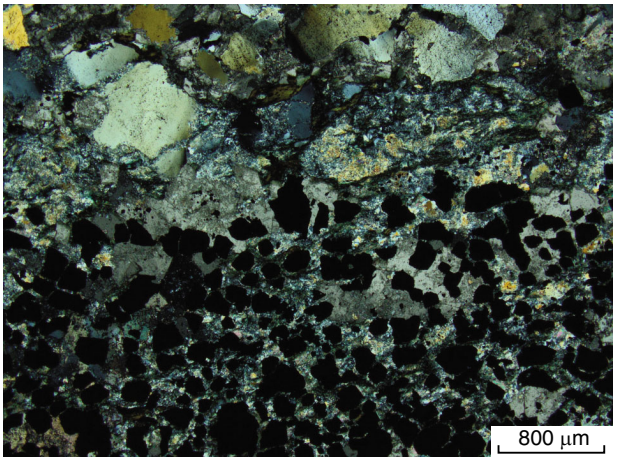

LYH111 20/06/14

Figure 18. Recrystallized banded iron-formation (BIF) from the Augustus area (GSWA 208104 from 271.7 m in YD10-01); crossed polars

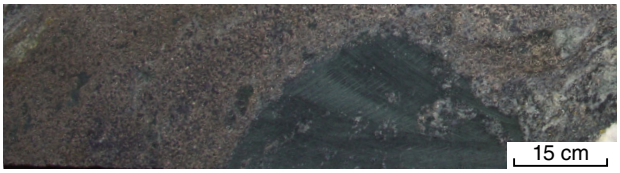

LYH112 20/06/14

Figure 19. Semi-massive sulfides, magnetite, carbonate, and quartz interstitial to ragged areas of mafic rock (GSWA 208103 from 270.5 m in YD10-01)

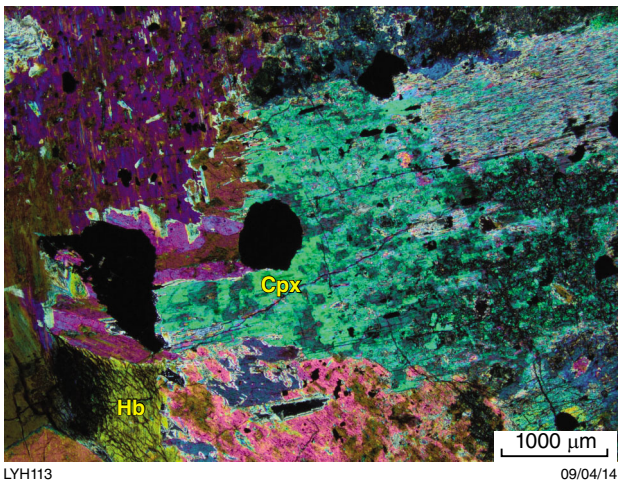

LYH113 09/04/14

Figure 20. Pyroxenite with large plates of clinopyroxene (Cpx) partially replaced by actinolite (note two directions of cleavage almost at right angles), with small crystal of hornblende (Hb) with typical amphibole cleavage (GSWA 208079 from 62.9 m in YD10-01); crossed polars

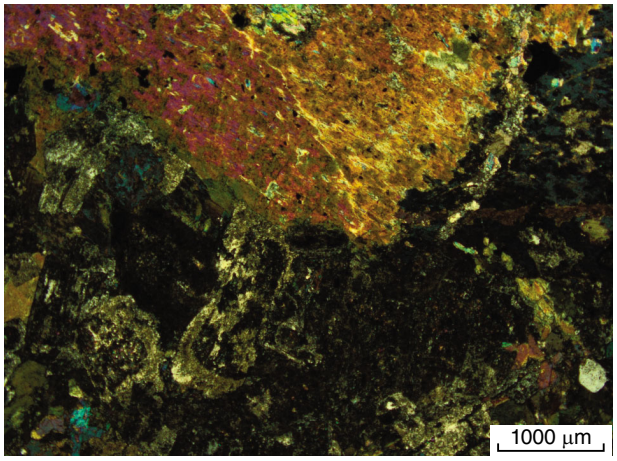

LYH114 08/04/14

Figure 21. Contact between coarse-grained pyroxenite and fine-grained gabbro (GSWA 208084 from 118.1 m in YD10-01); crossed polars

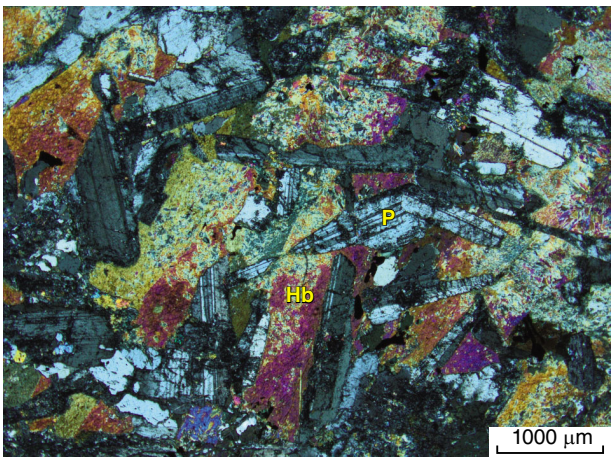

LYH115 09/04/14

Figure 22. Gabbro with plagioclase (P) subophitically enclosed by partially altered blue-green hornblende (Hb) (GSWA 208043 from 230.5 m in YD09-03); crossed polars

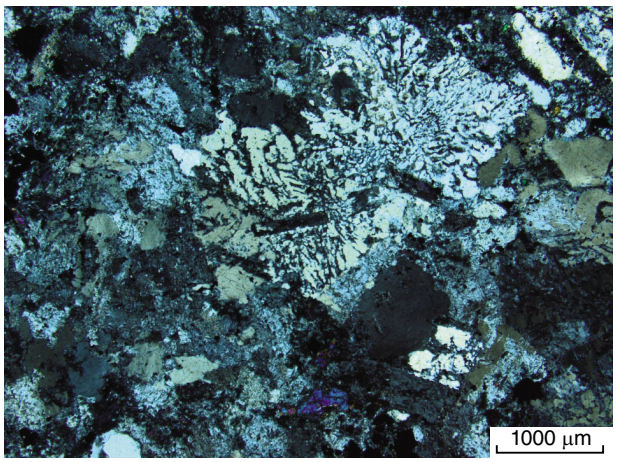

LYH116 08/04/14

Figure 23. Granophyre (GSWA 208048 from 267.2 m in YD09-03); crossed polars

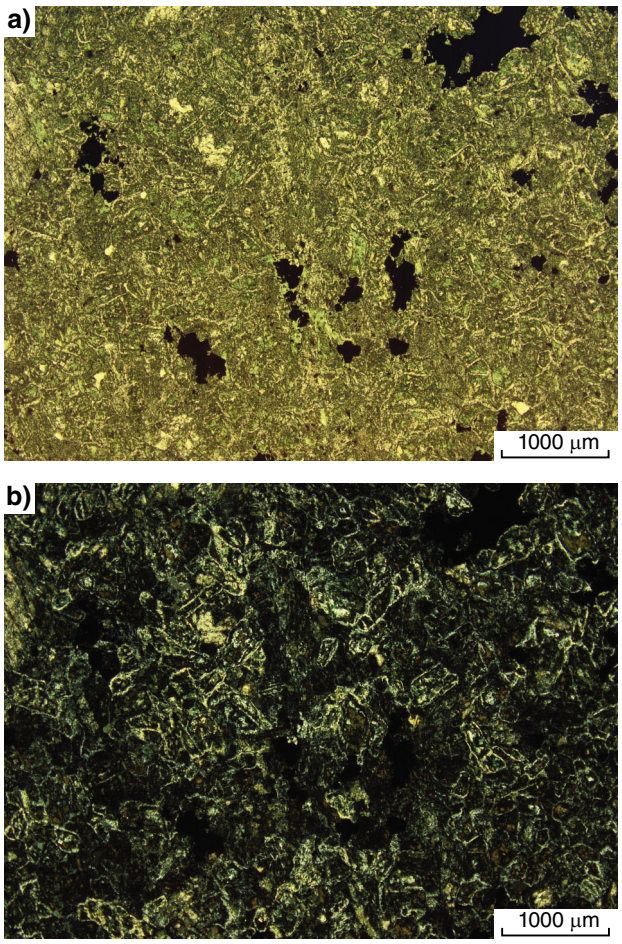

Figure 24. Dolerite with abundant blocky ?zoned feldspars with cores altered to chlorite, and clear rims (GSWA 208097 from 258.0 m in YD10-01): a) plane-polarized light; b) crossed polars

Felsic porphyry

Felsic porphyries were mapped by Watkins (1990) in the northeastern part of the area and aplites were mapped by Belford (1982) and Bannister (1988) in the southwestern part of the area. None was noted in the studied drillcore.

Intrusive andesite

A fine-grained, brownish-grey rock has intruded the basalt above and below the lowest mineralized zone in diamond drillhole YD09-01. The contacts are sharp but irregular. This rock plots as an andesite – basaltic andesite on the volcanic discrimination diagram of Pearce (1996) (Fig. 6). It contains phenocrysts of green hornblende that have been largely replaced by brown ferrohornblende in a matrix of cloudy plagioclase laths and fine-grained prismatic brown ferrohornblende (Fig. 25). In places there is minor quartz and fine-grained corroded subhedral magnetite crystals.

This intrusive andesite is difficult to distinguish visually from the basalt in drillcore although it has a slightly brownish hue relative to the greenish grey of the basalt. The intrusive andesite can be clearly distinguished from the basalt in the HyLogger summary plot by its markedly higher plagioclase content (see Hydrothermal alteration and metasomatism, below). As discussed in the Geochemistry section, the andesite also has very different trace element chemistry from the basalt. Like the granophyre, this intrusive andesite may have stoped out mineralization.

Mineralization

Just Desserts – Trajan – C Zone

In the Just Desserts – Trajan – C Zone areas, sulfides are associated with both chemical sedimentary rocks and hyaloclastites between the chemical sedimentary horizons. In the chemical sedimentary rocks, sulfides are present in layers conformable with the laminae, as crosscutting veinlets and infilling the matrix of breccias (Figs 11, 13 and 26). In the hyaloclastites, the sulfides typically infill spaces between the fragments, although in places, sulfides also replace fragments (Fig. 26).

Pyrite was the most abundant sulfide present in the high-grade ore remnants in YD09-01 at Just Desserts, although massive coarse-grained chalcopyrite and pyrrhotite were also present in the core used for metallurgy, as illustrated in Empire Resources Ltd (2009b). There are at least two generations of pyrite: an early spongy melnikovite pyrite and a later clear euhedral to subhedral pyrite (Fig. 27a). The early pyrite is replaced by chalcopyrite, pyrrhotite, sphalerite, and the clear pyrite (Fig. 28a). The clear pyrite is in turn replaced by chalcopyrite along fractures (Fig. 28a) and contains small inclusions of chalcopyrite, pyrrhotite, magnetite, native gold (Fig. 27b), and tellurides (Fig. 28b). Chalcopyrite also replaces an early generation of pyrrhotite (Fig. 29). Unusual blebs of pyrrhotite rimmed by pyrite described as ‘framboidal-like’ were also illustrated by Empire Resources Ltd (2009b) and interpreted as consistent with a VMS origin.

Pyrrhotite was the dominant sulfide intersected at depth in the Trajan area in YRC10-13D, where it is associated with chalcopyrite infilling the matrix of a cherty breccia (Fig. 30a). The chert in the breccia has largely recrystallized to quartz although some fragments show evidence of original bedding where impurities have migrated into the centres of what may have been colloidal blebs (Fig. 30b).

In the mineralized zone intersected by YRC09-01D at the C Zone, pyrrhotite tends to dominate over pyrite and is very porous, suggesting that it replaces melnikovite pyrite, although it may have been precipitated directly as pyrrhotite. This pyrrhotite infills the matrix of a breccia and has been partially replaced by sphalerite, chalcopyrite, and clear pyrite (Fig. 31). In places it is associated with euhedral to subhedral magnetite and accessory native gold and tellurides.

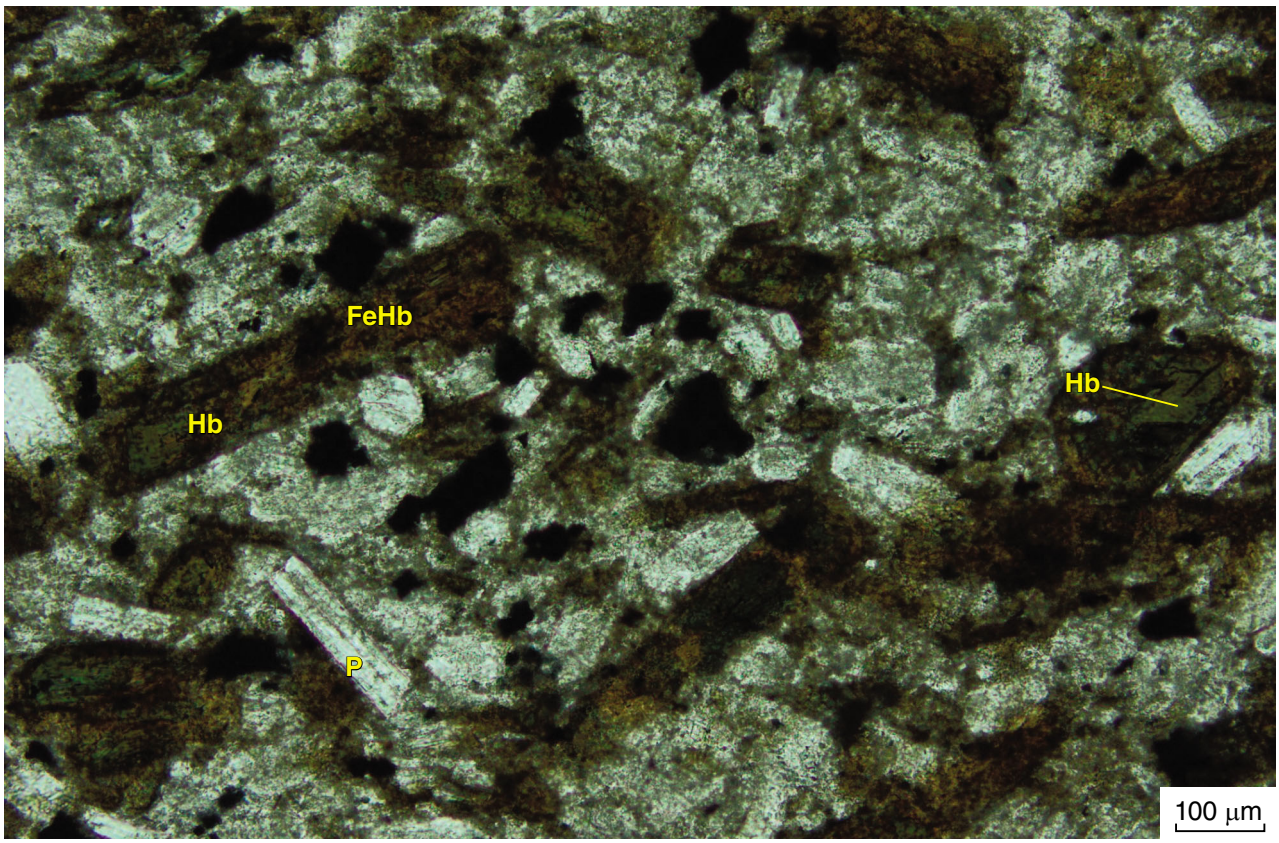

Figure 25. **Intrusive andesite with phenocrysts of green hornblende (Hb) largely replaced by brown ferrohornblende (FeHb) in matrix of plagioclase laths (P) and fine-grained FeHb**

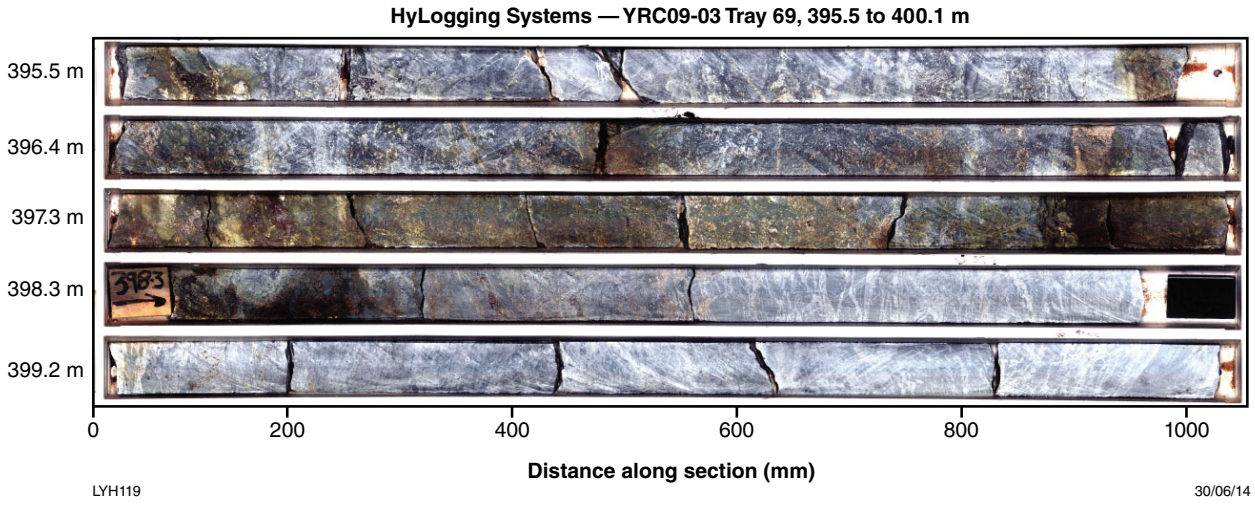

Figure 26. **Drillcore from YD09-03 (395.5 – 400.1 m) showing sulfides infilling matrix of basaltic hyaloclastite (399.1 – 400.1 m), forming matrix to chert breccia (397.3 – 398.3 m) and infilling fractures in chert (395.5 – 397.3 m)**

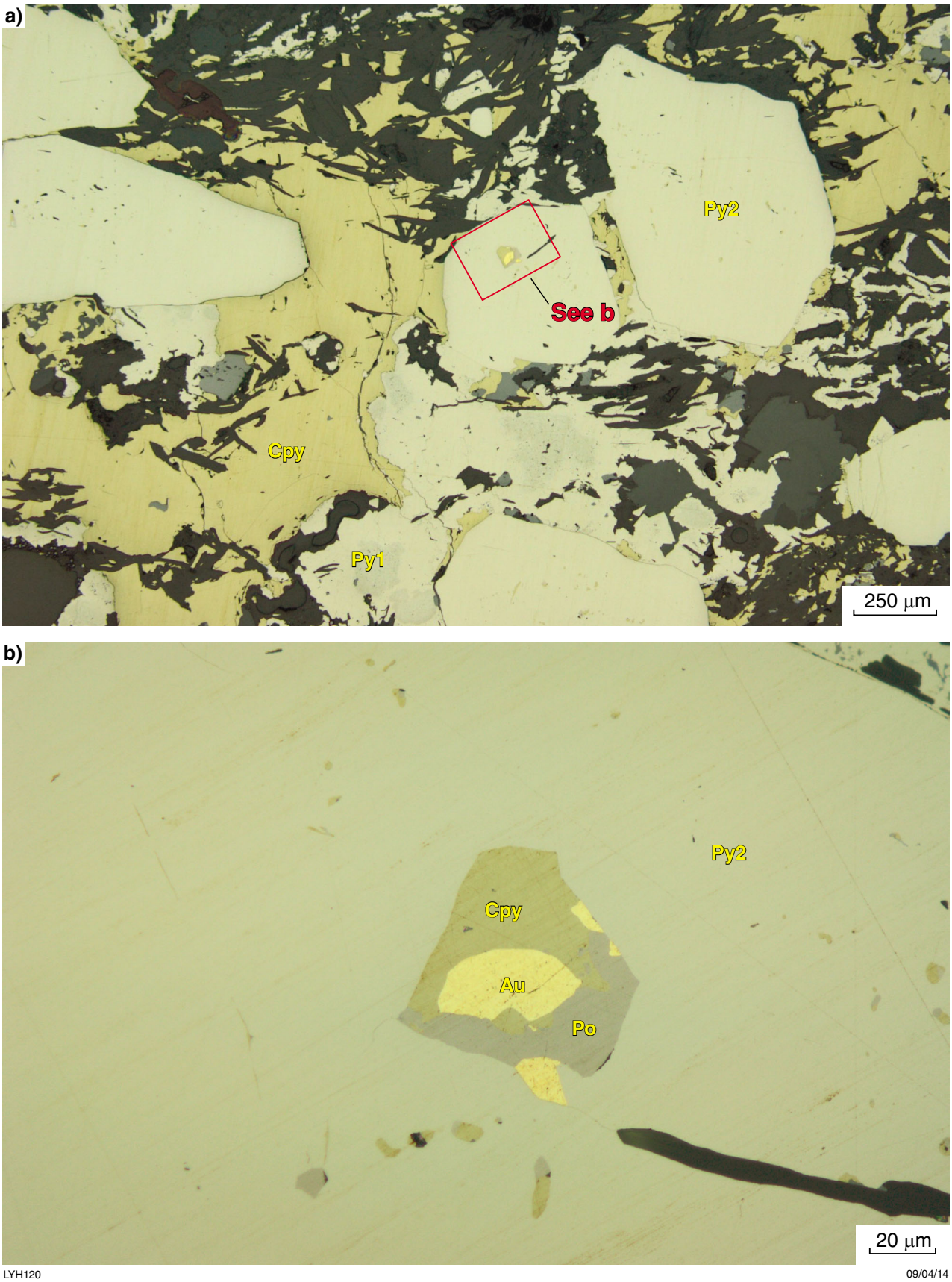

Figure 27. **a) Chalcopyrite (Cpy) and two generations of pyrite: an early irregular melnikovite pyrite (Py1) and a later clear variety (Py2) in high-grade ore; b) higher magnification view of a) showing inclusion of gold (Au), chalcopyrite (Cpy), and pyrrhotite (Po) in clear pyrite (GSWA 204946 from 76.7 m in YD09-01, Just Desserts deposit); reflected light**

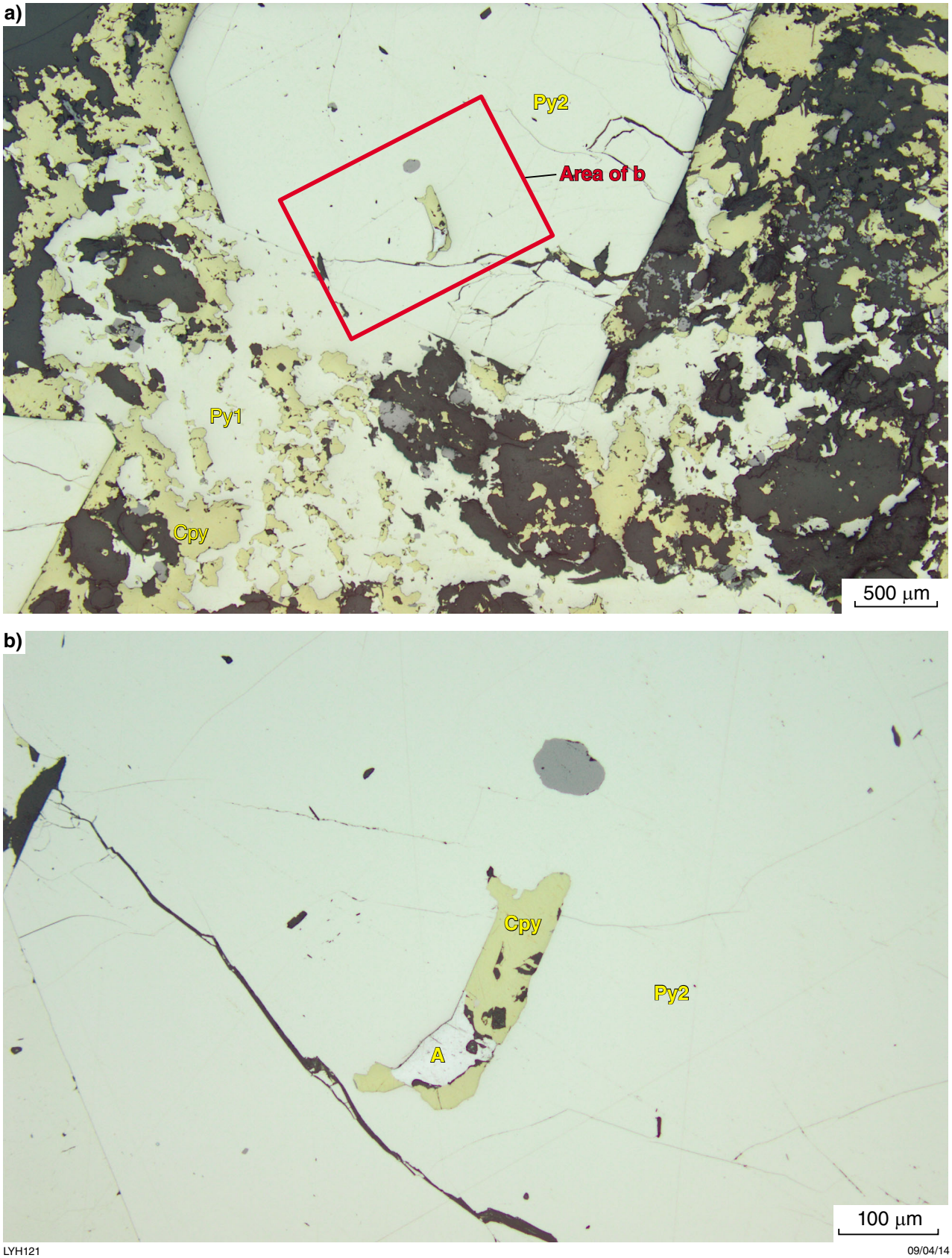

Figure 28. a) Chalcopyrite (Cpy) replacing an early generation pyrite (Py1), and infilling fractures and as inclusions in later clear pyrite (Py2); b) higher magnification view of a) showing inclusion of chalcopyrite and altaite (A) (lead telluride) in clear pyrite (GSWA 204944 from 108.7 m in YD09-01, Just Desserts deposit); reflected light

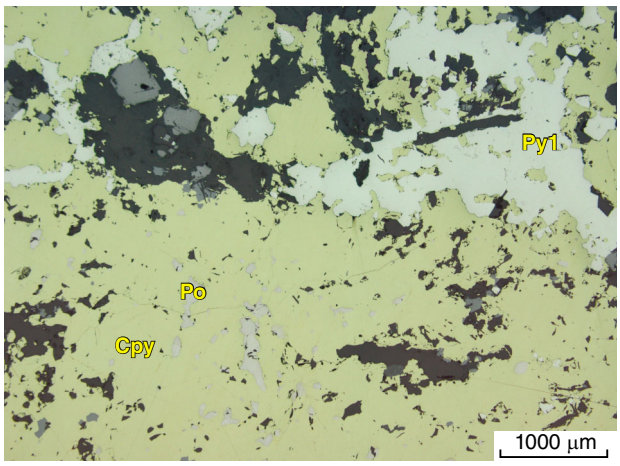

Figure 29. **Chalcopyrite (Cpy) replacing early generation of pyrrhotite (Po) leaving isolated remnants of pyrrhotite within the chalcopyrite; chalcopyrite also replaces early pyrite (Py1) (same sample as Fig. 28)**

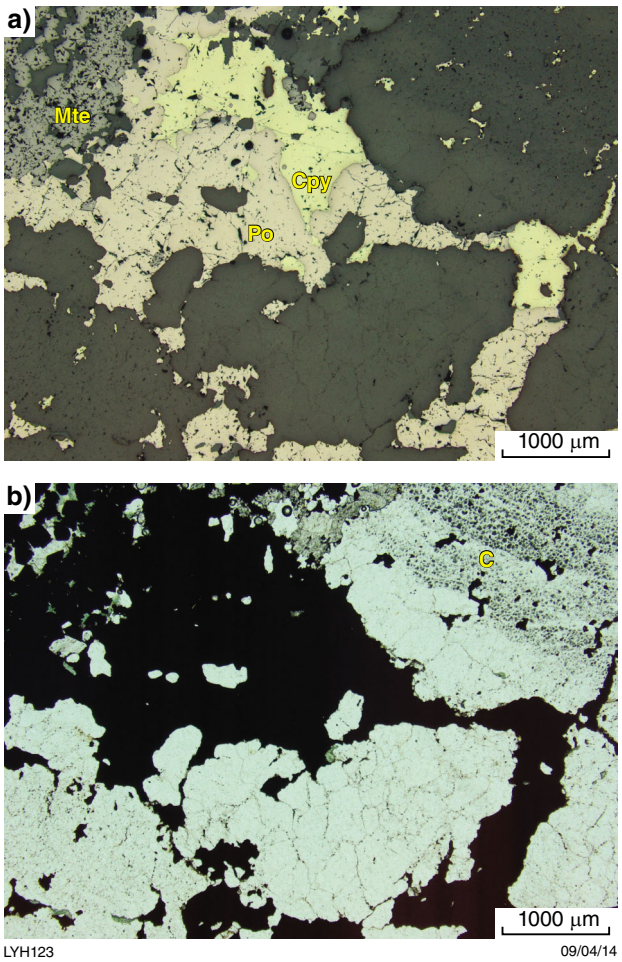

Figure 30. **Pyrrhotite (Po), chalcopyrite (Cpy), and magnetite (Mte) in matrix of chert breccia (GSWA 20815 from 403.4 m in YRC10-13D: a) reflected light; b) plane-polarized light; includes recrystallized chert fragment (C) showing evidence of original bedding where impurities migrated into the centres of what may have been colloidal blebs**

Pyrrhotite and chalcopyrite are the dominant sulfides in the stringer-type mineralization infilling fractures in the chemical sedimentary rocks (Fig. 32a) in both the Just Desserts – Trajan area and the C Zone. Gold and tellurides are also associated with stringer mineralization (Fig. 32b).

Tellurides identified using optical properties and scanning electron microscopy (SEM) in the Just Desserts – Trajan – C Zone area include tellurobismuthite (Bi_2Te_3), melonite ($NiTe_2$), a Co–Ni telluride, hessite (Ag_2Te), petzite (Ag_3AuTe_2), altaite (PbTe), rucklidgeite ($[Bi, Pb]_3Te_4$), and tetradymite (Bi_2Te_2S).

Molybdenite was observed in association with disseminated chalcopyrite and pyrrhotite, and apatite in the matrix of talc-altered hyaloclastite beneath the mineralized zone in YD09-03 (Fig. 33).

Locally abundant magnetite is associated with the mineralization infilling the matrix in breccia zones and with the stringer mineralization infilling fractures in the chemical sedimentary rocks. There are at least two generations of magnetite apart from that in the BIF: an early generation with irregular spongy form and a later clear form that locally includes blebs of pyrrhotite (Fig. 34).

Tiny grains of uraninite and a rare earth mineral were discovered as bright specks during SEM analysis on mineralized samples from Just Desserts and C Zone, respectively. The rare earth mineral gave a semiquantitative analysis of 12.9% La, 11.8% P, 10.6% Ba, 8.6% Fe, 3.2% V, 3.1% Cr, 1.1% Ce, and 1.8% S. Its identity is unknown.

Augustus area

The mineralization intersected in YD10-01 is mostly associated with thin crosscutting quartz–carbonate–sulfide veins that intersect gabbro, dolerite, basalt, and mafic lithic tuff. Semimassive sulfides associated with BIF that has been intruded by leucogabbro or dolerite (Fig. 19) may be the remnants of VMS mineralization; alternatively, they could be later hydrothermal mineralization related to the quartz vein, as discussed in the section on Geology. Pyrrhotite, pyrite, and chalcopyrite are the main sulfides present. Magnetite is also abundant in the semimassive sulfides (Fig. 35). One small telluride aggregate, which SEM indicated was composed of melonite ($NiTe_2$) and tellurobismuthite (Bi_2Te_3), was enclosed in pyrrhotite from one of the mineralized veins (Fig. 36).

Hydrothermal alteration and metasomatism

HyLogger data were used in conjunction with petrology and SEM to study the alteration at Yuinmery. HyLogger data were analysed using The Spectral Geologist (TSG), software developed by CSIRO Earth Science and Resource Engineering and marketed by Aussec International Pty Ltd. This program compares obtained spectra with the spectra

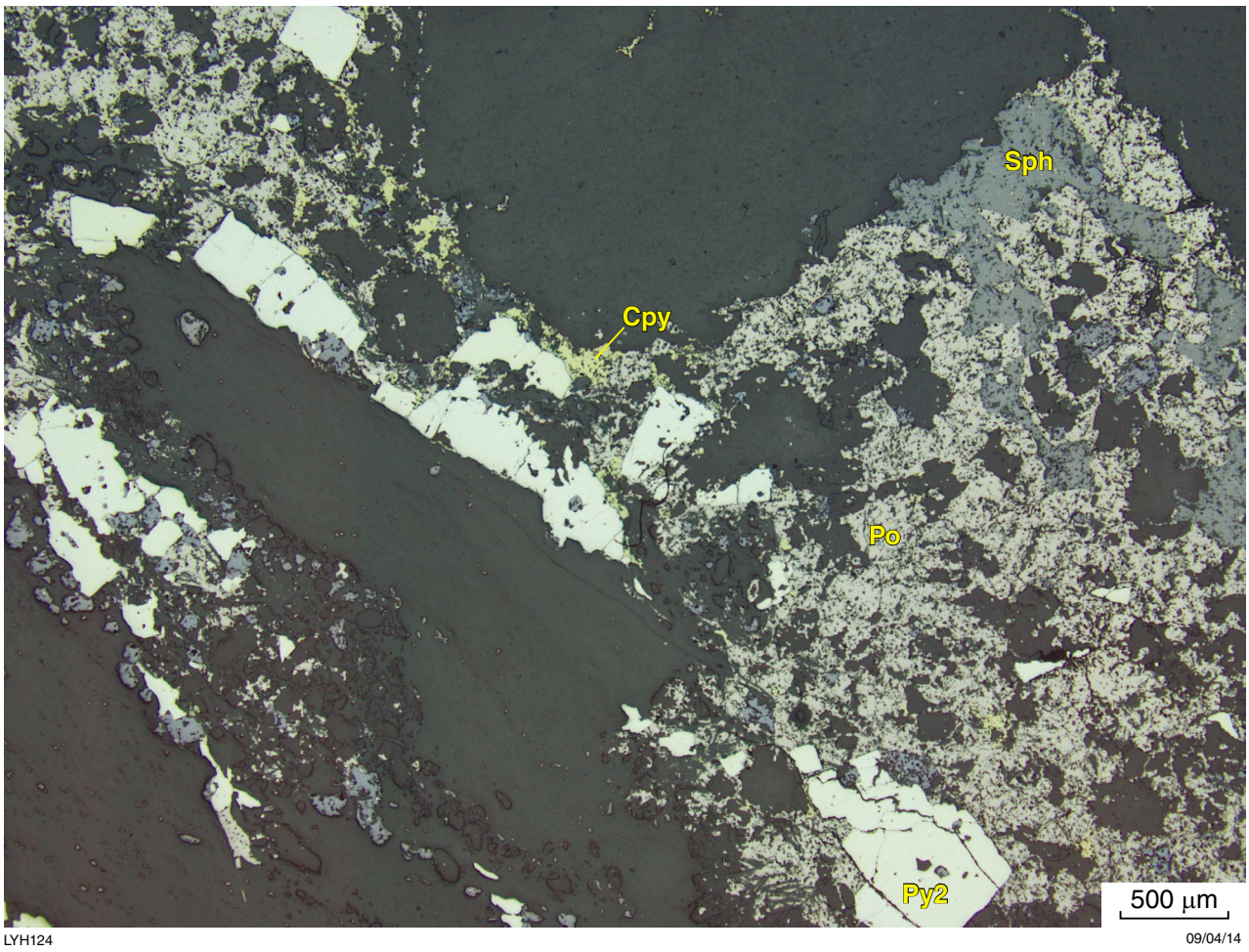

Figure 31. **Porous pyrrhotite (Po) partially replaced by sphalerite (Sph), chalcopyrite (Cpy), and clear pyrite (Py2) in matrix of breccia interpreted to have formed near a hydrothermal vent (GSWA 208126 from 251.3 m in YRC09-01D, C Zone; same sample as in Fig. 13)**

of known minerals and provides a system-generated interpretation of the minerals for each interval analysed (approximately 8 mm) (Pontual 2008; Hancock et al., 2013). The three main minerals contributing to the spectra are calculated for each interval for the thermal infrared (TIR) spectrum, and the two main minerals are calculated for the short wave infrared (SWIR) spectrum. A summary plot is calculated by averaging these mineral results over a larger chosen interval (1–4 m, depending on length of drillhole). SWIR is better for identifying micas, chlorite, and clay minerals and TIR is better for identifying quartz, feldspars, pyroxenes, garnet, and phosphates. Both can identify amphiboles, talc, and carbonates (Hancock et al., 2013). Visible near infrared (VNIR) is good for identifying iron oxides and rare earth elements (REE) (Morin-Ka, 2012; Hancock et al., 2013).

Given the large numbers of possible overlaps of absorption features from different minerals, particularly for TIR, it is not surprising that the system-generated interpretation of minerals is commonly wrong. For example, an early version of TSG reported approximately 30% topaz downhole in YD09-01 in the TIR summary yet no topaz was observed in thin section. The latest version of TSG available at the time of writing this report (version 7.1.0.059) correctly interprets this mineral as chlorite although it still shows large amounts of prehnite in the TIR summary plot for this drillhole, whereas none is shown in the SWIR summary. Fortunately, TSG has the provision to allow or not allow minerals. For example, prehnite is readily identified in SWIR (Hancock et al., 2013); however, no prehnite was recognized in core or thin section, so it is reasonable to not allow prehnite. Appendix 3 lists the allowed and not allowed minerals used for the Yuinmery core determined by trial and error and using petrology as a guide. Although not always correct, the data generated using this list are far better than the system-generated data.

The scatter plot tab in TSG allows for individual minerals to be plotted downhole using either the first, second, or third most abundant mineral picked up in each 8 mm interval. It was more useful for TSG to calculate a combined weighted average for the mineral regardless of whether it is the first, second, or third mineral.

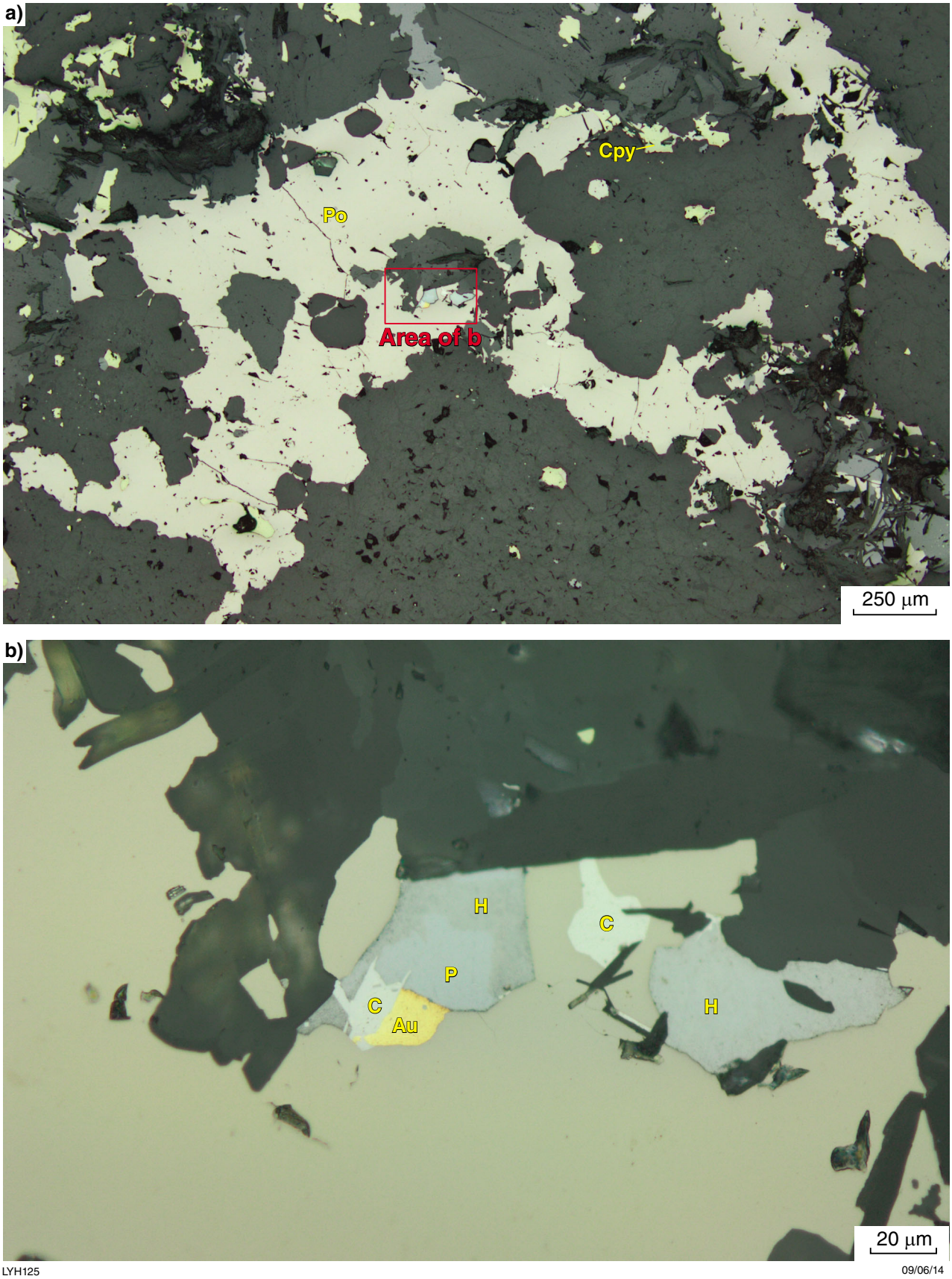

Figure 32. **a) Pyrrhotite (Po) and chalcopyrite (Cpy) infilling fracture in chert; b) enlargement of a) showing aggregate of gold (Au) and tellurides including petzite (P), hessite (H), and a Co–Ni telluride (C) (GSWA 208056 from 393.5 m in YD09-03)**

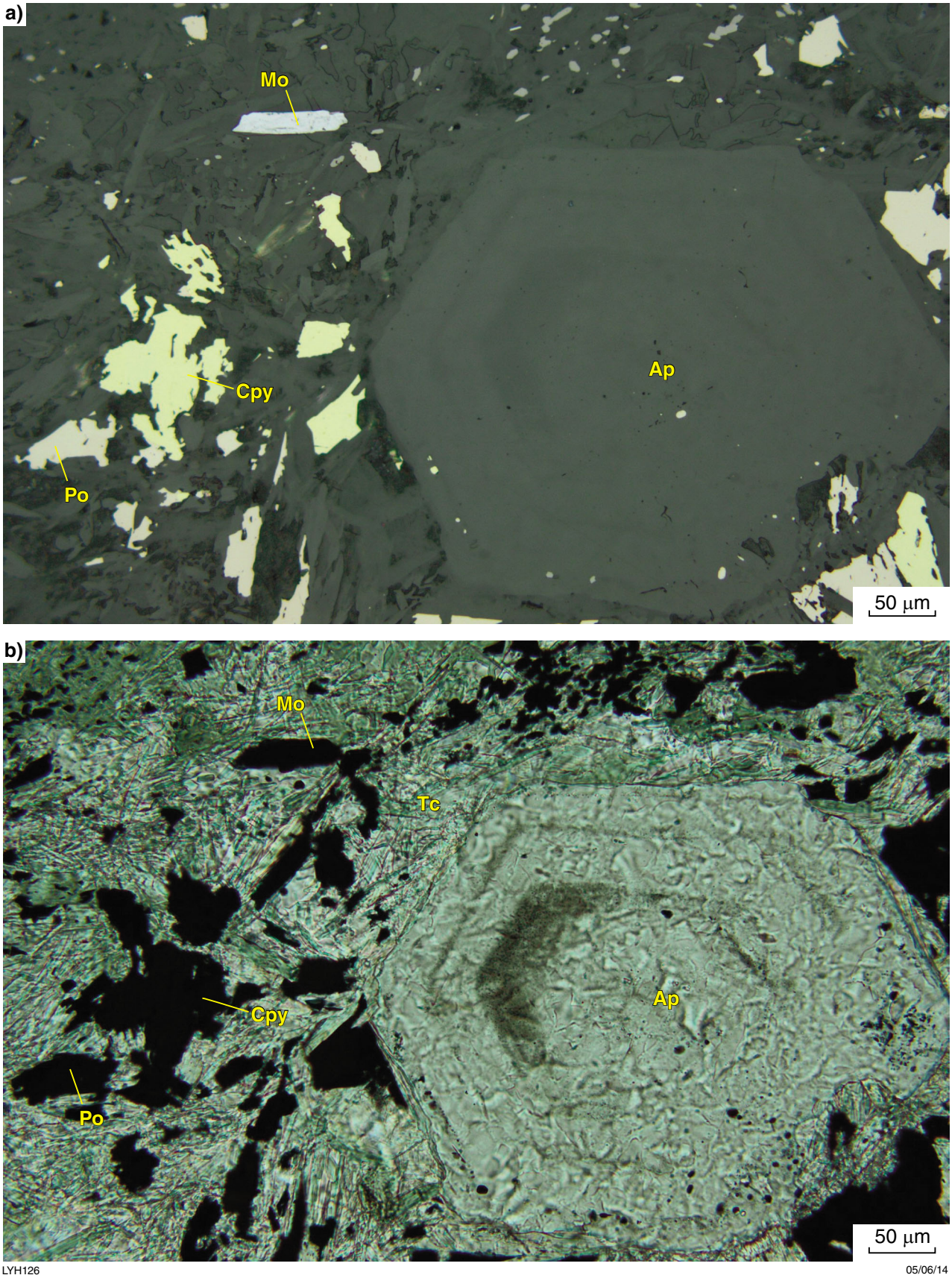

Figure 33. **Molybdenite (Mo) associated with chalcopyrite (Cpy), pyrrhotite (Po), talc (Tc), and zoned apatite crystal (Ap) in matrix of altered hyaloclastite (GSWA 208058 from 399.0 m in YD09-03): a) reflected light; b) plane-polarized light**

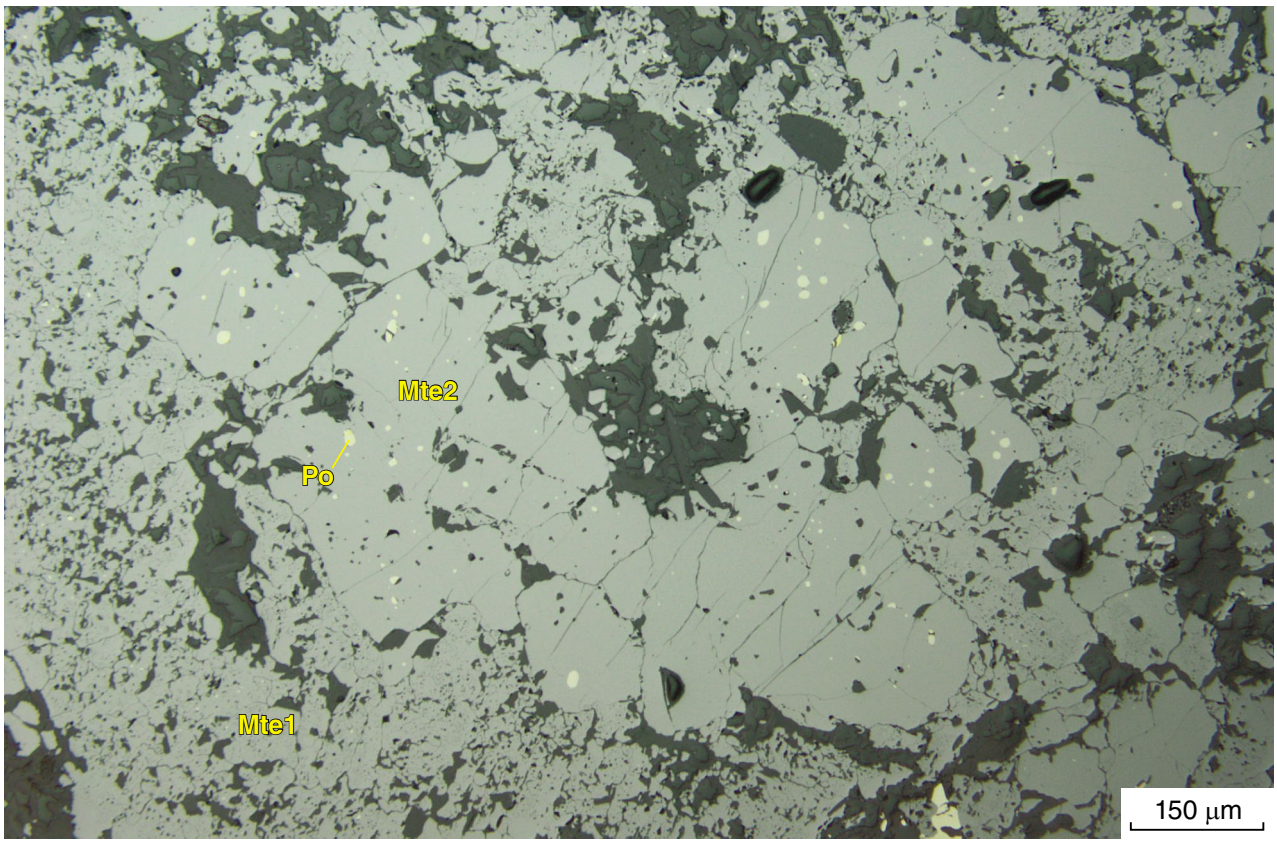

Figure 34. **Two generations of magnetite: an early irregular form (Mte1) and a later well-crystallized form (Mte2) with pyrrhotite inclusions (Po)**

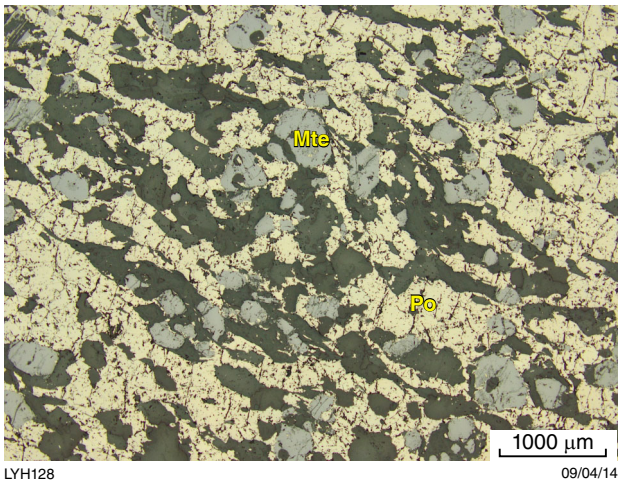

Figure 35. **Semimassive pyrrhotite (Po) with disseminated subhedral magnetite (Mte) (GSWA 208103 from 270.4 m in YD10-01)**

Where a particular mineral is not in the TSG library, spectra can be matched with another spectral library and the results plotted downhole, as above. The wavelengths of the absorption features of some minerals such as chlorite and white micas vary with the composition of the mineral, as described by McLeod et al. (1987), Herrmann et al. (2001), and Pontual (2008); the wavelength can also be plotted downhole. In addition, TSG allows assay and drillhole logs to be imported and displayed along with the other scatter plots.

HyLogger data for YD09-01, YD09-03, YRC10-13D, YRC09-01D, and YD10-01 are given in Appendices 4, 5, 6, 7, and 8, respectively. Data presented include summary plots of minerals for both TIR and SWIR, and where appropriate, scatter plots showing variations in abundance or composition (i.e. wavelength) of the most important alteration minerals for each drillhole. For each drillhole, a log of simplified geology is given for comparison because it is essential to consider the composition of the host rock when looking at alteration.

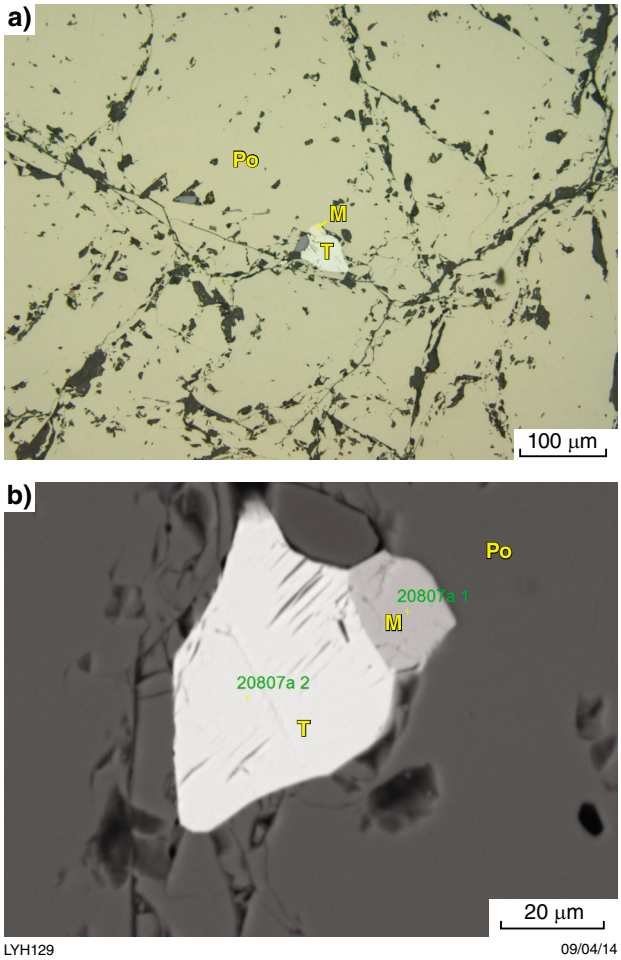

Figure 36. **Small inclusion of tellurobismuthite (T) and melonite (M) in pyrrhotite (Po) (GSWA 208107 from 279.5 m in YD10-01); a) reflected light; b) scanning electron micrograph**

Selected minerals were analysed using a FEI XL40 SEM fitted with a Bruker X-flash 5030 energy dispersive spectrometer (EDS) at the CSIRO Division of Earth Science and Resource Engineering at Kensington, Western Australia. Results were recalculated to 100% after correcting for background using the Quantax Esprit EDS software of Bruker Nano GmbH, Germany (Michael Verrall, CSIRO, 2013, written comm., 26 August).

The main alteration minerals are described below along with their optical properties, geochemistry, and spectral characteristics where appropriate.

Talc

The TIR and, to a lesser extent, SWIR summary plots for YD09-01 (Appendix 4) show that talc is the dominant alteration mineral in the basaltic hyaloclastites underlying the upper mineralized zone at the Just Desserts deposit. Talc alteration continues downhole for about 16 m until the hyaloclastites are stoped out by granophyre. In places, the hyaloclastite is almost completely replaced by fine-grained talc with coarser grained talc near sulfides (Fig. 37). In other places, remnants of chloritic hyaloclastite remain (Fig. 38). Talc is also abundant in the BIF between the second and third zones of mineralization (Fig. 39) and is present for several metres in the BIF below the third zone of mineralization until the BIF is stoped out by intrusive andesite. There is only minor talc in the hyaloclastites above the fourth (lowest) mineralized zone and in the basalt beneath it. This talc is not visible in the summary plots although it is visible in the scatter plot where the weighted values for talc are plotted (Appendix 5e) and in thin section. Talc is also the dominant alteration mineral in the low-grade mineralization intersected in YD09-03 and in the underlying hyaloclastite (Appendix 5a; Fig. 33b), although talc alteration is much less extensive than in YD09-01. Only minor talc is associated with the mineralization and surrounding BIF intersected in YRC10-13D; this does not show up in the TIR summary plot (Appendix 6a) although it appears in the scatter plot where the weighted values for talc are plotted (Appendix 6e).

At C Zone in YRC09-01D, talc is abundant in the mineralized zone and in the BIF up to 4 m above mineralization and in the BIF for about 50 cm beneath the main mineralized zone. However, talc is only a minor component in the hyaloclastite and basalt below this zone, even where the hyaloclastite and basalt are mineralized (Appendix 7a,e).

There is very little talc associated with mineralization in YD10-01 at the Augustus prospect, although some talc has formed as an alteration mineral in the pyroxenite (Appendix 8a,e).

Semiquantitative SEM analyses of the talc from YD09-01 and YD09-03 are given in Table 2. Because SEM does not determine water content, results for other elements will be a little high. Sulfur and copper are included in the table because they indicate the extent of error from backscatter from adjacent sulfides. Assays with more than 2% S were discarded as the iron result would be elevated. The talc is not pure ($Mg_6[Si_8O_{20}](OH)_4$) but has significant although variable amounts of iron (6.5 – 21.5%), approaching minnesotaite ($Fe_6[Si_8O_{20}](OH)_4$) composition.

Chlorite

Chlorite is an important alteration mineral throughout the stratigraphic succession at Yuinmery except in strongly mineralized zones (Appendices 4a,b, 5a,b, 6a,b, 7a,b, and 8a,b). It forms as a fine-grained alteration product in the hyaloclastites where it has been partially replaced by talc (Fig. 38) and also as an alteration product in andesite, basalt, silicate-facies BIF, and the intrusive rocks. Coarser grained chlorite is present in crosscutting veinlets (Fig. 40).

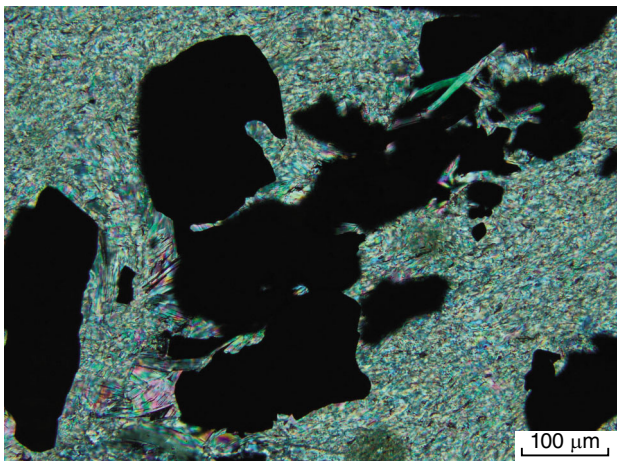

LYH130 08/04/14

Figure 37. Hyaloclastite beneath upper mineralized zone at Just Desserts that has been almost completely replaced by fine-grained talc with coarser grained talc developed near sulfides (GSWA 204961 from 77.3 m in YD09-01)

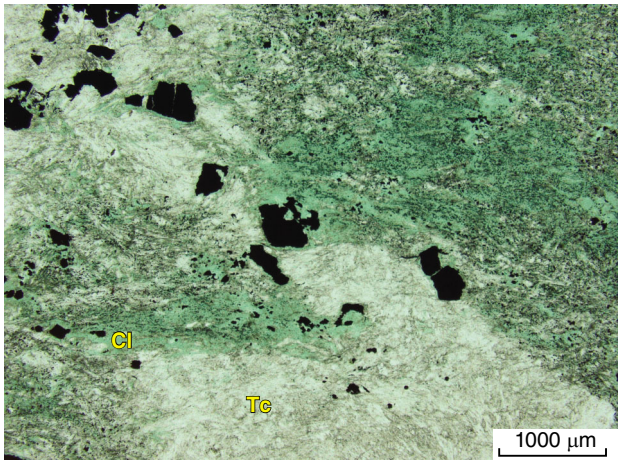

LYH131 09/04/14

Figure 38. Chloritized hyaloclastite with chlorite (Cl) partially replaced by talc (Tc) (GSWA 204963 from 82.7 m in YD09-01); plane-polarized light

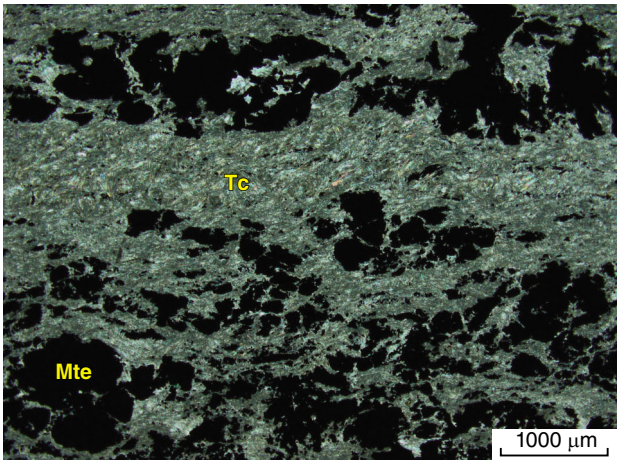

LYH132 09/04/14

Figure 39. Talc laminae (Tc) alternating with magnetite laminae (Mte) in BIF (GSWA 204971 from 114.9 m in YD09-01); crossed polars

Petrographic examination revealed a wide range in optical properties of the chlorite. The chlorite varies from colourless to medium green in plane-polarized light. Some crystals have normal interference colours whereas others display anomalous olive, brown, mauve, or bright blue colours under crossed polars (Table 3). In some sections chlorite crystals with different optical properties are in juxtaposition (Fig. 40). In the section illustrated in Figure 40, chlorite with anomalous blue interference colours appears to replace chlorite with olive interference colours along a veinlet. Chlorite with olive interference colours is also abundant in the matrix of the rock. There is clearly more than one generation of chlorite.

Pontual (2008) showed that the wavelength of the SWIR FeOH absorption feature of chlorite varies from about 2246 nm for Mg# = 1 to about 2260 nm for Mg# = 0 (Mg# = atomic % of Mg divided by the atomic % of Mg+Fe). The composition of the chlorite is strongly influenced by the composition of the host rock. This effect is particularly obvious in YD09-03 and YRC10-13D where wavelength plots of the FeOH absorption feature of chlorite vs depth indicate that the chlorites associated with gabbro are more magnesium rich than those associated with the volcanic rocks and granophyre (Appendices 5f, 6f).

In YRC09-01D, where the succession is not disrupted by intrusions, the wavelength of the FeOH absorption feature of chlorite falls within a fairly constant range, except near mineralization where there is more scatter. However, an overall increase suggests that more iron-rich chlorite is associated with mineralization (Appendix 7f). However, in YD09-01, which was drilled through the middle of the Just Desserts deposit, chlorite in the volcanic rocks between and adjacent to mineralization shows a wide scatter in wavelength (Appendix 4f), suggesting variation from magnesium rich to iron rich.

SEM analyses of selected chlorites are given in Table 4. Mg# was calculated after correcting for iron contributed by sulfides. Mg# calculated from the SEM analyses and Mg# estimated from the HyLogger 2250 nm absorption feature are compared in Table 3 along with the optical properties of the chlorite and distance of the sample from mineralization. Mg# calculated from the SEM analyses fall within a much narrower range (0.26 – 0.68) than those estimated from the 2250 nm absorption feature (0–1). Samples with the greatest discrepancy between the SEM results and the results estimated from the 2250 nm absorption feature tended to show a weak signal, especially where TSG did not identify chlorite at all, giving a result of aspectral or null; most samples containing abundant sulfides or oxides fell in this category. In general, where TSG identified Fe chlorite, typically it was more Fe rich and where it identified Mg chlorite it was relatively magnesium rich, even though all of the chlorite should be probably classified as Fe–Mg chlorite.

The optical properties of the chlorite showed some correlation with the Mg# derived from SEM analysis, where the more iron-rich samples had anomalous blue interference colours and the more magnesium-rich samples normal to olive interference colours.Those with brown to mauve interference colours tended to intermediate composition. However, for some chlorite with

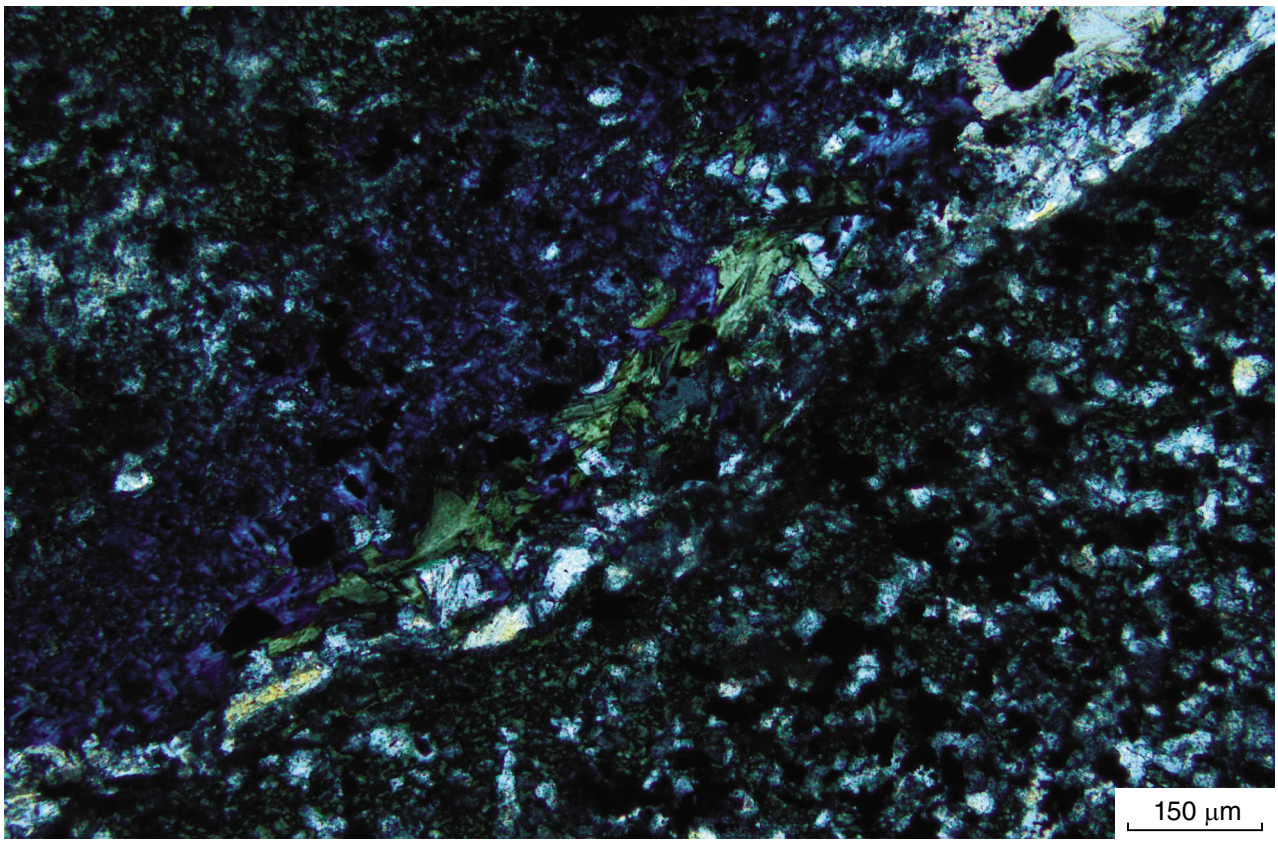

Figure 40. **Chlorite with bright blue anomalous interference colours appears to replace chlorite with olive interference colours within a veinlet. Matrix also contains chlorite with olive green interference colours (GSWA 208133 from 265.0 m in YD09-01D)**

olive anomalous interference colours(e.g. GSWA 208133), Mg# < 0.5 so the optical properties alone cannot be used to determine chlorite composition.

On the basis of the SEM results, chlorite crystals within 5 m of mineralization range in Mg# 0.26 – 0.68, whereas those analysed from andesite and basalt 15 m or more from mineralization show a narrower Mg# range of 0.42 – 0.45. This, in addition to the weaker absorption features in the presence of sulfides, explains the greater scatter in the TSG results near mineralization.

Amphiboles

Apart from primary hornblende (and its alteration product, actinolite) present in the intrusive rocks and volcanic rocks, there are non-primary amphiboles of the grunerite–cummingtonite and anthophyllite–ferroanthophyllite series that are associated with mineralization, BIF, and highly altered volcanic rocks. These amphiboles take on a wide variety of forms even within the same section. They were identified on the basis of their optical properties and their chemistry was checked by SEM. Table 5 gives the analyses and calculated Mg#. Although the HyLogger in TIR mode identified amphiboles as a group, it was not able to distinguish members of the grunerite–cummingtonite and anthophyllite–ferroanthophyllite series due to overlapping absorption features of the different amphiboles and talc.

Spectral matching of United States Geological Survey (USGS) SWIR spectra with the HyLogger data in TSG for anthophyllite and cummingtonite gave too many false positives where hornblende and actinolite were present. An absorption feature at about 980 nm in SWIR may be characteristic of members of the anthophyllite–gedrite series (J Huntington, 2013, written comm., 28 August). This feature was found in most spectra where cummingtonite or anthophyllite had been identified in thin section (Fig. 41). A spectral match on the 980 nm absorption feature using the 'PFIT' feature of TSG gave the best indication of where these minerals were present and was therefore used to represent these Ca-poor amphiboles in Appendices 4g, 5g, 6g, 7g, and 8g, even though TSG was unable to distinguish between the orthorhombic and monoclinic series. Where appropriate, the HyLogger results are discussed in more detail below.

Table 2. Talc analyses 1–13

Analysis no.	*1*	*2*	*3*	*4*	*5*	*6*	*7*	*8*	*9*	*10*	*11*	*12*	*13*
SiO_2	63.00	62.72	63.02	60.88	61.73	61.79	62.06	61.36	61.91	62.53	61.92	61.68	60.76
TiO_2	0.01	0.02	0.01	0.03	0.02	0.00	0.01	0.04	0.01	0.01	0.03	0.07	0.34
Al_2O_3	0.58	0.82	0.66	0.47	0.47	0.54	0.87	0.85	0.81	0.84	1.23	1.34	1.01
FeO	8.50	7.91	7.30	12.91	10.11	10.04	8.62	9.57	9.91	9.39	7.96	8.24	8.56
MnO	0.01	0.00	0.00	0.01	0.02	0.00	0.00	0.01	0.02	0.01	0.02	0.02	0.01
MgO	27.40	27.97	28.44	24.16	26.26	26.38	27.24	26.40	26.38	26.55	27.97	27.98	28.34
CaO	0.01	0.00	0.02	0.19	0.17	0.14	0.02	0.06	0.04	0.07	0.05	0.02	0.04
Na_2O	0.30	0.36	0.33	0.37	0.34	0.32	0.30	0.39	0.39	0.24	0.45	0.37	0.41
K_2O	0.02	0.02	0.02	0.08	0.03	0.08	0.04	0.32	0.05	0.02	0.03	0.00	0.04
P_2O_5	0.04	0.04	0.05	0.20	0.22	0.13	0.07	0.03	0.07	0.00	0.13	0.14	0.15
Cl	0.01	0.00	0.01	0.01	0.01	0.00	0.00	0.21	0.00	0.01	0.02	0.00	0.00
S	0.07	0.07	0.07	0.44	0.40	0.32	0.61	0.54	0.25	0.19	0.09	0.06	0.21
Cu	0.07	0.08	0.08	0.25	0.22	0.26	0.14	0.22	0.15	0.13	0.09	0.07	0.13

Table 2. Talc analyses 14–26

Analysis no.	*14*	*15*	*16*	*17*	*18*	*19*	*20*	*21*	*22*	*23*	*24*	*25*	*26*
SiO_2	61.21	59.35	58.39	60.74	55.35	61.50	62.23	62.28	60.82	62.06	62.32	62.08	57.18
TiO_2	0.24	0.05	0.05	0.03	0.00	0.01	0.02	0.02	0.05	0.02	0.03	0.02	0.01
Al_2O_3	1.17	0.87	1.11	1.19	0.87	0.75	0.45	0.49	1.25	0.59	0.54	0.61	0.47
FeO	6.53	9.69	9.87	7.34	21.54	9.35	9.01	8.96	11.41	9.99	9.49	10.20	19.55
MnO	0.01	0.02	0.00	0.06	0.22	0.02	0.01	0.00	0.00	0.02	0.00	0.01	0.15
MgO	30.07	27.41	27.15	26.92	20.61	27.25	27.28	27.04	25.61	26.47	26.63	26.14	21.17
CaO	0.04	0.01	0.05	3.14	0.13	0.04	0.03	0.07	0.03	0.03	0.03	0.04	0.10
Na_2O	0.38	0.42	0.32	0.37	0.53	0.36	0.35	0.34	0.33	0.37	0.37	0.39	0.46
K_2O	0.02	0.00	0.02	0.00	0.02	0.03	0.02	0.02	0.02	0.02	0.01	0.01	0.00
P_2O_5	0.04	0.14	0.06	0.00	0.15	0.13	0.10	0.15	0.11	0.10	0.16	0.15	0.18
Cl	0.00	0.00	0.00	0.01	0.00	0.00	0.00	0.00	0.00	0.00	0.00	0.00	0.00
S	0.16	1.40	1.91	0.03	0.30	0.35	0.34	0.35	0.25	0.23	0.23	0.22	0.42
Cu	0.13	0.62	1.07	0.17	0.27	0.22	0.17	0.28	0.12	0.09	0.18	0.13	0.31

NOTES: Sample descriptions:
1–3 GSWA 204961 from 77.2 m in YD09-01
4–10 GSWA 204962 from 78.4 m in YD09-01
11–14 GSWA 204964 from 82.7 m in YD09-01
15–17 GSWA 204965 from 144.6 m in YD09-01
18–26 GSWA 208058 from 398.9 m in YD09-03

Table 3. Chlorite properties

Drillhole	*Depth (m)*	*Sample no.*	*Wavelength (nm)*	*Pleochroism*	*Interference colour*	*TSG name*	*2250 name*	*2250 Mg#*[(a)]	*SEM Mg#*[(b)]	*Lithology*	*Position relative to mineralization*
YD09-01	78.4	204962	2247–2253	C–L green	Olive	Mg	Mg–FeMg	0.9 – 0.5	0.59, 0.53	Basaltic hyaloclastite	1.4 m below upper mineralized zone
YD09-01	82.7	204964	2242–2245	C–L green	Normal to olive	–	Mg	1	0.55, 0.54, 0.56, 0.59, 0.65	Basaltic hyaloclastite	5.5 m below upper mineralized zone
YD09-01	86.4	204965	2242–2250	C–M green	Brown	–	Mg–FeMg	1–0.65	0.56, 0.53	Mineralized hyaloclastite	Minor mineralized horizon below upper zone
YD09-01	110.3	204969	2250–2254	C–L green	Purple–brown	FeMg	FeMg	0.65–0.4	0.42, 0.41, 0.41, 0.39, 0.38	Intermendiate ?tuff	1 m below second mineralized zone
YD09-01	110.3	204969	2249, 2259	C–M green	Purple–blue	Fe	Mg, Fe	0.8, 0	0.42, 0.41, 0.41, 0.39, 0.38	Intermendiate ?tuff	1 m below second mineralized zone
YD09-01	121.3	204945	2244–2252	C–L green	Olive	Aspectral		1–0.55	0.55: 0.53	Mineralized breccia	Base of third mineralized zone
YD09-01	143.8	204980	2249–2252	C–M green	Olive to brown	FeMg	FeMg	0.75–0.55	0.45, 0.48	Amygdaloidal basalt	1 m below fourth mineralized zone
YD09-01	144.6	204981	2244–2252	C–L green	Normal to olive	Mg, FeMg	Mg, FeMg	1–0.55	0.68, 0.67	Basaltic hyaloclastite	2 m below fourth mineralized zone
YD09-03	398.9	208058	2245, 2259	C-L green	Brown	null	Mg, Fe	1, 0	0.52, 0.55, 0.52, 0.53	Basaltic hyaloclastite	Few cm below upper mineralized zone
YRC10-13D	427.2	208026	2249–2255	C–L green	Brown	FeMg	FeMg	0.7–0.3	0.45, 0.44, 0.44, 0.45	Altered basalt	21.8 m below lower mineralized zone
YRC09-01D	206.5	208118	2258–2261	M green	Brown to purple	Fe, FeMg	Fe	0.1–0	0.42, 0.43	Altered andesite	44 m above upper mineralization
YRC09-01D	235.4	208121	2252–2258	L green	Dark brown to green	FeMg	Fe–FeMg	0.55–0.1	0.45, 0.44	Andesite	15 m above upper mineralization
YRC09-01D	244.2	208123	2252–2258	L green	Mostly brown, few flecks of blue to mauve	FeMg	Fe–FeMg	0.55–0.1	0.41, 0.43, 0.44, 0.42	Intermediate hyaloclastite or tuff	5.8 m above upper mineralization

Table 3. continued

Drillhole	*Depth (m)*	*Sample no.*	*Wavelength (nm)*	*Pleochroism*	*Interference colour*	*TSG name*	*2250 name*	*2250 Mg#*[(a)]	*SEM Mg#*[(b)]	*Lithology*	*Position relative to mineralization*
YRC09-01D	246.1	208124	2253–2258	L green	Olive	FeMg, Fe	Fe–FeMg	0.5–0.1	0.53	BIF	3.9 m above upper mineralization
YRC09-01D	250.7	208125	2252–2259	C–L green	Olive to mauve	Aspectral	Fe–FeMg	0.55–0	0.49	Mineralized breccia	Upper mineralization
YRC09-01D	251.5	208127	2242[(c)]	C–L green	Brown to mauve	Aspectral	Mg	1	0.50, 0.50, 0.49, 0.51	BIF breccia	Lower contact with upper mineralization
YRC09-01D	251.5	208127	2242[(c)]	C–L green	Olive	Aspectral	Mg	1	0.6	BIF breccia	Lower contact with upper mineralization
YRC09-01D	257.3	208130	2258–2259	C–L green	Berlin blue	Fe, FeMg	Fe	0.1–0	0.26, 0.29	Basalt	3.2 m below upper mineralization; 3.1 m above second mineralized horizon
YRC09-01D	260.6	208132	2248–2258[(c)]	L green	Bright blue to mauve	Fe, aspectral	Fe–FeMg	0.8–0.1	0.32, 0.33, 0.31	Mineralization	Second mineralized horizon
YRC09-01D	265	208133	2250–2253	C–L green	Olive	FeMg	FeMg	0.65–0.5	0.46, 0.46, 0.44, 0.47	Altered basalt	4.2 m below second mineralized horizon
YRC09-01D	265	208133	2250–2253	C–L green	Bright blue to mauve	FeMg	FeMg	0.65–0.5	0.32, 0.33, 0.33, 0.33	Altered basalt	4.2 m below second mineralized horizon

NOTES: (a) estimated from the HyLogger 2250 nm absorption feature
(b) calculated from SEM analyses
(c) weak signal
– not applicable
BIF banded iron-formation
SEM scanning electron microscope (calculated using Quantax Esprit EDS software, Bruker Nano GmbH, Germany)
TSG The Spectral Geologist software

Table 4. Chlorite analyses 1–14

Analysis no.	*1*	*2*	*3*	*4*	*5*	*6*	*7*	*8*	*9*	*10*	*11*	*12*	*13*	*14*
SiO_2	34.06	29.03	29.64	29.91	33.82	32.99	36.06	30.61	27.95	29.62	28.59	34.72	34.24	33.52
TiO_2	0.02	0.02	0.07	0.13	0.10	0.32	0.09	0.12	0.08	0.09	0.06	0.10	0.06	0.04
Al_2O_3	17.38	19.89	19.81	20.79	16.67	17.19	15.11	17.69	18.53	20.45	20.15	19.06	17.67	18.60
FeO	26.95	31.35	29.95	29.47	29.11	27.48	23.99	29.22	31.17	35.42	37.00	33.03	35.01	35.49
MnO	0.08	0.05	0.05	0.08	0.08	0.04	0.04	0.08	0.06	0.14	0.13	0.12	0.11	0.10
MgO	20.75	18.95	20.03	19.31	19.78	21.13	24.12	19.52	18.52	13.68	13.55	12.53	12.25	11.75
CaO	0.01	0.03	0.04	0.03	0.01	0.01	0.01	0.09	0.18	0.00	0.05	0.04	0.01	0.01
Na_2O	0.07	0.02	0.04	0.01	0.00	0.00	0.00	0.00	0.00	0.16	0.09	0.12	0.00	0.02
K_2O	0.02	0.01	0.00	0.00	0.02	0.01	0.00	0.00	0.00	0.01	0.02	0.01	0.01	0.02
SO_3	0.42	0.42	0.14	0.07	0.21	0.55	0.42	2.13	2.69	0.19	0.12	0.05	0.42	0.20
Cl	0.05	0.07	0.05	0.06	0.06	0.00	0.00	0.03	0.03	0.11	0.09	0.09	0.06	0.07
Cu	0.20	0.18	0.17	0.14	0.14	0.27	0.16	0.49	0.77	0.15	0.15	0.14	0.16	0.17

Table 4. Chlorite analyses 15–28

Analysis no.	*15*	*16*	*17*	*18*	*19*	*20*	*21*	*22*	*23*	*24*	*25*	*26*	*27*	*28*
SiO_2	37.13	35.51	31.02	31.29	34.27	33.28	29.87	30.30	29.65	29.80	31.84	32.53	31.01	32.41
TiO_2	0.03	0.04	0.15	0.15	0.29	0.28	0.05	0.03	0.00	0.01	0.07	0.05	0.08	0.03
Al_2O_3	16.42	17.05	21.57	20.41	20.41	20.43	19.44	19.61	19.57	19.53	21.48	20.61	20.42	20.99
FeO	27.59	29.12	32.36	31.82	20.25	21.23	31.42	29.81	31.60	31.15	31.93	32.23	33.75	31.70
MnO	0.08	0.08	0.09	0.12	0.08	0.08	0.07	0.08	0.06	0.07	0.18	0.19	0.22	0.20
MgO	18.00	17.36	14.46	15.98	23.32	23.43	18.61	19.60	18.72	19.11	14.12	13.81	14.04	14.00
CaO	0.00	0.02	0.07	0.02	1.21	1.03	0.03	0.01	0.02	0.04	0.04	0.00	0.05	0.05
Na_2O	0.08	0.06	0.00	0.00	0.00	0.00	0.08	0.09	0.04	0.03	0.09	0.01	0.04	0.16
K_2O	0.02	0.01	0.00	0.00	0.00	0.02	0.00	0.00	0.00	0.00	0.01	0.13	0.05	0.10
SO_3	0.41	0.51	0.02	0.01	0.00	0.08	0.24	0.28	0.11	0.04	0.00	0.04	0.03	0.02
Cl	0.04	0.07	0.13	0.04	0.01	0.01	0.02	0.06	0.04	0.05	0.09	0.23	0.16	0.19
Cu	0.20	0.19	0.13	0.15	0.14	0.14	0.16	0.13	0.18	0.16	0.15	0.17	0.16	0.15

Table 4. Chlorite analyses 29–42

Analysis no.	*29*	*30*	*31*	*32*	*33*	*34*	*35*	*36*	*37*	*38*	*39*	*40*	*41*	*42*
SiO_2	28.90	29.13	31.12	30.97	26.62	28.18	26.55	26.53	31.26	32.49	29.89	29.99	31.95	29.93
TiO_2	0.12	0.56	0.07	0.09	0.15	0.15	0.19	0.18	0.02	0.08	0.07	0.10	0.12	0.08
Al_2O_3	20.74	20.41	21.55	21.05	22.48	21.97	22.74	22.21	19.24	18.91	19.79	19.47	17.43	18.66
FeO	35.62	34.98	32.34	33.26	36.31	34.81	35.16	36.45	30.44	29.31	32.31	32.38	26.94	33.53
MnO	0.15	0.17	0.15	0.17	0.17	0.18	0.16	0.17	0.11	0.07	0.14	0.12	0.12	0.12
MgO	13.85	14.26	14.44	14.15	13.44	14.15	14.77	14.10	18.53	14.96	17.49	17.71	21.62	17.36
CaO	0.07	0.06	0.02	0.02	0.06	0.04	0.04	0.07	0.03	0.29	0.03	0.01	0.06	0.00
Na_2O	0.22	0.14	0.06	0.00	0.09	0.10	0.08	0.02	0.00	0.00	0.09	0.00	0.21	0.05
K_2O	0.00	0.01	0.01	0.02	0.00	0.00	0.00	0.01	0.00	0.01	0.01	0.01	0.01	0.00
SO_3	0.10	0.05	0.03	0.02	0.01	0.00	0.04	0.01	0.18	3.67	0.00	0.03	1.31	0.04
Cl	0.08	0.07	0.09	0.10	0.49	0.24	0.07	0.11	0.08	0.07	0.07	0.07	0.07	0.07
Cu	0.14	0.16	0.13	0.15	0.17	0.19	0.19	0.14	0.12	0.14	0.12	0.12	0.15	0.15

Table 4. Chlorite analyses 43–56

Analysis no.	*43*	*44*	*45*	*46*	*47*	*48*	*49*	*50*	*51*	*52*	*53*	*54*	*55*	*56*
SiO_2	29.56	26.42	26.57	20.21	19.55	22.74	27.69	27.97	26.83	26.78	26.93	26.15	27.47	27.07
TiO_2	0.07	0.23	0.51	0.17	0.13	0.29	0.06	0.07	0.12	0.09	0.13	0.06	0.15	0.18
Al_2O_3	19.14	20.42	20.76	18.37	18.62	19.95	21.72	21.32	21.33	21.53	21.37	21.20	23.23	23.43
FeO	32.81	43.11	41.53	40.28	39.16	41.82	34.46	34.29	41.09	40.62	40.49	41.22	34.08	32.88
MnO	0.12	0.23	0.25	0.19	0.16	0.17	0.15	0.13	0.17	0.16	0.17	0.18	0.14	0.14
MgO	18.05	8.23	9.00	9.42	9.60	9.81	15.68	15.94	10.26	10.55	10.65	10.81	14.62	15.82
CaO	0.00	0.85	0.64	0.39	0.16	0.14	0.06	0.01	0.03	0.03	0.01	0.16	0.03	0.01
Na_2O	0.04	0.00	0.15	0.00	0.08	0.00	0.02	0.06	0.00	0.00	0.00	0.04	0.01	0.16
K_2O	0.00	0.00	0.00	0.00	0.00	0.01	0.00	0.00	0.00	0.01	0.00	0.00	0.02	0.02
SO_3	0.03	0.23	0.25	10.66	12.25	4.75	0.00	0.05	0.04	0.07	0.09	0.00	0.00	0.01
Cl	0.04	0.12	0.15	0.11	0.13	0.14	0.01	0.02	0.00	0.00	0.00	0.01	0.12	0.11
Cu	0.13	0.17	0.18	0.18	0.16	0.17	0.14	0.15	0.14	0.17	0.16	0.16	0.13	0.16

NOTES: Sample descriptions:

1, 2 GSWA 204962 from 78.4 m in YD09-01
3–7 GSWA 204964 from 82.7 m in YD09-01
8, 9 GSWA 204965 from 86.4 m in YD09-01
10–14 GSWA 204969 from 110.3m in YD09-01
15, 16 GSWA 204945 from 121.3 m in YD09-01
17, 18 GSWA 204980 from 143.8 m in YD09-01
19, 20 GSWA 204981 from 143.8 m in YD09-01
21–24 GSWA 208058 from 389.9 m in YD09-03
25–28 GSWA 208026 from 427.2 m in YRC10-13D
29, 30 GSWA 208118 from 206.5 m in YRC09-01D
31, 32 GSWA 208121 from 235.4 m in YRC09-01D
33–36 GSWA 208123 from 244.2 m in YRC09-01D
37 GSWA 208124 from 246.1 m in YRC09-01D
38 GSWA 208125 from 250.7 m in YRC09-01D
39–43 GSWA 208127 from 251.5 m in YRC09-01D

Table 5. Amphibole analyses 1–14

Analysis no.	*1*	*2*	*3*	*4*	*5*	*6*	*7*	*8*	*9*	*10*	*11*	*12*	*13*	*14*
SiO_2	54.52	56.27	53.93	53.40	58.08	60.78	56.78	51.93	49.95	49.75	54.33	55.18	53.54	54.50
TiO_2	0.03	0.01	0.04	0.01	0.04	0.01	0.03	0.23	0.19	0.21	0.00	0.00	0.03	0.01
Al_2O_3	0.89	0.86	0.94	1.18	0.61	0.64	0.77	6.50	6.96	6.94	0.00	0.00	1.46	0.70
FeO	25.35	23.43	26.17	22.65	20.50	18.73	21.49	21.62	23.33	23.02	19.08	18.89	26.31	26.17
MnO	0.22	0.15	0.21	0.22	0.22	0.24	0.25	0.11	0.14	0.11	0.00	0.00	1.00	1.32
MgO	17.59	17.89	17.21	18.53	18.21	17.57	18.19	17.40	17.21	17.57	18.99	18.82	16.92	16.51
CaO	0.32	0.28	0.28	1.72	1.00	0.87	0.99	0.68	0.72	0.78	0.00	0.00	0.10	0.20
Na_2O	0.55	0.57	0.58	0.47	0.42	0.40	0.56	1.30	1.32	1.41	0.00	0.00	0.45	0.42
K_2O	0.00	0.00	0.00	0.00	0.00	0.00	0.00	0.00	0.00	0.01	0.00	0.00	0.00	0.01
P_2O_5	0.03	0.06	0.01	1.26	0.81	0.64	0.80	0.14	0.12	0.14	0.00	0.00	0.04	0.02
SO_3	0.51	0.51	0.64	0.55	0.11	0.10	0.13	0.08	0.08	0.07	0.00	0.00	0.13	0.15
Mg#	0.56	0.59	0.55	0.60	0.62	0.64	0.61	0.60	0.58	0.59	0.65	0.65	0.54	0.54

Table 5. Amphibole analyses 15–28

Analysis no.	*15*	*16*	*17*	*18*	*19*	*20*	*21*	*22*	*23*	*24*	*25*	*26*	*27*	*28*
SiO_2	54.40	52.71	53.30	62.79	56.39	63.88	54.70	55.09	54.35	54.27	53.31	54.03	53.54	53.73
TiO_2	0.00	0.01	0.02	0.02	0.00	0.00	0.00	0.00	0.04	0.01	0.02	0.00	0.08	0.08
Al_2O_3	0.55	1.16	0.87	0.50	1.17	0.56	0.96	0.94	1.34	0.96	0.92	0.96	2.23	1.96
FeO	26.96	32.16	31.34	20.54	25.01	19.34	26.51	26.38	27.57	27.51	31.69	29.40	27.24	27.02
MnO	1.04	0.61	0.62	0.83	1.00	0.72	1.31	0.95	0.54	0.85	0.41	0.89	0.46	0.49
MgO	16.40	12.53	12.94	14.69	15.77	14.62	15.81	15.84	15.23	15.68	12.78	13.87	15.49	15.85
CaO	0.20	0.18	0.13	0.07	0.21	0.08	0.16	0.19	0.18	0.16	0.16	0.20	0.14	0.15
Na_2O	0.36	0.53	0.57	0.36	0.31	0.39	0.41	0.43	0.56	0.43	0.53	0.47	0.60	0.55
K_2O	0.00	0.00	0.00	0.00	0.01	0.00	0.00	0.00	0.00	0.00	0.00	0.00	0.01	0.01
P_2O_5	0.00	0.01	0.03	0.05	0.04	0.12	0.01	0.06	0.05	0.00	0.00	0.00	0.07	0.05
SO_3	0.11	0.09	0.16	0.14	0.09	0.29	0.11	0.12	0.15	0.11	0.17	0.19	0.14	0.11
Mg#	0.53	0.42	0.43	0.57	0.54	0.58	0.53	0.53	0.51	0.51	0.43	0.47	0.51	0.52

Table 5. Amphibole analyses 29–42

Analysis no.	*29*	*30*	*31*	*32*	*33*	*34*	*35*	*36*	*37*	*38*	*39*	*40*	*41*	*42*
SiO_2	53.45	54.66	54.33	54.90	54.92	54.19	53.85	53.31	51.82	51.08	53.10	53.73	54.64	53.84
TiO_2	0.10	0.04	0.04	0.07	0.04	0.08	0.08	0.09	0.09	0.03	0.09	0.08	0.04	0.09
Al_2O_3	2.14	1.33	1.61	1.55	1.31	1.72	2.10	2.45	4.41	5.02	3.77	3.03	1.88	3.57
FeO	27.00	27.84	27.53	27.34	27.01	28.14	26.51	27.46	23.50	24.37	22.55	25.60	25.61	25.13
MnO	0.48	0.39	0.42	0.36	0.42	0.32	0.50	0.47	0.34	0.40	0.33	0.65	0.75	0.60
MgO	15.89	15.03	15.25	14.90	15.71	14.69	16.17	15.38	18.91	18.01	19.04	15.74	16.03	15.53
CaO	0.13	0.15	0.19	0.17	0.11	0.18	0.08	0.11	0.19	0.25	0.19	0.26	0.36	0.28
Na_2O	0.57	0.46	0.50	0.53	0.43	0.58	0.53	0.65	0.72	0.74	0.74	0.71	0.52	0.72
K_2O	0.01	0.00	0.00	0.00	0.00	0.00	0.01	0.00	0.01	0.04	0.05	0.00	0.00	0.00
P_2O_5	0.07	0.02	0.05	0.08	0.00	0.03	0.04	0.00	0.00	0.00	0.03	0.07	0.06	0.09
SO_3	0.16	0.08	0.07	0.11	0.06	0.09	0.13	0.09	0.00	0.07	0.11	0.13	0.12	0.15
Mg#	0.52	0.50	0.51	0.50	0.52	0.49	0.53	0.51	0.60	0.58	0.61	0.53	0.54	0.53

Table 5. Amphibole analyses 43–56

Analysis no.	*43*	*44*	*45*	*46*	*47*	*48*	*49*	*50*	*51*	*52*	*53*	*54*	*55*	*56*
SiO_2	52.14	55.22	54.98	55.64	54.85	55.39	55.81	55.80	55.99	55.18	52.02	51.12	53.89	54.03
TiO_2	0.04	0.11	0.10	0.02	0.02	0.04	0.04	0.03	0.04	0.04	0.01	0.00	0.06	0.04
Al_2O_3	4.11	1.22	1.23	0.42	1.12	1.40	1.56	1.45	1.47	2.45	1.46	1.38	1.81	1.98
FeO	26.10	23.47	23.64	23.83	24.91	21.30	19.91	21.55	19.81	21.10	23.77	24.02	18.31	18.01
MnO	0.70	0.19	0.22	0.24	0.26	0.16	0.15	0.17	0.24	0.32	0.48	0.53	0.22	0.20
MgO	15.93	18.76	18.89	18.43	17.86	20.51	21.46	19.96	21.08	19.40	19.87	20.21	24.48	24.36
CaO	0.30	0.12	0.10	0.30	0.12	0.13	0.14	0.12	0.25	0.29	0.34	0.23	0.25	0.25
Na_2O	0.48	0.46	0.43	0.43	0.41	0.51	0.53	0.52	0.61	0.75	0.63	0.62	0.67	0.68
K_2O	0.00	0.00	0.00	0.00	0.00	0.00	0.01	0.00	0.00	0.00	0.00	0.00	0.00	0.00
P_2O_5	0.09	0.07	0.06	0.25	0.10	0.15	0.14	0.14	0.08	0.04	0.33	0.24	0.01	0.03
SO_3	0.09	0.38	0.35	0.42	0.34	0.40	0.25	0.26	0.43	0.45	1.10	1.65	0.30	0.43
Mg#	0.53	0.60	0.60	0.59	0.57	0.64	0.67	0.63	0.66	0.63	0.61	0.61	0.71	0.72

NOTE: See page 34 for Table 5 notes.

TABLE 5 NOTES: Sample descriptions:

1–3	polysynthetically twinned cross-cutting cummingtonite crystals in banded silicate facies banded iron-formation (BIF); GSWA 204970 from 111.0 m in YD09-01
4	crosscutting cummingtonite crystals associated with ragged apatite; above sample
5–7	fine-grained matted fibrous amphibole crystals; above sample
8–10	small clear crystals; silicate facies BIF; GSWA 204973 from 123.4 m in YD09-01
11, 12	large rounded cloudy amphiboles; above sample
13–15	large polysynthetically twinned cummingtonite crystals, BIF; GSWA 208020 from 406.4 m in YRC10-13D
16, 17	small untwinned prismatic crystals; above sample
18–20	curved fibrous asbestiform crystals; above sample
21–24	small polysynthetically twinned prismatic amphiboles; above sample
25–26	long fibrous anthophyllite crystal; above sample
27–29	radial aggregate of fibrous anthophyllite associated with cordierite; altered basaltic hyaloclastite; GSWA 208027 from 429.0 m in YRC10-13D
30–34	thin prismatic crystals along fracture in chert; above sample
35, 36	fibrous anthophyllite crystals in cordierite; above sample
37–39	fibrous crystals of anthophyllite intergrown with biotite; altered basaltic hyaloclastite; GSWA 208028 from 431.0 m in YRC10-13D
40–43	small acicular crystals of anthophyllite; altered basaltic hyaloclastite; GSWA 208030 from 436.3 m in YRC10-13D
44–47	matted intergrowth of colourless fine-grained acicular anthophyllite in weakly mineralized hyaloclastite, GSWA 208058 from 398.9 m in YD09-03
48–50	crosscutting crystal of anthophyllite; above sample
51, 52	remnants of anthophyllite partly replaced by fibrous amphibole; GSWA 208124 from 246.1 m in YD09-01D
53, 54	small prismatic anthophyllite crystal; BIF slump breccia; GSWA 208127 from 251.6 m in YD09-01D
55, 56	small prismatic anthophyllite crystal; above sample

In the BIF directly below mineralization in YRC10-13D, large (up to 4 mm long) crystals of polysynthetically twinned cummingtonite cut across the laminations almost perpendicular to some of the BIF laminae. These cummingtonite crystals have incorporated layers of fine-grained magnetite from the BIF. They are fractured and partially bent and displaced: sulfides infill the fractures in places (Fig. 42). Other laminae have finer grained prismatic cummingtonite crystals. In other parts of the same thin section, layers with curved fibrous asbestiform crystals of anthophyllite are cut by prismatic cummingtonite crystals (Fig. 43). Chemically, the cummingtonite and anthophyllite are very similar: both are low in Ca and Al and have 0.6 – 1.3% Mn. The Mg# of the cummingtonite is variable (0.41 – 0.54) (analyses 13–17, 21–24, Table 5) as is the Mg# of the anthophyllite (0.43 – 0.58) (analyses 18–20, 25–26, Table 5).

Further downhole in YRC10-13D, highly altered basaltic hyaloclastites containing radiating aggregates of acicular crystals of anthophyllite exist in a matrix of cordierite within fragments (Fig. 44). Anthophyllite is also present along fractures in chert infilling the matrix between fragments (Fig. 45). In places anthophyllite is also intergrown with biotite (Fig. 46). The anthophyllite associated with both the cordierite and chert is similar in composition with Mg# of 0.49 – 0.53, low Ca, and 1.3 – 2.4% Al_2O_3 (analyses 28–36, Table 5). However, the anthophyllite associated with the biotite has Mg# of 0.58 – 0.61, and 3.0 – 5.0% Al_2O_3 substituting for SiO_2 in the lattice (analyses 37–39, Table 5).

Initially, all amphiboles in the TSG TIR spectral library except kaersutite, tschermakite, holmquistite, arfvedsonite, glaucophane, and riebeckite were enabled when analysing the TIR data. Later, gedrite, edenite-1, edenite-2, and amphibole ML48 were turned off (see Appendix 3) as no gedrite or edenite were present in thin section and amphibole ML48 was a mineral specimen of uncertain composition, possibly anthophyllite in the CSIRO collection. Then, the only amphiboles remaining in the TSG library for matching spectra were hornblende, ferrohornblende, actinolite, grunerite–cummingtonite, manganocummingtonite, and anthophyllite. Not surprisingly, the most abundant amphiboles detected in YRC10-13D were in the mafic intrusive rocks and consisted of hornblende, ferrohornblende, and actinolite (Fig. 47b). In order to show the distribution of the Ca-poor amphiboles downhole, the weighted average of the first, second, and third minerals downhole were plotted. The weighted grunerite–cummingtonite plot registered 23 points in total, mostly where anthophyllite had been observed although there were only two points in the BIF where cummingtonite was abundant (Fig. 47c). The weighted manganocummingtonite plot registered 59 points in the hyaloclastites where anthophyllite was abundant although it did not register any in the BIF (Fig. 47d). Only 12 points are in the weighted anthophyllite plot, of which 11 plot where abundant anthophyllite was observed (Fig. 47e). Spectral matching of the SWIR data against the USGS spectra for anthophyllite and cummingtonite gave large numbers of false positives in the intrusive rocks and very few points where anthophyllite and cummingtonite existed (Fig. 47f,g). The plot of the 980 nm wavelength absorption feature gave positive results in both the BIF where cummingtonite was abundant and in the altered hyaloclastite where anthophyllite was abundant and gave no false positives; the 980 nm wavelength absorption feature also gave a significant number of results (657 points) and was therefore used as a proxy for Ca-poor amphiboles in Appendix 6g and in the remainder of the drillholes.

BIF in YD09-01 contained large polysynthetically twinned cummingtonite crystals similar to those shown in Figure 42 for YRC10-13D. The cummingtonite crystals in YD09-01 were also chemically similar to those in YRC10-13D, apart from marginally higher Mg# (0.55 – 0.60) and less Mn (analyses 1–4, Table 5); analysis 4 has 1.72% CaO but the presence of P_2O_5 indicates that some or all of the CaO comes from scatter from the adjacent apatite. Other samples of silicate-facies

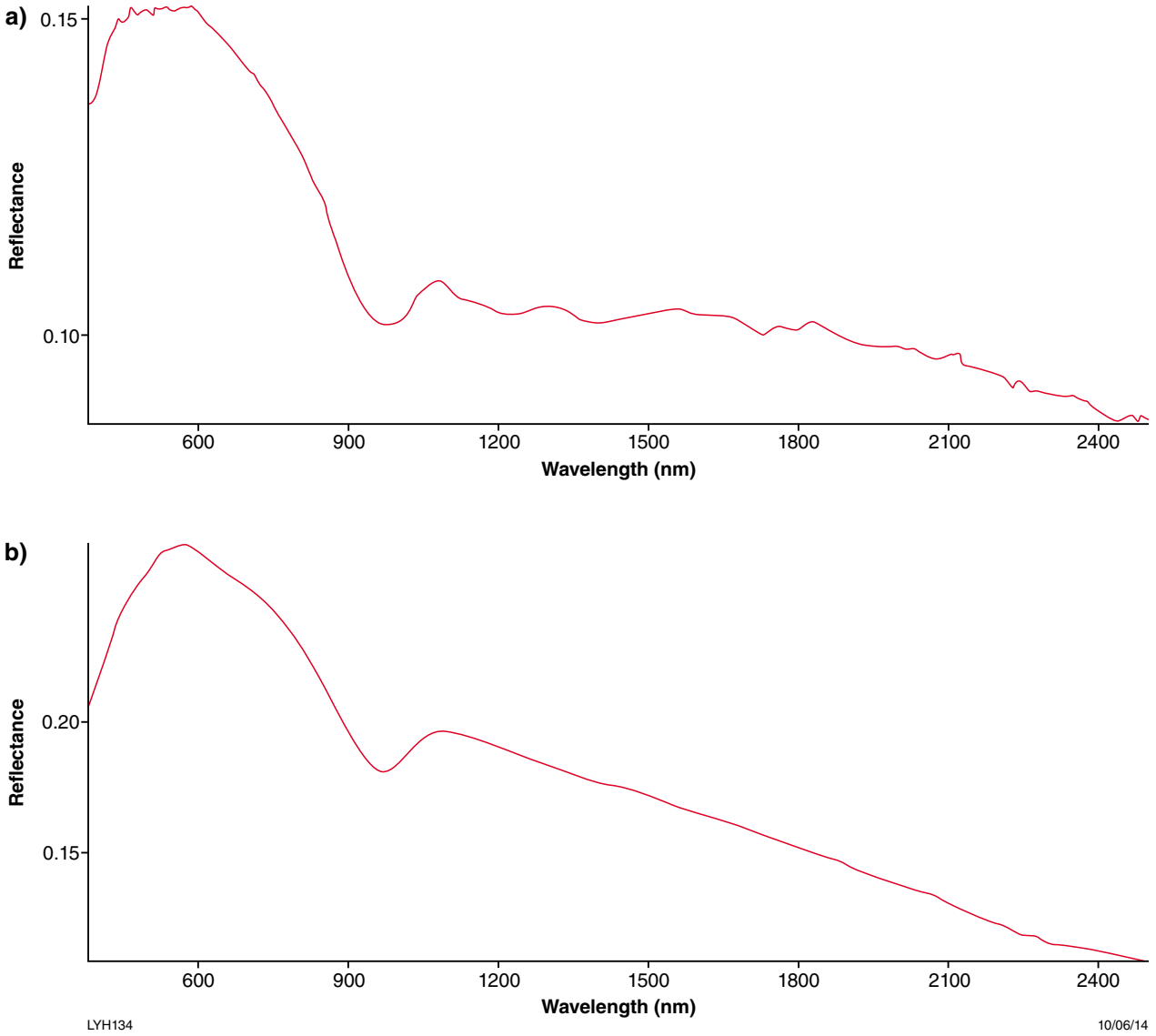

Figure 41. **The 980 nm absorption feature in short wave infrared (SWIR) spectra: a) spectrum from interval with large cummingtonite crystals (406.43 m in YRC10-13D); b) spectrum from interval with abundant anthophyllite, (429.07 m in YRC10–13D)**

iron-formation were composed of rounded to elongate cloudy fibrous cummingtonite crystals (Fig. 48), which possibly replaced early greenalite as in the granular iron-formation of the Minnesota–Ontario area (Floran and Papike, 1978). Some interstitial small, clear, colourless cummingtonite crystals in the iron formation appear to have crystallized later (Fig. 48). The cloudy cummingtonite had low Al_2O_3 and Na_2O and Mg# of 0.65 (analyses 11–12, Table 5) whereas the clear cummingtonite crystals contained 6.5 – 7.0% Al_2O_3, 1.3 – 1.4% Na_2O, and Mg# of 0.58 – 0.60 (analyses 8–10, Table 5). The plot of the amphibole 980 nm absorption feature (Appendix 4g) downhole in YD09-01 indicates that the Ca-poor amphiboles are most abundant in the BIF as suggested by the petrologic work, and less abundant in the nearby tuff or hyaloclastite and basalt.

In YD09-03, the plot of the amphibole 980 nm absorption feature (Appendix 5g) shows strong development near mineralization. In this interval, fine-grained acicular anthophyllite replaces chlorite (Fig. 49) and larger crystals of anthophyllite crosscut chloritic hyaloclastite fragments (Fig. 50). The fine-grained acicular anthophyllite had a Mg# of 0.57 – 0.60 (analyses 44–47, Table 5) whereas the larger anthophyllite crystal has Mg# of 0.63 – 0.67 (analyses 48–50, Table 5). The plot of the 980 nm absorption feature (Appendix 5g) also suggested that Ca-poor amphiboles are present in altered andesitic hyaloclastite 260 m above the main Just Desserts – Trajan mineralized horizon in YD09-03. Petrographic examination confirmed the presence of polysynthetically twinned cummingtonite infilling cavities within this zone (Fig. 51).

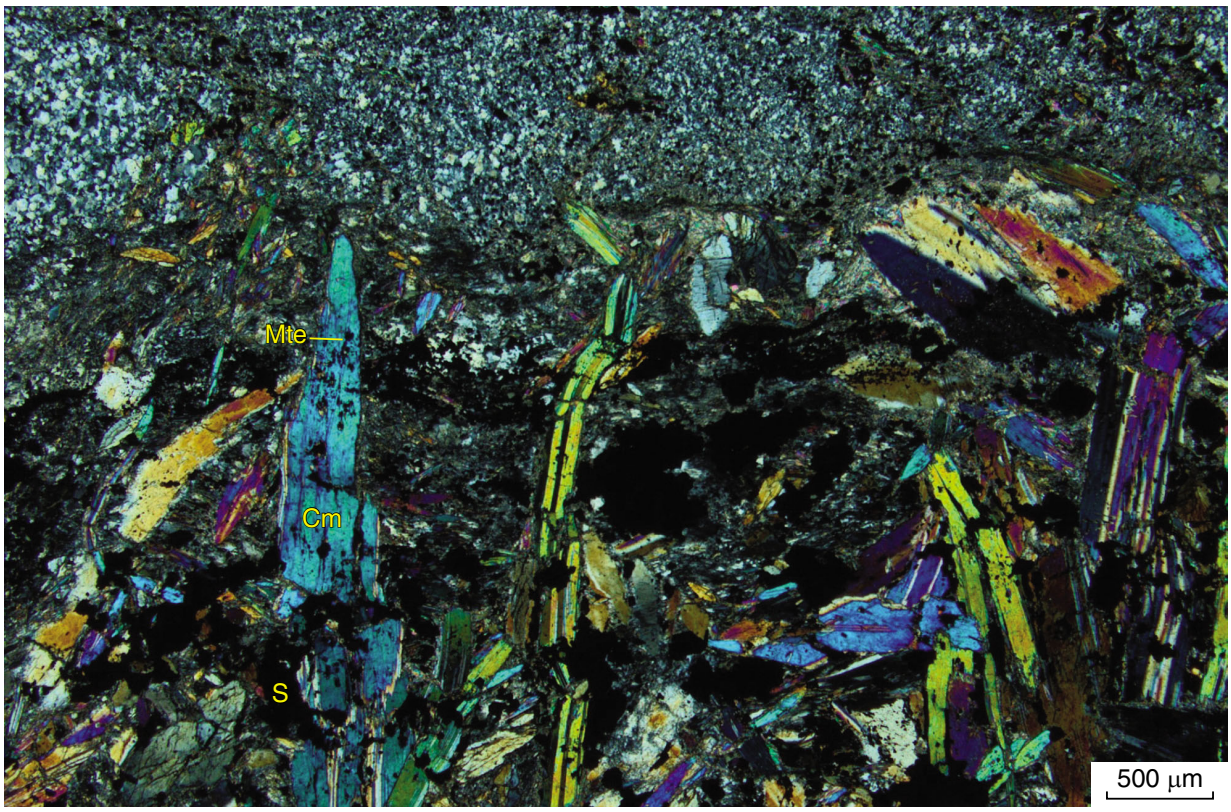

LYH135 08/04/14

Figure 42. **Large crystals of polysynthetically twinned cummingtonite (Cm) cutting perpendicularly across the laminations of BIF. These cummingtonite crystals have incorporated layers of fine-grained magnetite (Mte) from the banded iron-formation (BIF). They are fractured, partially bent, and are displaced; sulfides (S) infill the fractures in places (GSWA 208020 from 406.4 m on YRC10-13D); crossed polars**

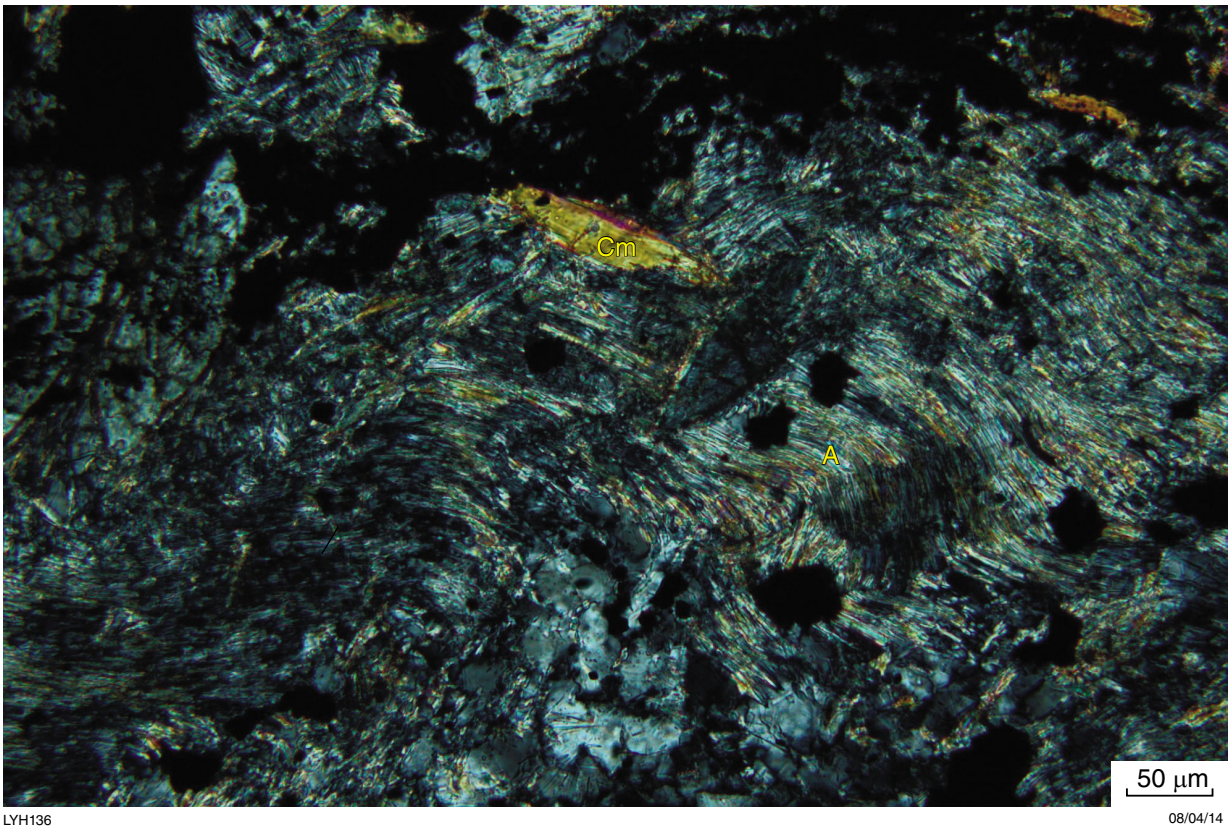

LYH136 08/04/14

Figure 43. **Curved fibrous asbestiform crystals of anthophyllite (A) cut by prismatic cummingtonite (Cm) crystals (same sample as Fig. 42); crossed polars**

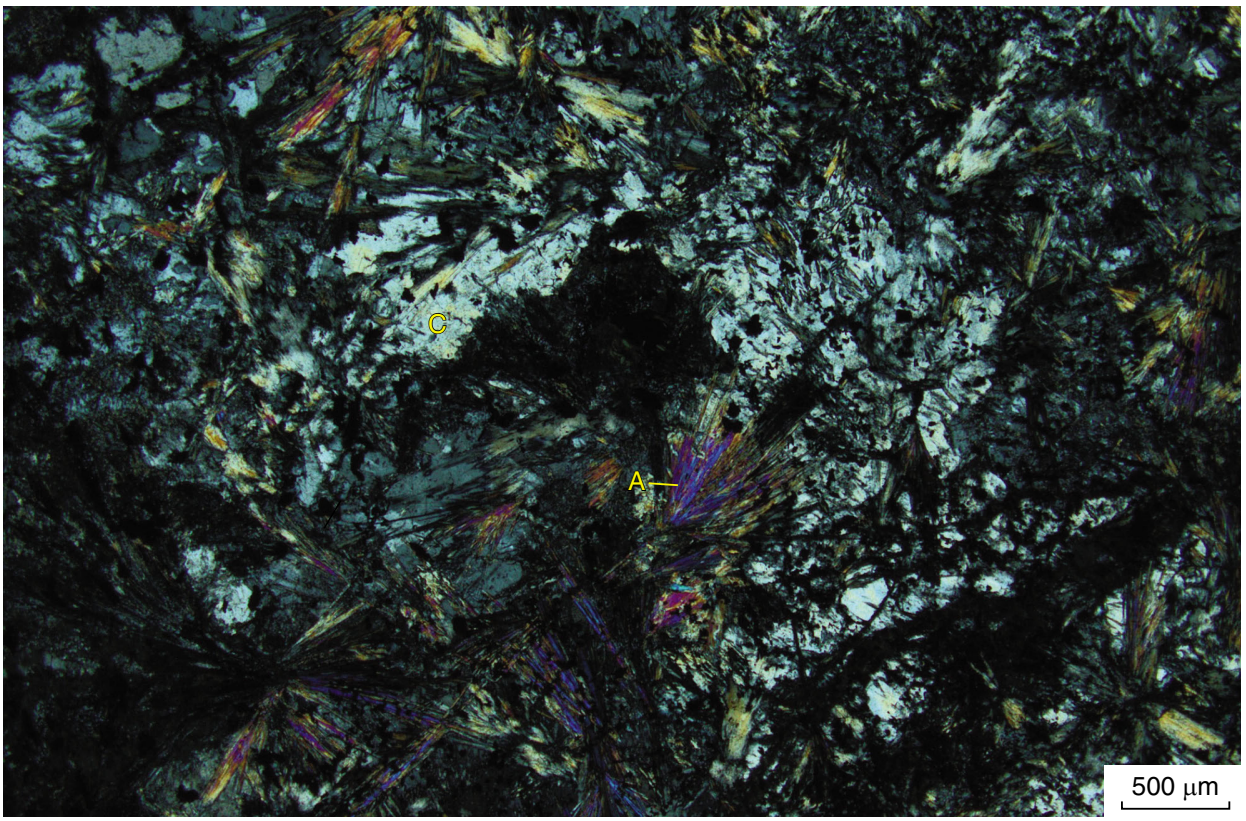

Figure 44. Radial aggregates of acicular anthophyllite (A) crystals in matrix of cordierite (C) in highly altered hyaloclastite (GSWA 208027 from 429.0 m in YRC10-13D); crossed polars

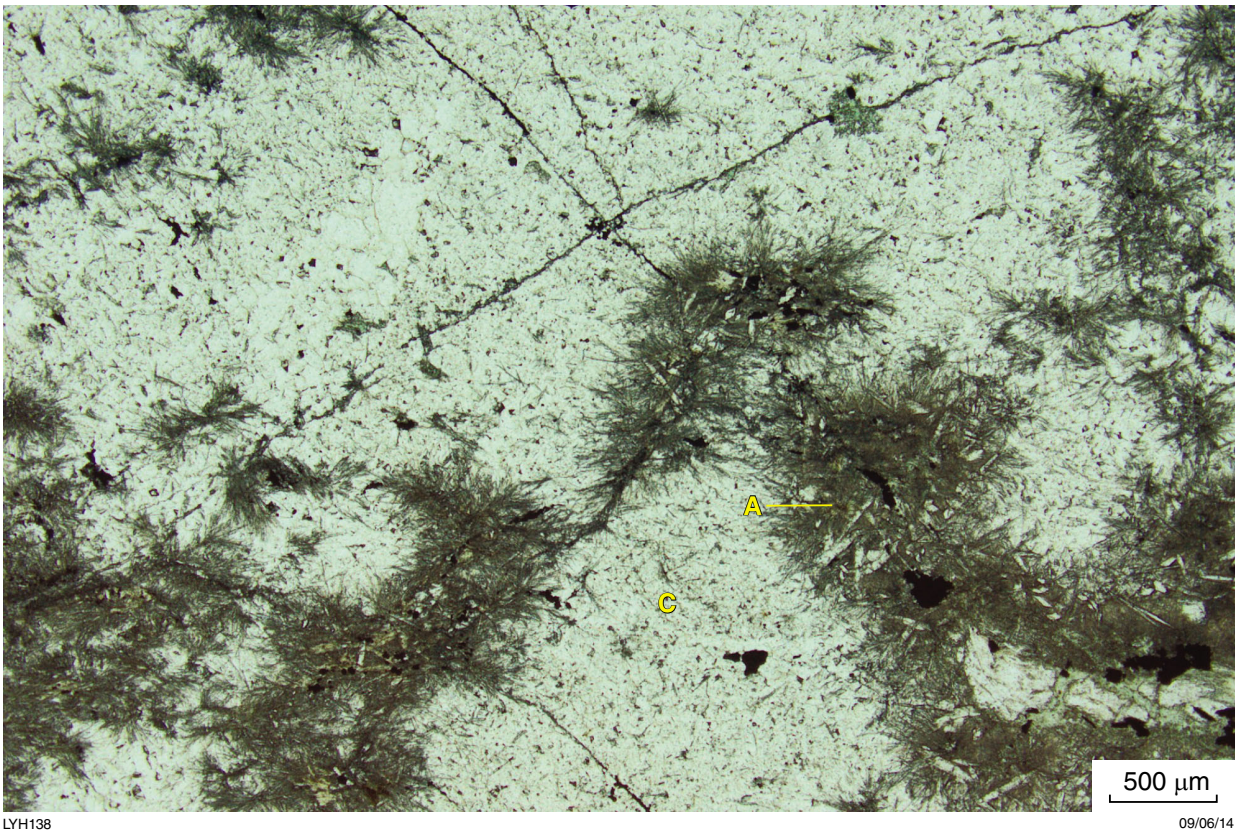

Figure 45. Acicular anthophyllite (A) developed along fractures in chert (C) infilling spaces between fragments in hyaloclastite (same sample as Fig. 43); plane-polarized light

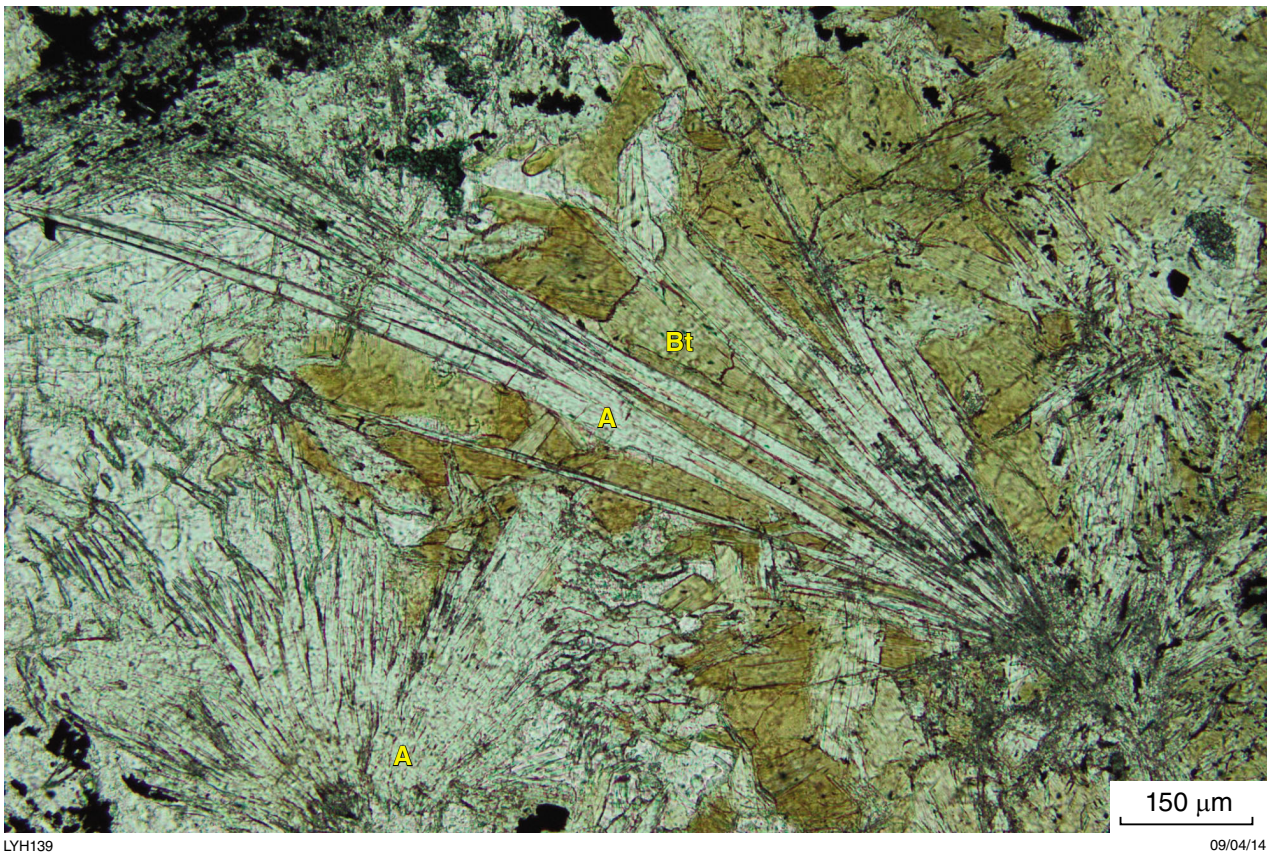

Figure 46. Anthophyllite (A) intergrown with biotite (Bt) (GSWA 208028, 431.0 m, YRC10-13D); plane-polarized light

The plot of the amphibole 980 nm absorption feature for YRC09-01D suggested that the greatest concentration of Ca-poor amphiboles was in the basalt beneath the C Zone. Petrologic examination of these basalts showed polysynthetically twinned cummingtonite associated with chlorite in small amygdales within the least altered basalt (Fig. 3) and radiating aggregates of anthophyllite associated with cordierite and tabular cummingtonite crystals in highly altered basalt. The brecciated BIF associated with mineralization contains small clear cummingtonite crystals surrounded by talc (Fig. 52). These crystals have the highest Mg# of all the amphiboles analysed (0.61 – 0.72; analyses 51–56, Table 5), although these results may be affected by scatter from the surrounding talc.

In YD10-01 from the Augustus prospect, there is no significant development of Ca-poor amphiboles, with only 12 points registered on the amphibole 980 nm absorption feature plot. None of these was associated with mineralization or BIF (Appendix 8g).

Figure 47. (facing) Comparative plots of amphiboles in YRC10-13D vs lithology (colours are relative indications of certainty: red, high; dark blue, low): a) lithology; b) plot of all amphiboles recorded as mineral 1 in thermal infrared (TIR) spectra; c) weighted plot of grunerite–cummingtonite in TIR; d) weighted plot of manganocummingtonite in TIR; e) weighted plot of anthophyllite in TIR; f) match against the USGS short wave infrared (SWIR) spectral library for anthophyllite; g) match against the USGS SWIR spectral library for cummingtonite; h) plot of spectral match with 980 nm absorption feature

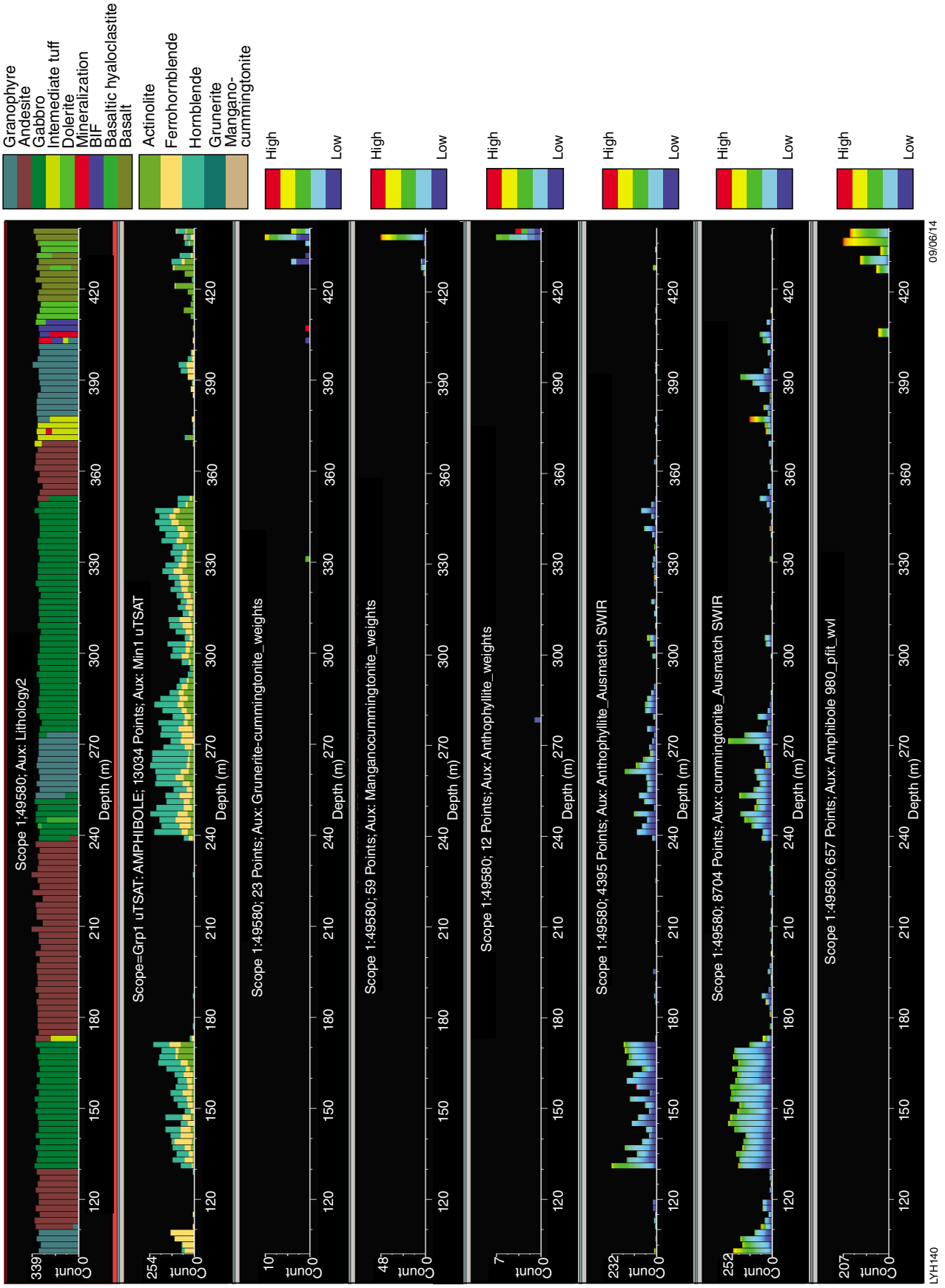
Granophyre
Andesite
Gabbro
Intemediate tuff
Dolerite
Mineralization
BIF
Basaltic hyaloclastite
Basalt
Actinolite
Ferrohornblende
Hornblende
Grunerite
Mangano-cummingtonite
High
Low
a)
Scope 1;49580; Aux: Lithology2
b)
Scope=Grp1 uTSAT: AMPHIBOLE; 13034 Points; Aux: Min1 uTSAT
c)
Scope 1:49580; 23 Points; Aux: Grunerite-cummingtonite_weights
d)
Scope 1:49580; 59 Points; Aux: Manganocummingtonite_weights
e)
Scope 1:49580; 12 Points; Aux: Anthophyllite_weights
f)
Scope 1:49580; 4395 Points; Aux: Anthophyllite_Ausmatch SWIR
g)
Scope 1:49580; 8704 Points; Aux: cummingtonite_Ausmatch SWIR
h)
Scope 1:49580; 657 Points; Aux: Amphibole 980_pfit_wvl
Count
Depth (m)
09/06/14
LYH140

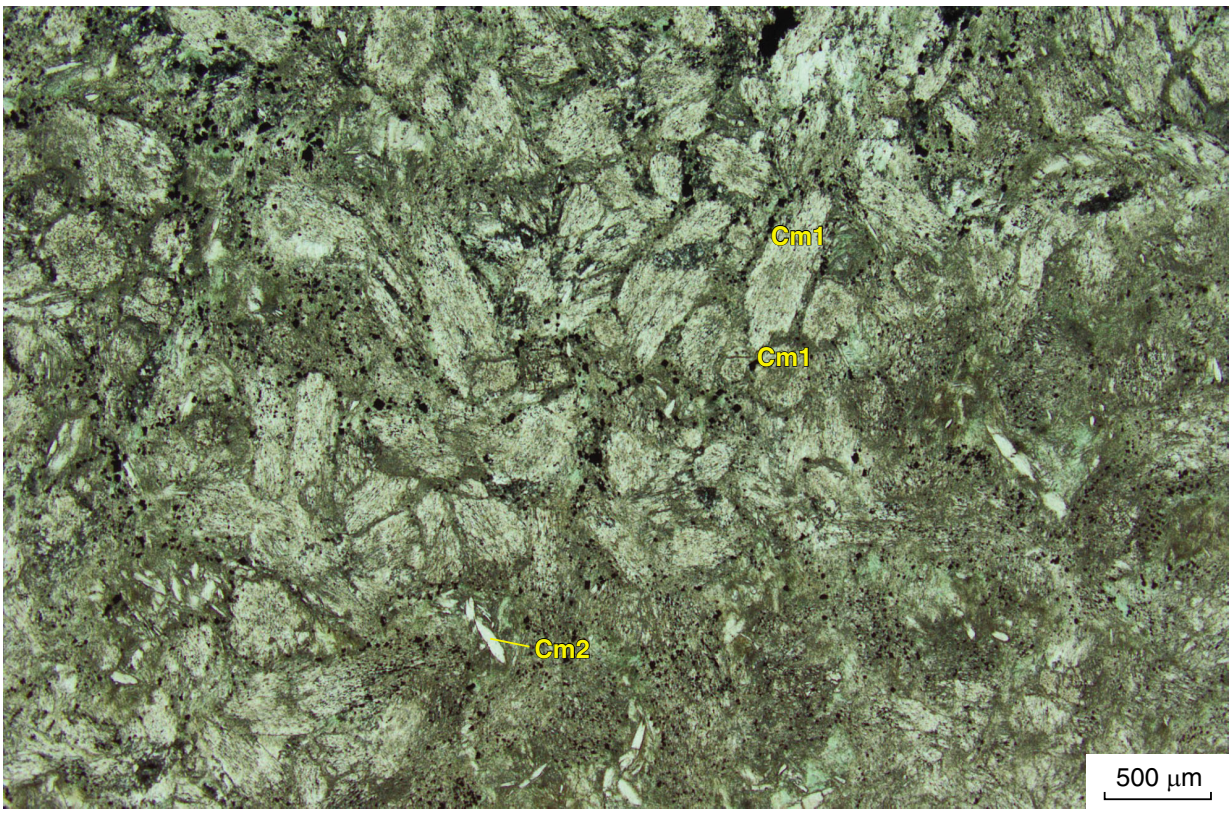

LYH141 09/04/14

Figure 48. **Iron formation composed of rounded to elongate cloudy fibrous cummingtonite (Cm1) crystals with a few small clear, colourless interstitial cummingtonite (Cm2) crystals (GSWA 204973 from 123.4 m in YD09-01); plane-polarized light**

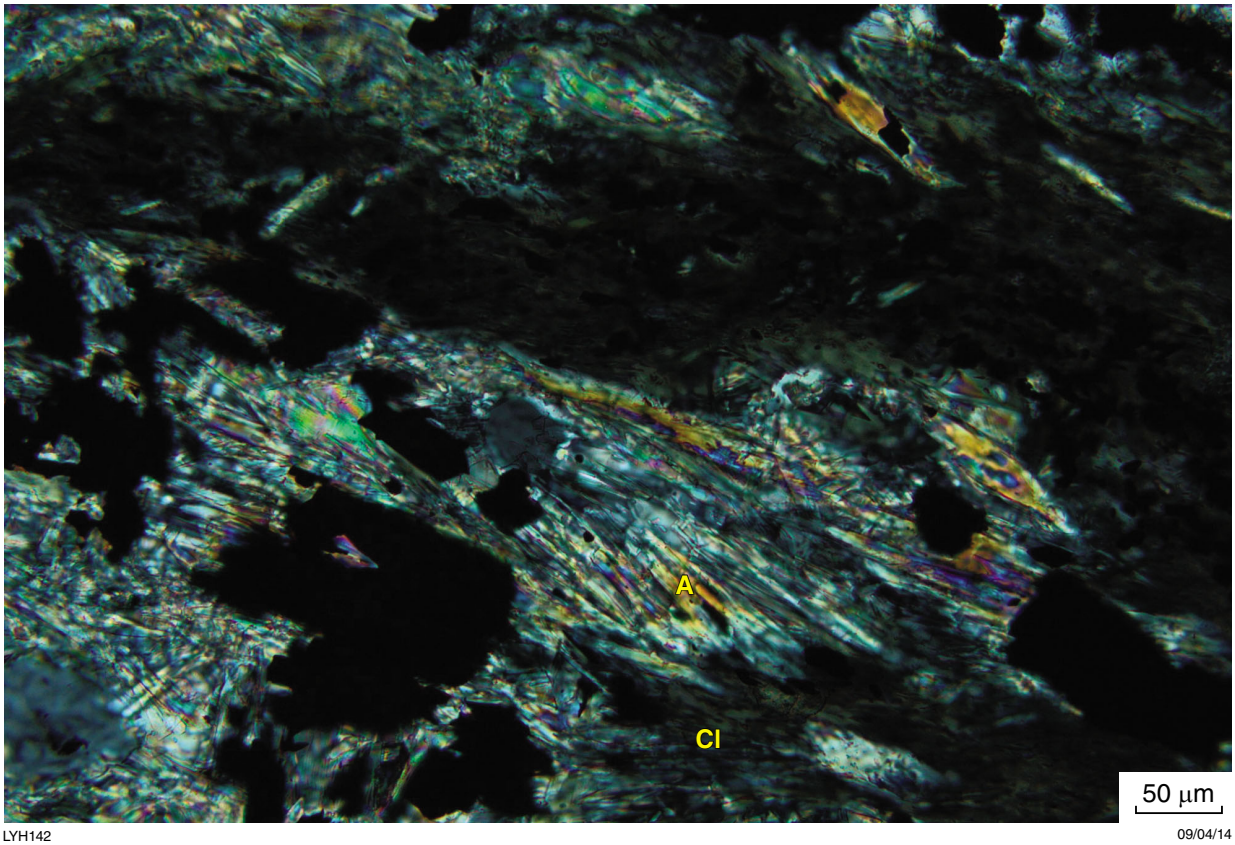

LYH142 09/04/14

Figure 49. **Fine-grained acicular anthophyllite (A) replacing chlorite (Cl) in weakly mineralized hyaloclastite (GSWA 208058 from 389.9 m in YD09-03); crossed polars**

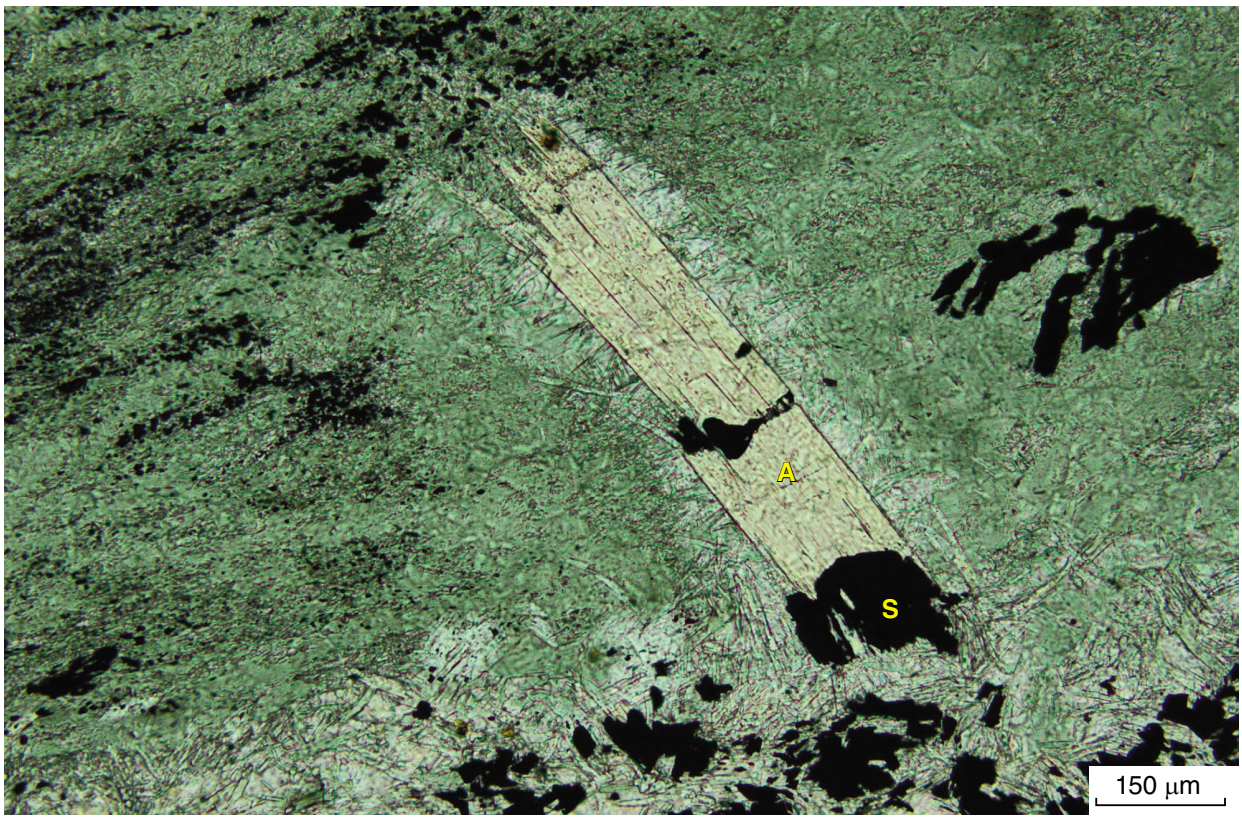

Figure 50. Anthophyllite (A) crystal cutting across chloritic hyaloclastite fragment; anthophyllite is partially replaced by sulfides (S) (GSWA 208058 from 389.9 m in YD09-03); plane-polarized light

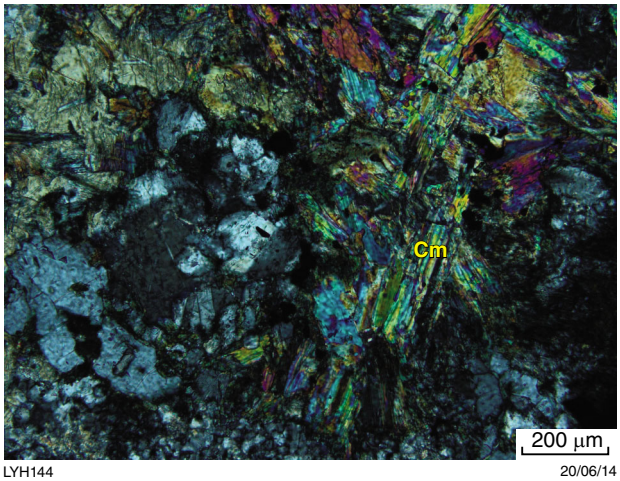

Figure 51. Polysynthetically twinned cummingtonite (Cm) infilling cavity in very altered hyaloclastite (GSWA 208077 from 122.9 m in YD09-03); crossed polars

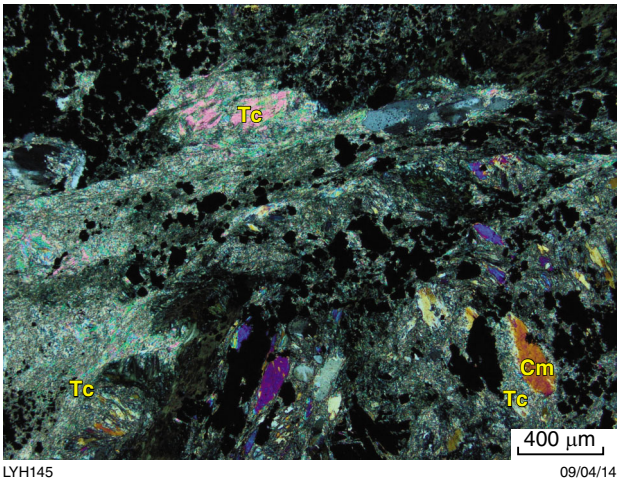

Figure 52. Small prismatic crystals of cummingtonite (Cm) surrounded by talc (Tc) in banded iron-formation (BIF) breccia (GSWA 208127 from 251.6 m in YRC09-01D); plane-polarized light

Cordierite

Cordierite was associated with anthophyllite in highly altered basaltic hyaloclastite beneath the Trajan mineralization in YRC10-13D (Fig. 44), and in highly altered basalts beneath the C Zone in YRC09-01D. Unfortunately the TIR spectra for cordierite shares its main reflectance feature at 10 267 nm with hornblende and its second main reflectance feature at 8177 nm with quartz, so no meaningful distribution of cordierite downhole could be obtained. Thus, cordierite was 'turned off' in TSG in order to prevent its being shown everywhere that hornblende and quartz were present. The cordierite is an iron-rich variety as indicated by SEM analysis (Table 6).

Silica

Silica alteration is widespread throughout the stratigraphic succession at Yuinmery (Appendices 4a, 5a, 6a, 7a, and 8a), especially in the volcanic rocks above and below mineralization where feldspars are commonly almost completely replaced by quartz and a little chlorite, carbonate, sericite, or epidote. It is difficult to determine whether this alteration took place during mineralization or at the time of regional metamorphism. However, in YRC09-01D, the basalts show a gradual decrease in quartz and increase in plagioclase downhole (Appendix 7a), suggesting that at least some of the silica alteration was related to mineralization. The presence of unaltered plagioclase in the andesite intruding the altered basalts at the Just Desserts prospect in YD09-01 (Appendix 4a) is also evidence that the alteration pre-dated the intrusion of the andesite and was associated with mineralization. The matrix of many of the hyaloclastites has been flooded by silica. Vesicles in the andesites and basalts have been mainly filled by silica along with small amounts of chlorite, amphiboles, and sulfides (Figs 4, 14 and 16c).

Layers of chert form an integral part of the BIF (Fig. 12). Where sulfides infill fractures in some chert horizons, the chert has been partly recrystallized to quartz, although in places retains colloidal characteristics (Fig. 30).

Carbonates

Carbonates make up a relatively minor percentage of the alteration minerals. They are present as crosscutting veinlets throughout the stratigraphic succession, including the mafic intrusive rocks. This indicates that carbonates typically post-date mineralization although small quantities of ferroan dolomite are related to mineralization (Fig. 53).

Staining of thin sections using the method of Dickson (1965) indicated that ferroan dolomite was the most abundant carbonate, although calcite, dolomite, ankerite (or ferroan calcite), and siderite were all identified. In many cases, several different carbonates were present in a single vein (Fig. 54). Early versions of TSG were unable to distinguish ferroan dolomite from dolomite or ankerite. However, the latest version of TSG (7.1.0.059) available at the time of writing can identify ferroan dolomite. TSG appears to give a reasonable indication of the downhole distribution of carbonates, although where mixtures are present it cannot distinguish the carbonates accurately. Because there are typically more points for carbonate as mineral 2 than mineral 1, mineral 2 is plotted in Appendices 4h, 5h, 6h, 7h, and 8h. There are no obvious systematic changes in the compositions of the carbonates with distance from mineralization.

Micas and brittle micas

The summary plots for TIR (Appendices 4a, 5a, 6a, 7a and 8a) and SWIR (Appendices 4b, 5b, 6b, 7b and 8b) suggest that white mica is a fairly minor alteration phase, although plots show little agreement on the distribution of white mica by the two methods. This lack of agreement is even more apparent when the downhole distribution of white mica for YD09-01 at Just Desserts is plotted for SWIR (Fig. 55b) and TIR (Fig. 55c). Mineral 2 was used in these plots because it yielded a greater number of points. The SWIR plot shows almost all of the white micas (predominantly muscovite) in the granophyre and intrusive andesite. The TIR plot shows the greatest concentration of

Table 6. Cordierite analyses

Analysis no.	*1*	*2*	*3*	*4*	*5*	*6*	*7*	*8*
SiO_2	46.32	46.52	46.40	47.85	47.49	47.51	50.31	48.49
Al_2O_3	33.78	33.57	33.84	34.38	34.14	34.05	32.21	32.01
FeO	10.04	9.97	10.09	7.48	7.53	8.27	7.87	9.10
MnO	0.15	0.17	0.18	0.08	0.07	0.11	0.00	0.00
MgO	8.86	8.74	8.62	9.53	9.80	9.39	9.61	9.61
CaO	0.07	0.12	0.06	0.10	0.04	0.06	0.00	0.00
Na_2O	0.64	0.82	0.68	0.49	0.83	0.54	0.00	0.80
K_2O	0.10	0.10	0.08	0.05	0.08	0.03	0.00	0.00
SO_3	0.03	0.00	0.05	0.05	0.00	0.03	0.00	0.00

NOTES: Sample descriptions:
1–6 GSWA 208027 from 429.0 m in YRC10-13D
7, 8 GSWA 208135 from 272.0 m in YD09-01D

white micas in the volcanic rocks and BIF, with muscovite dominating in the regions between mineralization and paragonite dominating beneath mineralization.

Most of the white mica in thin section is very fine grained. Some coarse-grained colourless to pale green crystals associated with mineralization that were originally considered as white mica turned out to be iron-bearing talc when analysed by SEM. Two small grains of muscovite containing a little sodium were, however, positively identified (analyses 1–6, Table 7). One of these was an inclusion in pyrite (Fig. 56). TSG interpreted paragonite at this location for both SWIR and TIR data. The SWIR spectra at this location gave an absorption feature at 2197 nm, which is consistent with the spectra of muscovite tending to paragonite given in Pontual (2008) and the SEM analyses. A flake of colourless to pale green mica from YD09-03 (Fig. 57) contained appreciable iron and magnesium, moderate sodium, and very low potassium (analyses 7–8, Table 7). TSG showed muscovite and paragonite in this interval for TIR and paragonite for SWIR. The SWIR absorption feature at 2191 nm suggested the flake was muscovite tending to paragonite according to the spectra in Pontual (2008). However, if this mineral were paragonite, it is unusually enriched in iron and magnesium and low in sodium. It could alternatively be a completely different, possibly undescribed, mica.

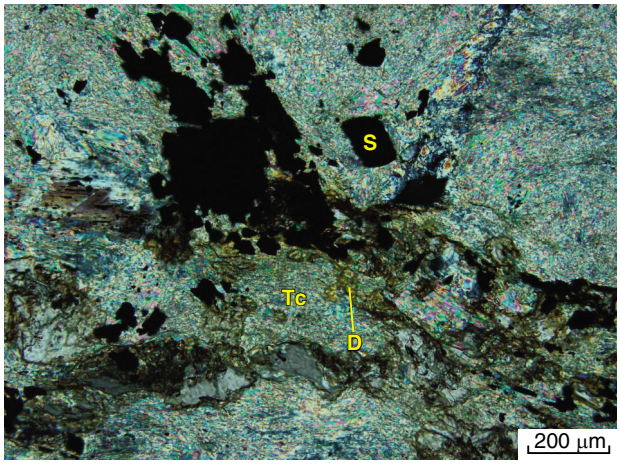

Figure 53. **Ferroan dolomite (D) associated with talc (Tc) and sulfides (S) from beneath the upper mineralized horizon at Just Desserts (GSWA 204964 from 82.7 m in YD09-01); crossed polars**

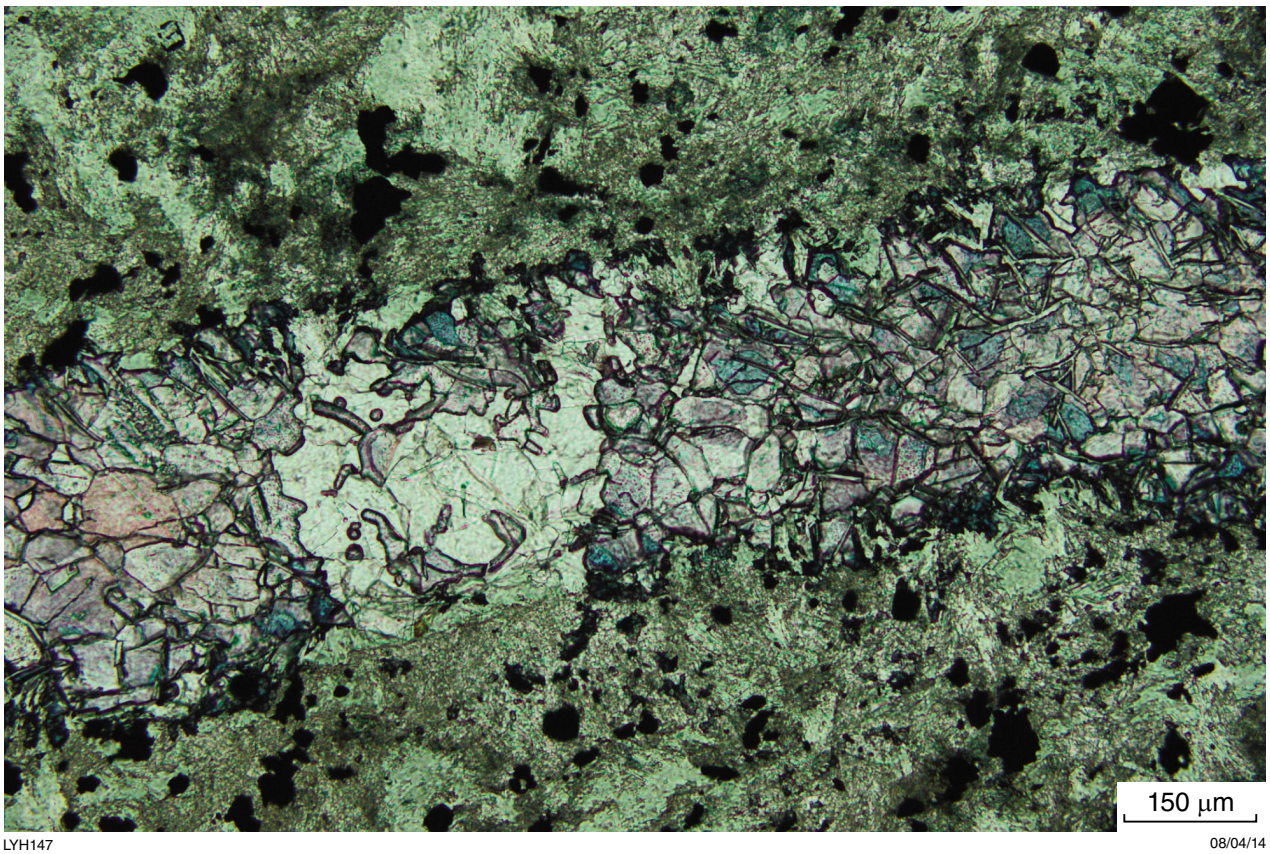

Figure 54. **Carbonate veinlet showing remnant ferroan dolomite (stained blue) replaced by ankerite or ferroan calcite (stained mauve) and calcite (stained pink), which in turn are replaced by colourless dolomite (unstained). From altered basalt beneath the C Zone (GSWA 206869 from 288.5 m in YRC09-01D); plane-polarized light**

Figure 55. **Downhole distribution of micas in YD09-01 from Just Desserts vs lithology: a) simplified lithology; b) short wave infrared (SWIR) spectroscopy of white micas; c) thermal infrared (TIR) spectroscopy of white micas; d) SWIR of dark micas; e) TIR of dark micas**

Table 7. Mica analyses

Analysis no.	*1*	*2*	*3*	*4*	*5*	*6*	*7*	*8*	*9*	*10*
SiO_2	47.09	46.88	47.09	45.01	45.53	45.03	42.83	42.75	35.66	37.32
TiO_2	0.36	0.40	0.21	0.33	0.55	0.41	0.18	0.17	0.85	0.94
Al_2O_3	38.40	38.35	38.70	38.24	37.09	38.45	40.06	40.04	17.00	16.80
FeO	1.82	1.81	1.97	2.19	2.48	2.04	4.95	5.09	22.42	20.44
MgO	0.56	0.66	0.68	0.58	0.69	0.46	9.39	9.26	14.68	13.92
CaO	0.11	0.13	0.12	0.10	0.11	0.11	0.09	0.13	0.05	0.08
Na_2O	1.53	1.24	1.93	1.37	1.07	1.33	2.26	2.35	0.30	0.44
K_2O	10.12	10.54	9.23	9.92	10.57	10.01	0.20	0.20	8.67	9.80
SO_3	0.00	0.00	0.07	2.27	1.92	2.17	0.03	0.00	0.00	0.01
Cl	0.01	0.00	0.00	0.00	0.00	0.00	0.00	0.01	0.36	0.24

NOTES: Sample descriptions:

1–6 white mica, GSWA 208133 from 265.0 m in YRC09-01D

7, 8 white mica, GSWA 208070b from 450.0 m in YD09-03

9, 10 dark mica intergrown with anthophyllite, GSWA 208028 from 431.0 m in YRC10-13D

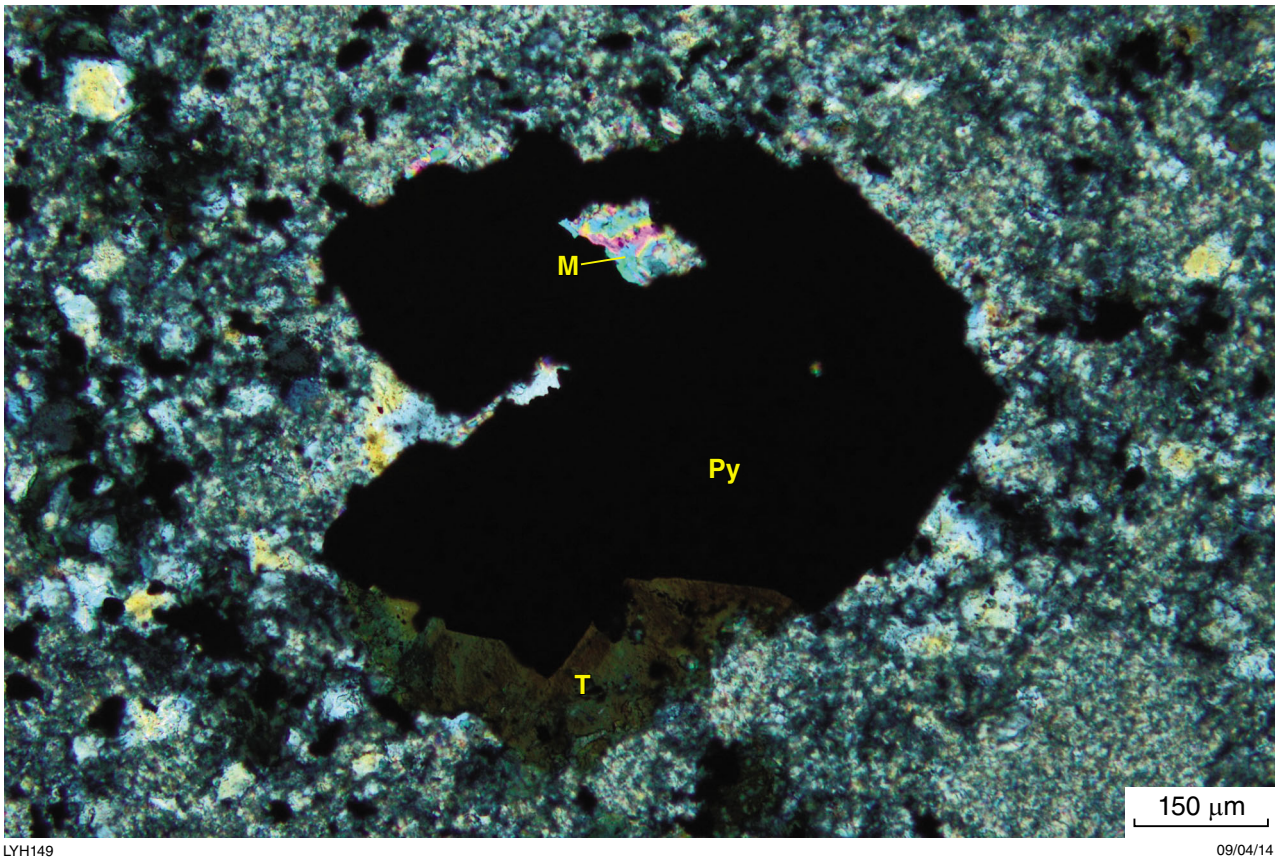

LYH149 09/04/14

Figure 56. Pyrite (Py) with inclusion of muscovite (M) from altered basalt below C Zone mineralization in YRC10-13D; the pyrite is fringed by blue to green tourmaline (T) (GSWA 208133 from 265.0 m in YRC10-13D; crossed polars

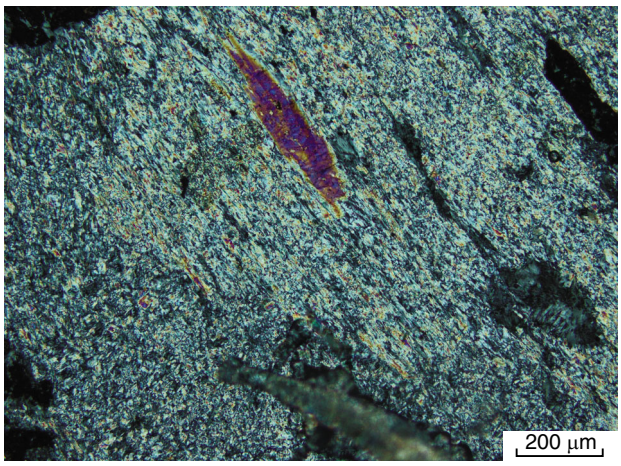

Figure 57. **Flake of relatively coarse-grained mica (possibly magnesium and iron-bearing paragonite) with abundant fine-grained mica (GSWA 208070B from 450.0 m in YD09-03); crossed polars**

Dark micas scarcely show in the summary plots although they show in plots of the downhole distribution of dark micas for SWIR and TIR data. In YD09-01, the SWIR plot (Fig. 55d) shows phlogopite as the dominant dark mica whereas the TIR plot (Fig. 55e) shows biotite as the most abundant dark mica directly below the upper mineralized horizon at Just Desserts, with phlogopite becoming more abundant downhole. Also, the TIR plot suggests the presence of the brittle mica, stilpnomelane. One example of a dark mica intergrown with anthophyllite (Fig. 46) was shown by SEM analysis as biotite (analyses 9 and 10, Table 7). TSG interpreted the SWIR spectra at this point as aspectral, although the spectra showed an absorption feature at 2250 nm consistent with biotite. Unfortunately chlorite has an absorption feature that overlaps with that of biotite at this wavelength. TSG for TIR showed paragonite as the only mica where this sample was taken, indicating that caution is needed for interpreting TSG results for mica, as indicated by Green et al. (2012).

Stilpnomelane was identified optically and by semiquantitative SEM analysis at one site where the TSG TIR user data suggested it was present, although the system data indicated muscovite at this point. The stilpnomelane was in a veinlet associated with sulfides and magnetite, talc, and ?hisingerite in the matrix of mineralized chert breccia at Just Desserts (Fig. 58).

?Hisingerite

A yellow-brown isotropic mineral is associated with talc, stilpnomelane, and sulfides as a cavity filling in mineralized chert breccias at Just Desserts (Fig. 58). Semiquantitative SEM analyses indicated that it consisted predominantly of iron and silica with minor calcium and magnesium. This mineral is considered most likely the hydrated iron silicate, hisingerite. It may have formed by reaction of iron carbonate and silica with sulfuric acid formed by breakdown of the sulfides, as suggested by Simpson (1920) for the Edna May mine at Westonia. This mineral is not in the HyLogger library and therefore its distribution downhole could not be assessed. However, it was only seen in thin section in mineralized chert breccia from Just Desserts.

Apatite

Apatite formed as both euhedral, zoned crystals associated with mineralization (Fig. 33b) and irregular grains in silicate-facies BIF. A plot of apatite weights from TIR showed reasonable correlation of apatite with mineralization in YD09-03 with a suggestion of some apatite also in the volcanic rocks beneath mineralization (Appendix 5i). The plot of apatite weights for YD09-01 (Appendix 4i) showed only sporadic distribution of apatite and none where some was observed and verified by semiquantitative SEM analysis at 111.1 m in this drillhole; however, most of the mineralized zones are missing from this drillhole. In YRC09-01D, the greatest concentration of apatite appeared in altered basalt beneath the C Zone mineralization (Appendix 7i). There were no significant concentrations of apatite recorded for YRC10-13D (Appendix 6i) or YD10-01 (Appendix 8i).

Tourmaline

Tourmaline fringes pyrite in altered basalt beneath the C Zone mineralization in YRC09-01D (Fig. 56) and infilling a vein in very altered andesitic hyaloclastite 150 m above mineralization in YD09-03 (Fig. 59). Downhole distribution of tourmaline according to the SWIR and TIR spectra was erratic. Whereas SWIR is more accurate than TIR for tourmaline identification (Hancock et al., 2013), tourmaline shares absorption features with quartz, muscovite, and biotite in SWIR; thus, false positives and negatives can be obtained.

Hypersthene (orthopyroxene)

Large plates (up to 5 mm) of a partially altered mineral with green to pink pleochroism were associated with cordierite in highly altered rock 18 m beneath the C Zone mineralization at 272.0 m in YRC09-01D (Fig. 60). This mineral looked like the orthopyroxene hypersthene, although its extinction angle was at a slight angle to the cleavage. The identity of the hypersthene was confirmed by SEM analysis (17.15% MgO, 30.2% FeO, 50.1% SiO_2, 2.5% Al_2O_3, 0.0% Na_2O, 0.0% CaO). Originally it was thought that this rock must be a highly altered hypersthene gabbro. However, spectral matching

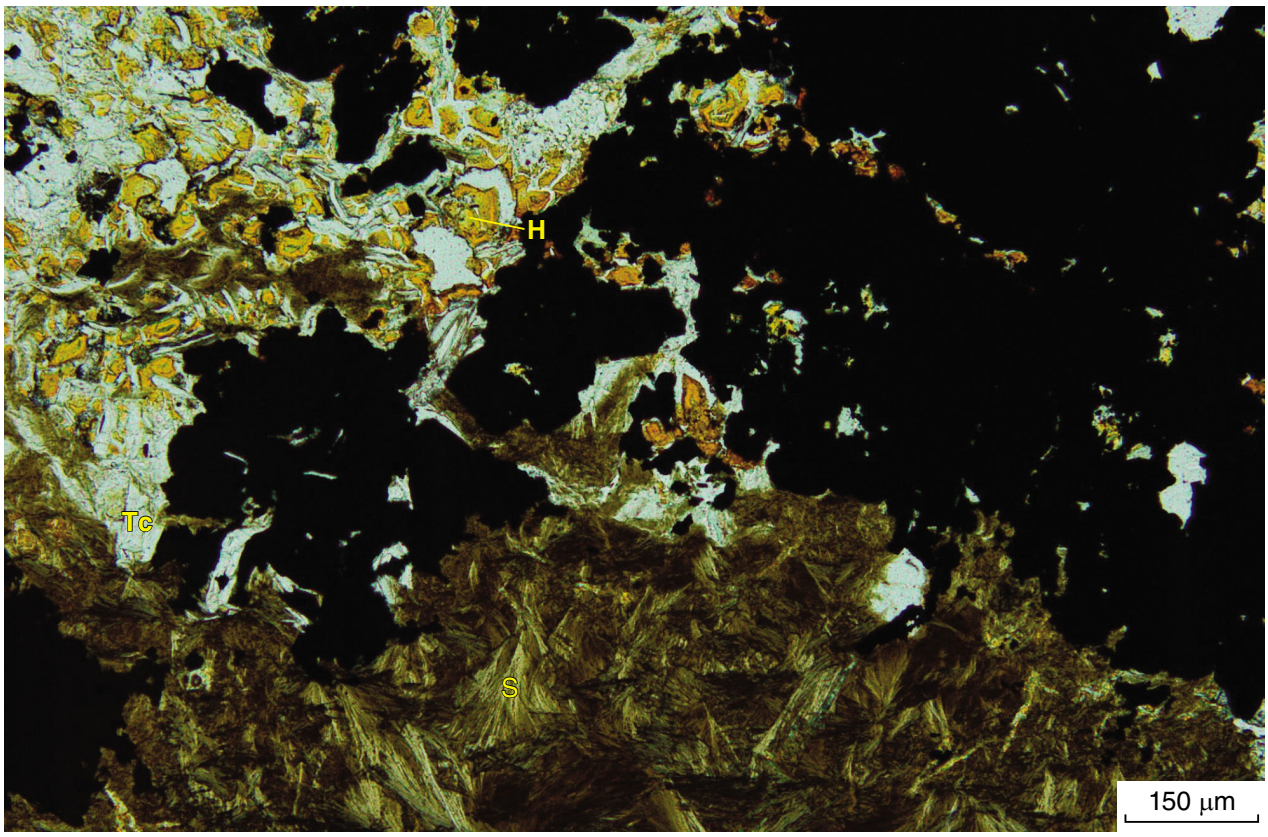

Figure 58. **Veinlet of stilpnomelane (S) associated with sulfides and magnetite (opaque), talc (Tc) and ?hisingerite (H) in matrix of mineralized chert breccia at Just Desserts (GSWA 204945 from 121.3 m in YD09-01); plane-polarized light**

on the TIR data for hypersthene suggested much higher concentrations of hypersthene further downhole at 288.5 m (Fig. 61). Thin sections from this material showed that the hypersthene occurred along the edge of a carbonate veinlet and in the matrix in association with cordierite, anthophyllite, and cummingtonite: the hypersthene appeared to be a metasomatic mineral, possibly replacing cordierite. The presence of amygdales filled with quartz and anthophyllite indicated that this hypersthene-bearing rock was volcanic (Fig. 62). Every gradation was found between this highly altered hypersthene-bearing rock and relatively unaltered basalt (Fig. 3).

Orthopyroxene also formed in highly altered andesitic hyaloclastite 260 m above mineralization in YD09-03, where remnants in optical continuity suggest the original plates were up to 5 mm across (Fig. 63), similar to those in Figure 60. Although a TIR match for hypersthene identified the hypersthene at this location, many false positives were given in rocks containing hornblende or actinolite, including the gabbro. Thus, care is needed when interpreting the TIR data, which can be used only as a guide to where hypersthene might be found. Petrography is required for confirmation.

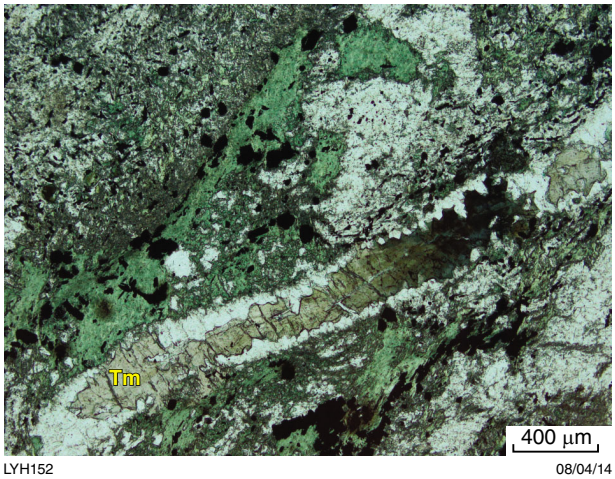

Figure 59. **Pale pink to dark blue pleochroic tourmaline (Tm) in veinlet in altered andesitic hyaloclastite (GSWA 208038 from 129.0 m in YD09-03)**

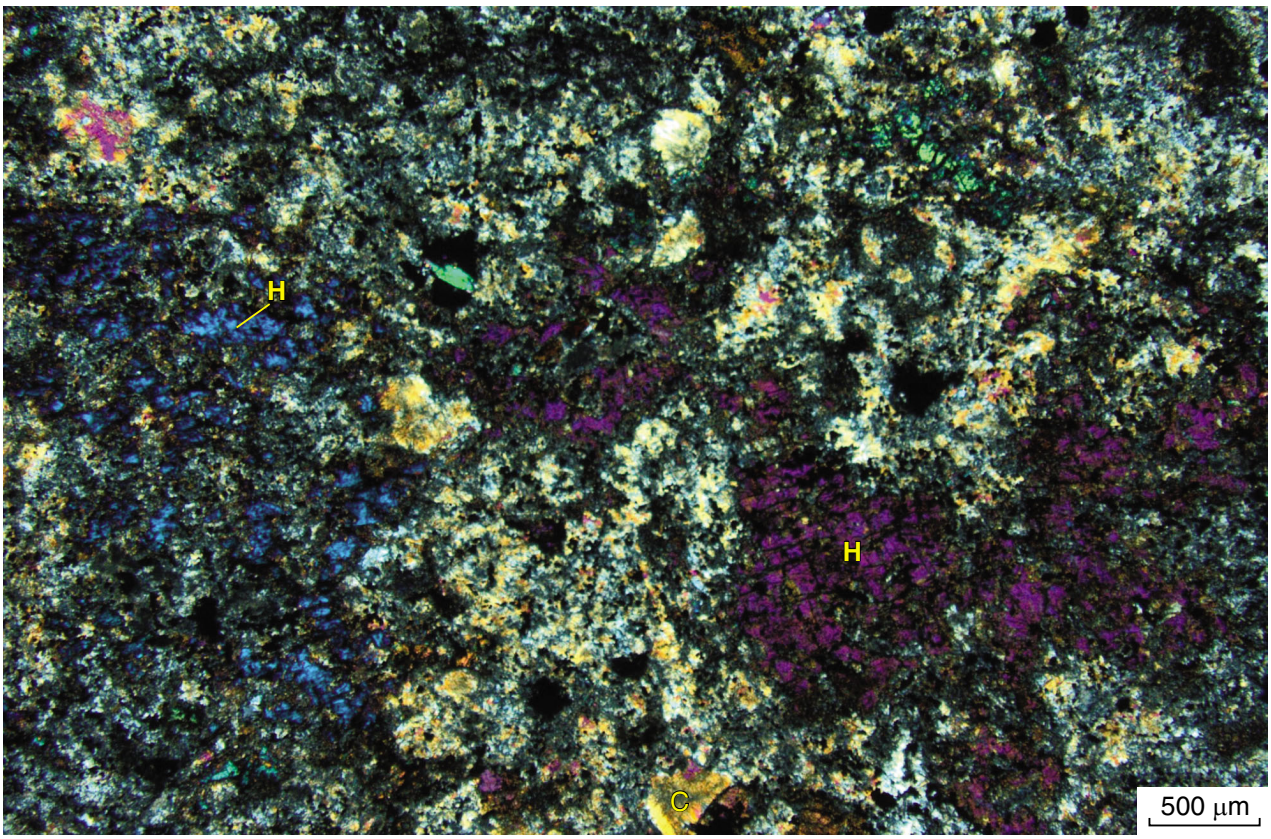

Figure 60. **Plates of hypersthene (H) associated with cordierite (C) in highly altered basalt 18 m beneath the C Zone mineralization (GSWA 208135 from 272 m in YRC09-01D); crossed polars, and note the section is thick so birefringence appears higher than normal.**

Geochemistry

The host rocks of VMS deposits are always altered and therefore major element geochemistry cannot be used for classification or determination of the tectonic environment. However, many trace elements including REE and high field strength elements (HFSE) are typically immobile during alteration and metamorphism up to moderate grades. Provided accurate analyses are made, trace elements can be used to classify rocks (Winchester and Floyd, 1977; Pearce, 1996) and to discriminate rocks formed in different geological settings (Pearce and Cann, 1971, 1973; Wood et al., 1979; Wood, 1980; Sun and McDonough, 1989; Rollinson, 1993; Pearce, 1996, 2008; Swinden, 1996; Kerrich and Wyman, 1997).

Selected samples of least altered and highly altered volcanic rocks and intrusive rocks were crushed and milled at GSWA's Carlisle laboratory using a tungsten carbon mill. Morris (2007) showed that there was negligible contamination of Bunbury Basalt samples milled in this way for the REE and HFSE of interest. Powdered aliquots were then submitted to ALS Laboratories for analysis of whole-rock geochemistry by XRF, and REE, Nb, Ta, Th, Y, Sc, V, Cr, and Zr by inductively coupled plasma–mass spectrometry (ICP-MS) following a lithium metaborate fusion and acid digest. The lithium metaborate fusion was used to address problems associated with incomplete dissolution of refractory elements (Watkins and Nolan, 1990; Jenner, 1996; Kerrich and Said, 2011). Duplicates and standards submitted with the samples showed that there was reasonable accuracy and precision for the elements of interest with blanks containing less than three times the lower detection limit except for sporadic higher values for La (up to 6 ppm) and Ta (up to 0.1 ppm). Results are presented in Appendix 2.

As indicated in the Geology section, the lower volcanics plot as basalt on the discrimination diagram of Pearce (1996) whereas the upper volcanics at Just Desserts and C Zone plot in the field of andesite – basaltic andesite. A volcanic rock from near the Augustus prospect plotted as basalt although it is compositionally distinct from the basalts of the lower volcanics (Fig. 6).

Primitive mantle-normalized plots of the immobile elements ordered by trace element incompatibility for the different rock types at Yuinmery are given in Figure 64.

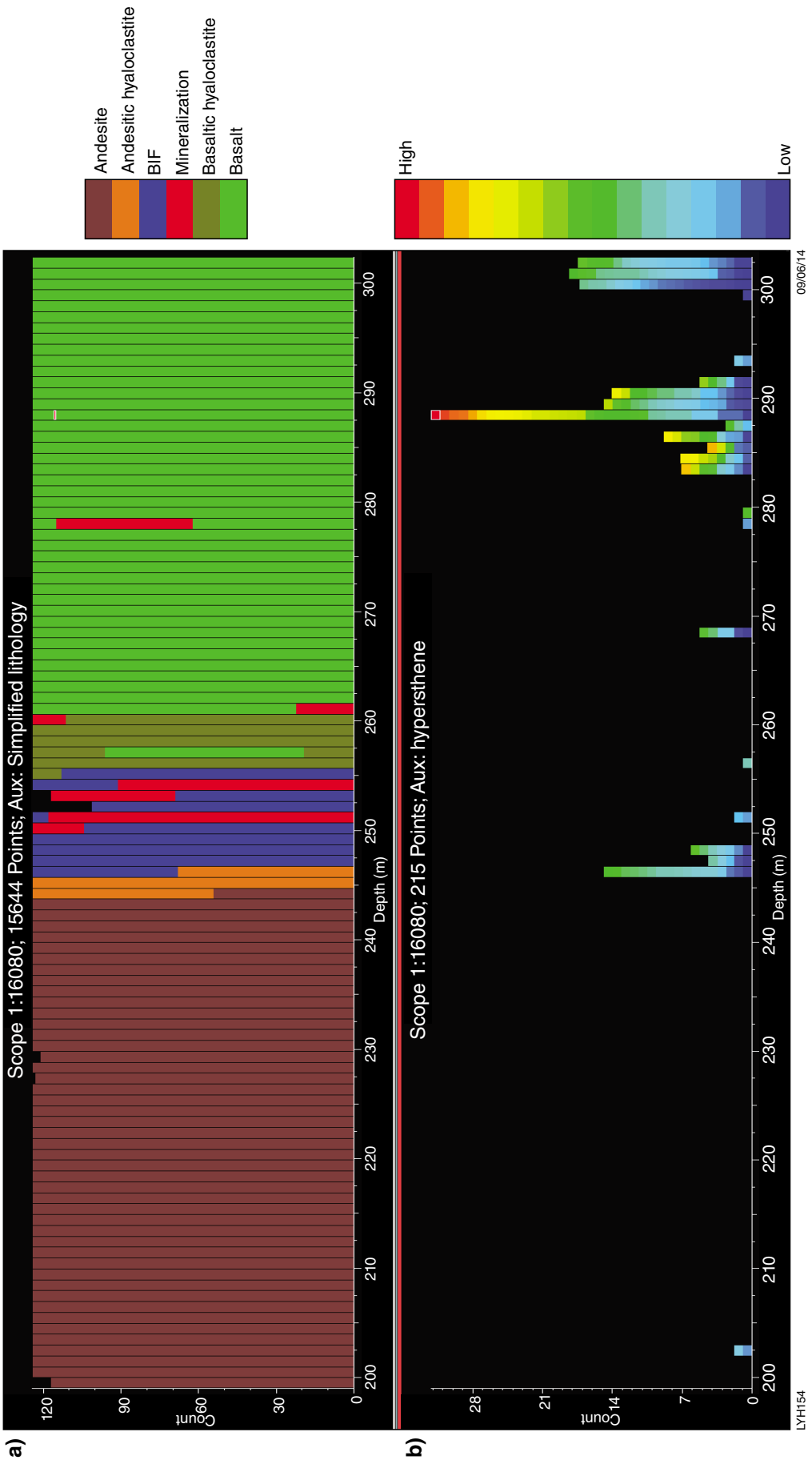

Figure 61. Spectral match of thermal infrared (TIR) data for hypersthene from Arizona State University (ASU) and Johns Hopkins University (JHU) TIR libraries (colours are relative indications of certainty: red, high; dark blue, low) vs lithology for YRC09-01D: a) lithology; b) hypersthene

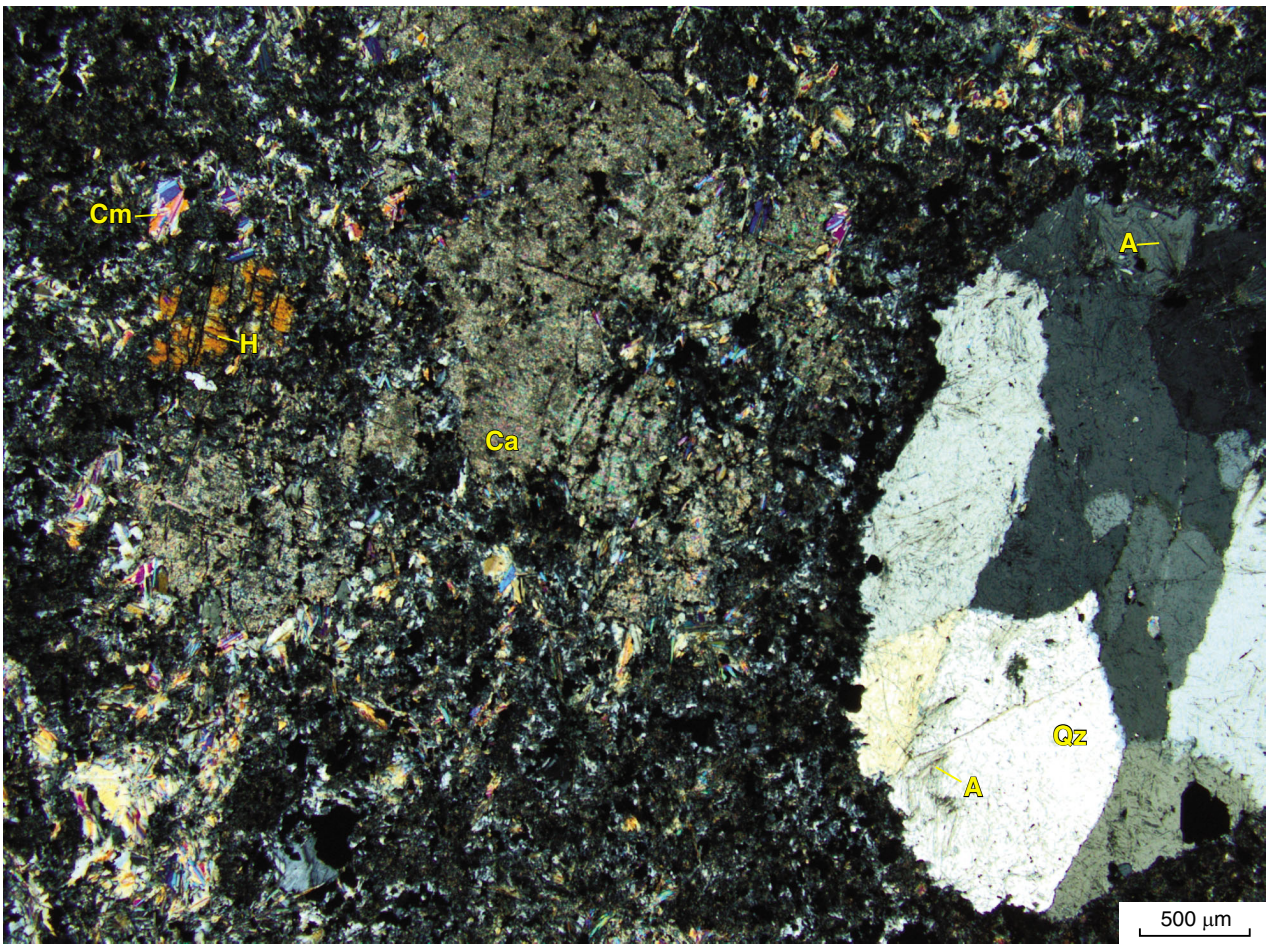

Figure 62. Altered amygdaloidal basalt containing hypersthene (H) associated with cummingtonite (Cm) and carbonate (Ca); note large amygdale filled with quartz (Qz) and acicular anthophyllite (A) at lower right (GSWA 206869 from 288.5 m in YRC09-01D); crossed polars

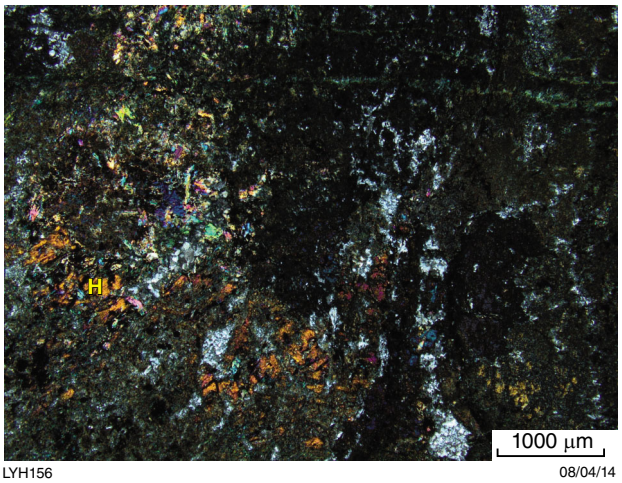

Figure 63. Remnants of large hypersthene plates (H) in highly altered andesitic hyaloclastite (GSWA 208037 from 123.0 m in YD09-03); crossed polars

Figure 64. (facing) Primitive mantle-normalized plots of immobile elements ordered by trace element incompatibility for the different rock types at Yuinmery (normalization values and order of incompatibility from Sun and McDonough, 1989): a) lower volcanics from Just Desserts and C Zone areas; b) upper volcanics from Just Desserts and C Zone areas; c) basalt of upper volcanics from Augustus area; d) ?rhyolite remnant in gabbro from Augustus area; e) intrusive andesite from Just Desserts area; f) pyroxenite from Augustus area; g) gabbros from Just Desserts – Trajan and Augustus areas; h) granophyre from Just Desserts – Trajan area; i) dolerite from Augustus area

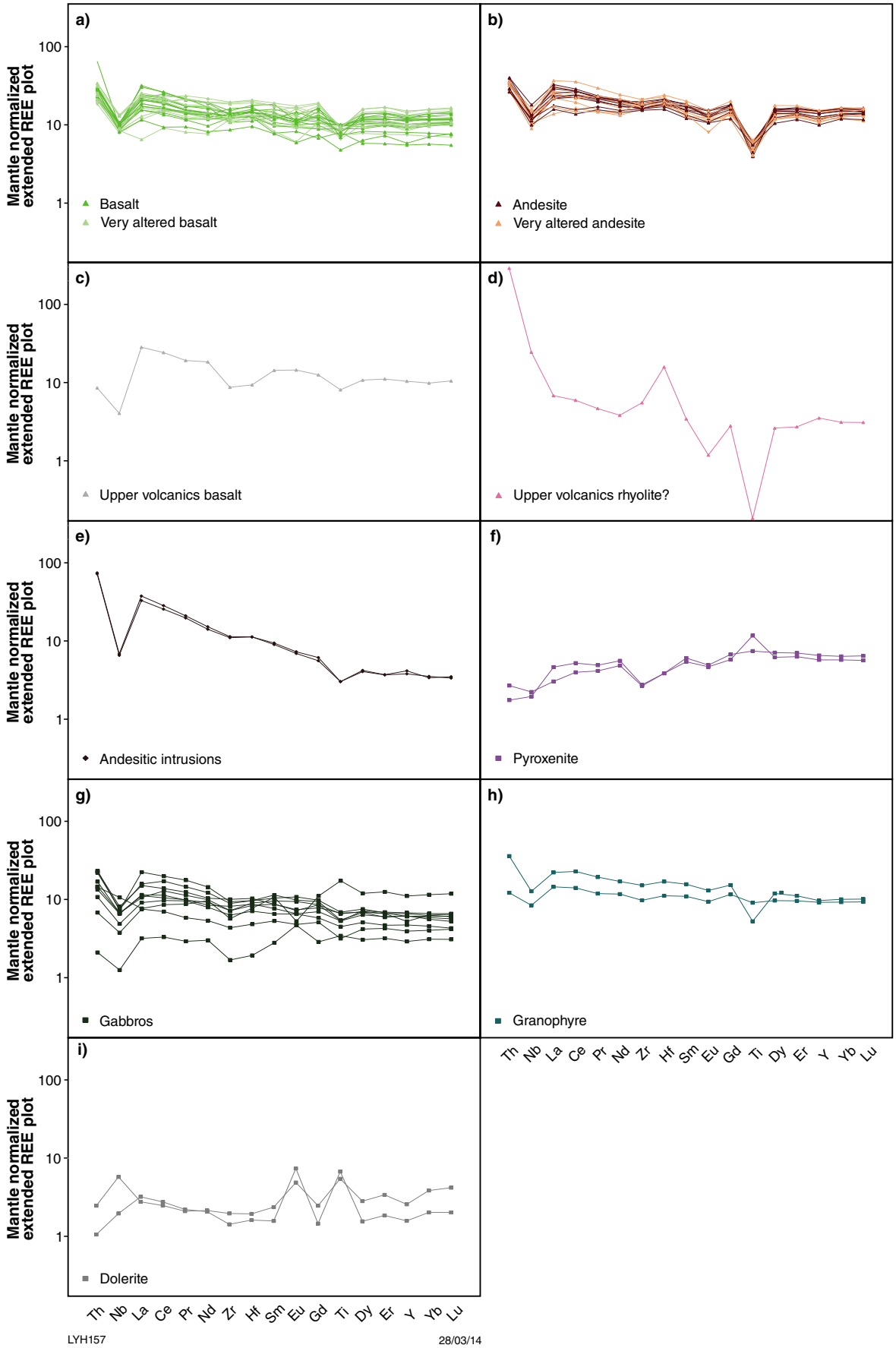
a)
b)
c)
d)
e)
f)
g)
h)
i)
Mantle normalized extended REE plot
100
10
1
Basalt
Very altered basalt
Andesite
Very altered andesite
Upper volcanics basalt
Upper volcanics rhyolite?
Andesitic intrusions
Pyroxenite
Gabbros
Granophyre
Dolerite
Th Nb La Ce Pr Nd Zr Hf Sm Eu Gd Ti Dy Er Y Yb Lu
LYH157
28/03/14

The normalization values and order of incompatibility are from Sun and McDonough (1989). Because Nb and Ta have similar incompatibilities, and the Nb values in the blanks were less than the lower level of detection and values in the rocks were higher than Ta (and thus less likely affected by contamination), Nb was used in these plots. For comparison, primitive mantle-normalized plots for non-arc, arc, and transitional mafic rocks are given in Figure 65.

The basalts and basaltic hyaloclastites from the lower volcanics beneath Just Desserts and the C Zone (Fig. 64a) are enriched in REE and HFSE relative to the primitive mantle, although Nb is depleted relative to Th, and Ti also shows a negative anomaly. The heavy REE have a flat pattern whereas the light REE show a slight enrichment trend. The patterns for highly altered basalts are similar to the least altered basalt, indicating that alteration has not greatly affected the REE and HFSE signatures. The primitive mantle-normalized plots for the lower volcanics resemble those for typical calc-alkaline basalts (Fig. 65b). The andesites from the upper volcanics at Just Desserts and C Zone (Fig. 64b) have fairly similar patterns to the basalts of the lower volcanics, although the light REE are slightly more enriched and the negative Ti anomaly is more pronounced. There is very little difference between the patterns for highly altered andesite and less-altered andesite. A basalt sample from the upper volcanic rocks near the Augustus prospect in YD10-01 has a very different pattern on the mantle-normalized plot (Fig. 64c), with much lower Th and very weak negative Nb and Ti anomalies, than the basalts of the lower volcanics and andesites of the upper volcanics.

The ?rhyolite from YD10-01 has an erratic mantle-normalized extended REE plot with intense enrichment of Th and strong depletion of Ti. There is also a negative Eu anomaly and a positive Hf anomaly, and Nb is depleted relative to Th but enriched relative to La (Fig 64d). Given this rhyolite is a remnant within a gabbro, it is not certain how meaningful these values are.

Two samples from separate andesitic intrusions intersected by YD09-01 at Just Desserts give almost identical mantle-normalized extended REE patterns (Fig. 64e). These intrusive andesites resemble the basalts of the lower volcanics and andesites of the upper volcanics with negative Nb and Ti anomalies, although they have a much stronger trend of enrichment though the middle and light REE than the upper and lower volcanics. This pattern still most closely resembles that of calc-alkaline basalts (Fig. 65b).

Mantle-normalized plots of the mafic–ultramafic intrusions are also given for comparison. The pyroxenites from YD10-01 have a fairly flat REE pattern, although there is a slight trend to depletion in the light REE, and Nb, Th, and Zr are relatively depleted, whereas Ti is flat to slightly enriched (Fig. 64f). The pattern is intermediate between island-arc tholeiite and back-arc basin basalt. The gabbros from the Just Desserts – Trajan area (Fig. 64g) and the granophyre from this area (Fig. 64h) are somewhat similar to the basalts of the lower volcanics from this area

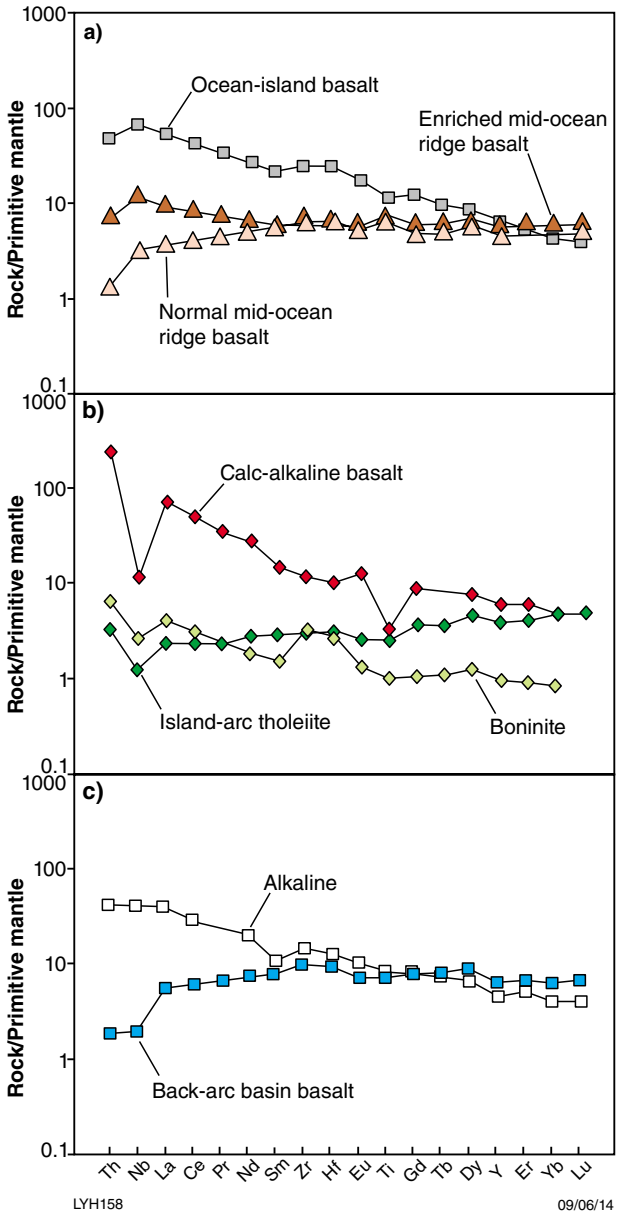

Figure 65. Primitive mantle-normalized plots of immobile elements ordered by trace element incompatibility for mafic rocks: a) non-arc rocks; b) arc rocks; c) transitional rocks; modified from Piercey (2011) with normalization values from Sun and McDonough (1989)

because they show Nb depletion, a slight trend to light REE enrichment, and much less depletion in Ti. The two gabbros from YD10-01 near the Augustus prospect differ both from each other and from the gabbros from the Just Desserts – Trajan area. One sample (GWSA 208095), taken from gabbro in close proximity to the pyroxenite, has a pattern fairly similar to the pyroxenite with slight depletions in Th, Nb, and Zr and very slight enrichment in Ti; it differs in having a slight positive Eu anomaly.

A sample (GWSA 208093) taken further downhole has a positive Ti anomaly, negative Eu anomaly, and no Nb anomaly. Fine-grained dolerites with zoned feldspar crystals from YD10-01 have weak negative Th anomalies and fairly flat REE profiles (Fig. 64i) similar to mid-ocean ridge basalts (Fig. 65a) apart from their positive Eu and Ti anomalies.

Wood et al. (1979) and Wood (1980) showed that the Th–Hf–Ta diagram could discriminate destructive plate-margin lavas from those erupted in other settings and further to discriminate primitive arc tholeiites from calc-alkaline rocks. The plot is applicable for both mafic and felsic rocks. The basalts from the lower volcanics and the andesites from the upper volcanics all plot within the calc-alkaline basalt field on the Th–Hf–Ta diagram, as does the rhyolite from YD10-01 (Fig. 66). The basalt from the upper volcanics in YD10-01 plots just outside the island-arc tholeiite field. Given that the Ta values are very low, it is acceptable to replace the Hf and Ta on this plot with Zr and Nb, respectively (Wood et al., 1979). On the Th–Zr–Nb diagram, the basalt from YD10-01 plots within the primitive arc tholeiite field and the basalts from the lower volcanics and the andesites from the upper volcanics plot within the calc-alkaline basalt field, as before (Fig. 67).

Pearce et al. (2005) and Pearce (2008) demonstrated that normal mid-ocean ridge basalt (N-MORB), enriched mid-ocean ridge basalt (E-MORB), and ocean island basalt (OIB) show a distinct array on a plot of Th/Yb vs Nb/Yb (or Th/Yb vs Ta/Yb) and that island-arc volcanic rocks plot above this array. All of the Yuinmery basalts and andesites plot above the MORB–OIB array on the Th/Yb vs Nb/Yb diagram (Fig. 68). These results are discussed further in the next section.

Discussion

Tectonic setting and environment of formation

The mineralized zone at Just Desserts – Trajan can be traced along strike to the C Zone. It is marked not only by the presence of BIF and chert horizons but also by a change in composition of the volcanic rocks from basaltic to andesitic. The presence of basalt beneath the mineralization and BIF in YD10-01 in the Augustus prospect area indicates that there is another change in the composition of the volcanic rocks either along strike or stratigraphically above the andesite. The Western Mining Corporation diamond drillholes through the B Zone might provide information on where the contact between the basalt and the andesite is; unfortunately this drillcore could not be located. The presence of remanent rhyolite in the gabbro in YD10-01 suggests that rhyolite was present higher up in the sequence, above the mineralization at Augustus, although it has since been stoped out by the gabbro and pyroxenite. The presence of BIF, silicate-facies iron-formation, and chert in the Just Desserts – Trajan – C Zone, and at A Zone and in the B Zone and Augustus area, is evidence of periods of quiescence in volcanic activity and also indicates a subaqueous environment. Abundant hyaloclastites throughout the volcanic succession (Figs 5 and 15) also indicate a subaqueous eruption environment.

Franklin et al. (2005) classified VMS deposits into five main lithostratigraphic types using sequence boundaries defined by major time–stratigraphic breaks, faults or intrusions:

1. Bimodal-mafic — formed in incipient-rifted suprasubduction oceanic arcs, typified by flows and less than 25% felsic strata (e.g. Noranda, Urals)
2. Mafic — formed in primitive oceanic back-arcs typified by ophiolite sequences with less than 10% sediment (e.g. Cyprus, Oman)
3. Pelite-mafic — formed in mature oceanic back-arcs, typified by subequal amounts of pelite and basalt (e.g. Windy Craggy, Besshi)
4. Bimodal-felsic — formed in incipient-rifted suprasubduction epicontinental arcs, typified by 35–75% felsic volcanic strata (e.g. Skellefte, Hercules-Rosebery)
5. Siliciclastic-felsic settings — (e.g. Iberia, Bathurst).

On the basis of the petrology and trace element geochemistry, the mineralization in the Just Desserts – Trajan – C Zone area most closely fits the bimodal-mafic model of Franklin et al. (2005).

On the Th–Hf–Ta and Th–Zr–Nb discrimination diagrams of Wood et al. (1979) and Wood (1980), the basaltic rocks underlying mineralization in the Just Desserts – Trajan area and C Zone, and the andesitic rocks overlying mineralization in the same area, plot in the calc-alkaline arc volcanic field whereas the basalt in the Augustus prospect area plots within or close to the island-arc tholeiite field (Figs 66, 67). All of these volcanic rocks also plot above the MORB–OIB array of Pearce (2008) on a Th/Yb vs Nb/Yb plot (Fig. 68). In the case of the modern-day Mariana Arc–basin system, the Mariana Arc volcanic rocks plot well above the MORB–OIB array, the Mariana Trough (back-arc basin) volcanic rocks plot just above and within the MORB–OIB array, and the arc-rift volcanic rocks plot in between (Pearce et al., 2005; Pearce 2008). The Yuinmery samples fall within the field of the Mariana Arc-rift volcanic rocks (Fig. 68). Note that Th/Nb is a proxy for crustal input and increased values can be due to subduction or crustal contamination (Pearce, 2008). Continental flood basalts also plot above the array, although as discussed below, the Yuinmery volcanic rocks are subaqueous so a subcontinental plume origin can be ruled out. As demonstrated by Pearce (2008), intra-oceanic plumes that evolved from subcontinental plumes such as the Kerguelen lavas may plot above the MORB–OIB array. However, unlike the Yuinmery volcanic rocks, they are not displaced very far above the array.

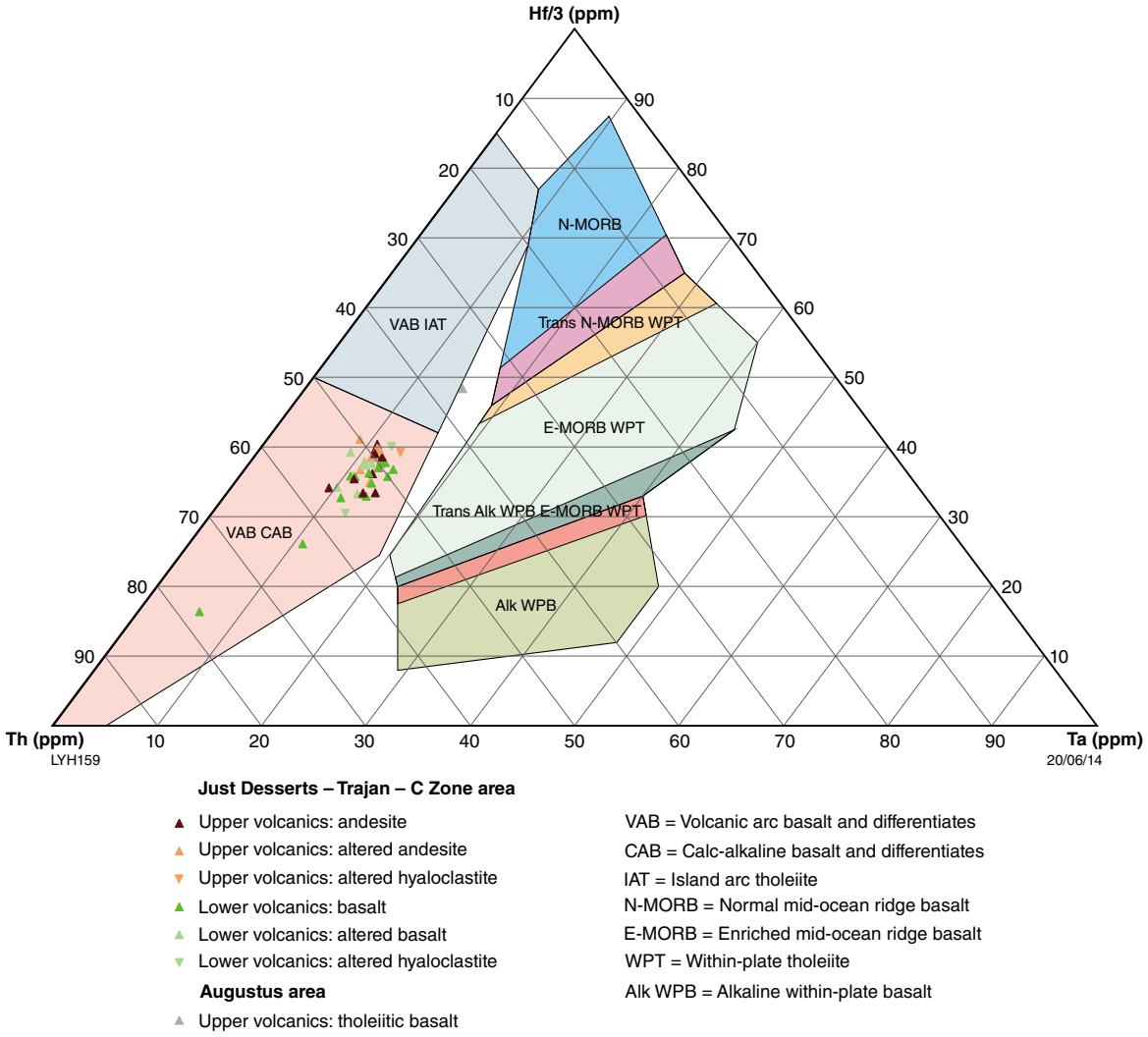

Figure 66. Th–Hf–Ta plot of Yuinmery volcanic rocks relative to tectonic fields of Wood (1980)

There is considerable controversy about whether plate tectonics comparable to that in the modern environment took place during the Archean (Stern, 2005; Bédard, 2010; Stevens et al., 2010; Van Kranendonk, 2010; Barnes et al., 2012). Barnes et al. (2012) pointed out that calc-alkaline volcanic rocks are not exclusive to arc settings and proposed that the andesites in the Kurnalpi Terrane, which had previously been interpreted as forming in an arc setting (Barley et al., 2008), could alternatively have been formed by assimilation and fractional crystallization of plume basalts as part of a large igneous province. This theory is based largely on the relatively high Cr concentrations in the andesites in the Kurnalpi Terrane, whereas arc volcanic rocks have low Cr and Ni concentrations. This argument cannot be used against an arc origin for the Yuinmery volcanic rocks as they have very low Cr and Ni concentrations (maximum 70 ppm Cr and 40 ppm Ni in the basalts and 30 ppm Cr and 6 ppm Ni in the andesites; Appendix 2). Van Kranendonk et al. (2013) suggested that andesites from the Greensleeves Formation of the Polelle Group in the Cue–Meekatharra area to the north of Yuinmery are also plume related, and concluded that the entire Yilgarn Craton may have been contiguous in 2820–2790 Ma during onset of magmatic events related to a deep mantle plume, and later split into narrow crustal ribbons through rifting, although Van Kranendonk et al. (2013) did not rule out an arc accretion model. However, Wyman and Kerrich (2012) identified boninite in a sample from the Polelle Group of the Meekatharra Formation and concluded that its presence provided clear evidence of subduction tectonics during the evolution of the 2825–2700 Ma evolution of the Youanmi Terrane.

Although many VMS deposits are hosted in submarine calderas associated with plumes beneath accreted volcanic arcs in the Archean Abitibi greenstone belt in Canada (Mueller et al., 2009), there are no known VMS deposits associated with plume-related continental basalts and associated rocks of large igneous provinces. VMS deposits

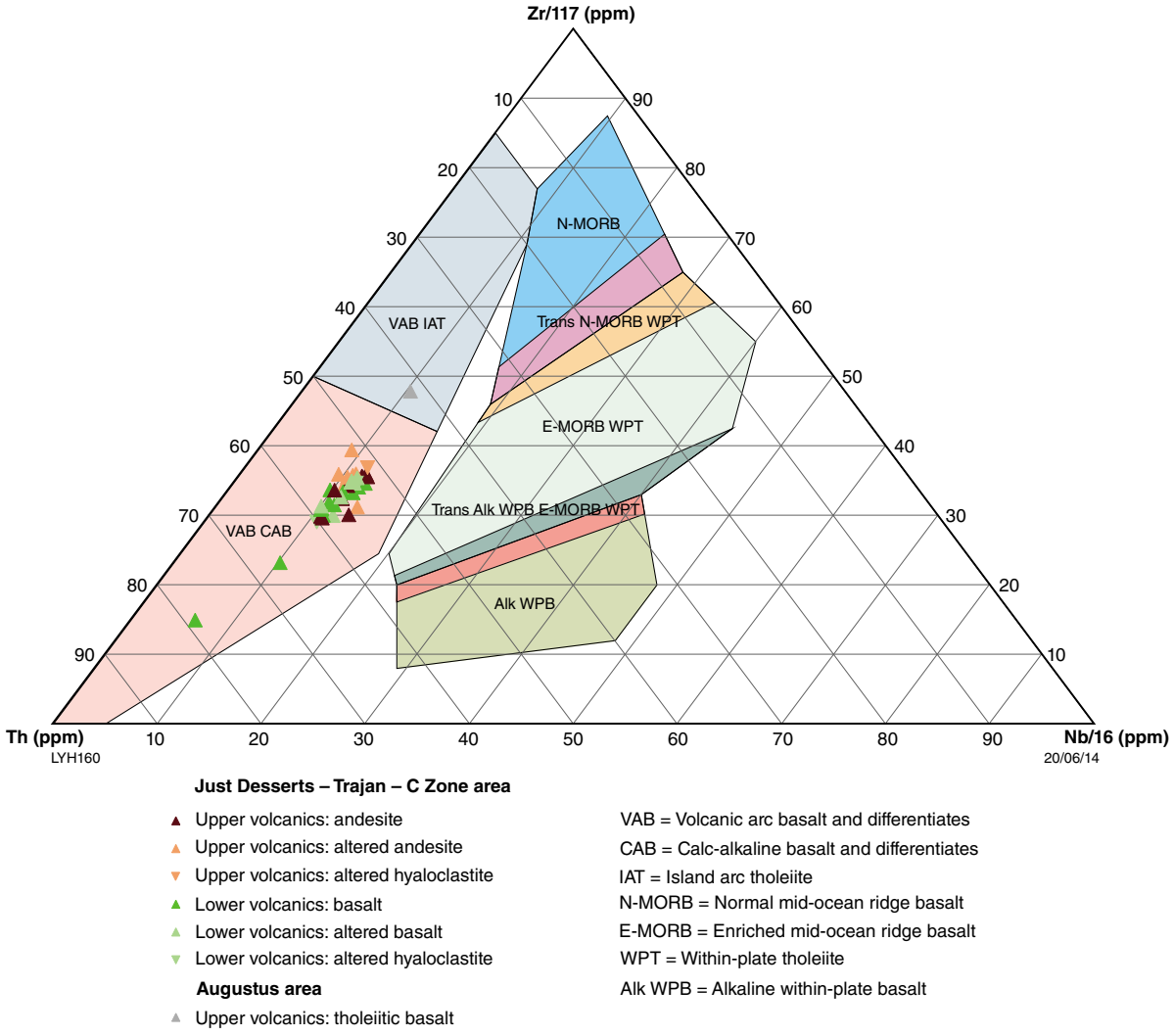

Figure 67. Th–Zr–Nb plot of Yuinmery volcanic rocks relative to tectonic fields of Wood (1980)

are formed in submarine environments because heat and fluid flow are essential for their formation (Barrie, 1999).

Currently, black smokers (hydrothermal vents) are found at mid-ocean ridges, in back-arc basins, and on submarine volcanic arcs. Arc-related examples where sulfide deposits are forming include the Mariana Trough, central Manus Basin, North Fiji Basin, and Lau Basin (Hannington et al., 2005).

The mineralization forming the matrix to chemical sedimentary breccias in the Just Desserts – Trajan – C Zone (Figs 11, 13, 26 and 30) is interpreted to have formed on the sea floor from hydrothermal vents during a period of relative quiescence in volcanic activity. The soft-sediment deformation of some of the fragments before incorporation in the breccia (Fig. 13) suggests that the chemical sediments from which the fragments formed were in a gel-like state at the time of formation of the breccia. A possible explanation is that sediments slumped down the sides of a hydrothermal vent or sulfide mound. According to Cas (1992), VMS deposits on the sea floor must have formed at depths of at least 500 m, as this is the minimum depth to provide sufficient pressure to prevent boiling and loss of sulfides in the substrate. Gibson et al. (1999) stated that VMS deposits have been found in water shallower than 300 m, although in the examples cited from the Skellefte district in Sweden, there is a range in styles from deep-water sea-floor ores, to subsea-floor replacements, to shallow-water, and possibly subareal synvolcanic epithermal replacements (Allen et al., 1997).

The sulfides infilling fractures in the chemical sedimentary rocks and infilling the matrix of the hyaloclastites in other parts of the Just Desserts – Trajan – C Zone deposits may have formed as a result of ponding of the hydrothermal fluids by the overlying chert and BIF that may have acted as an impermeable barrier; alternatively they may indicate some boiling with resulting deposition in the substrate.

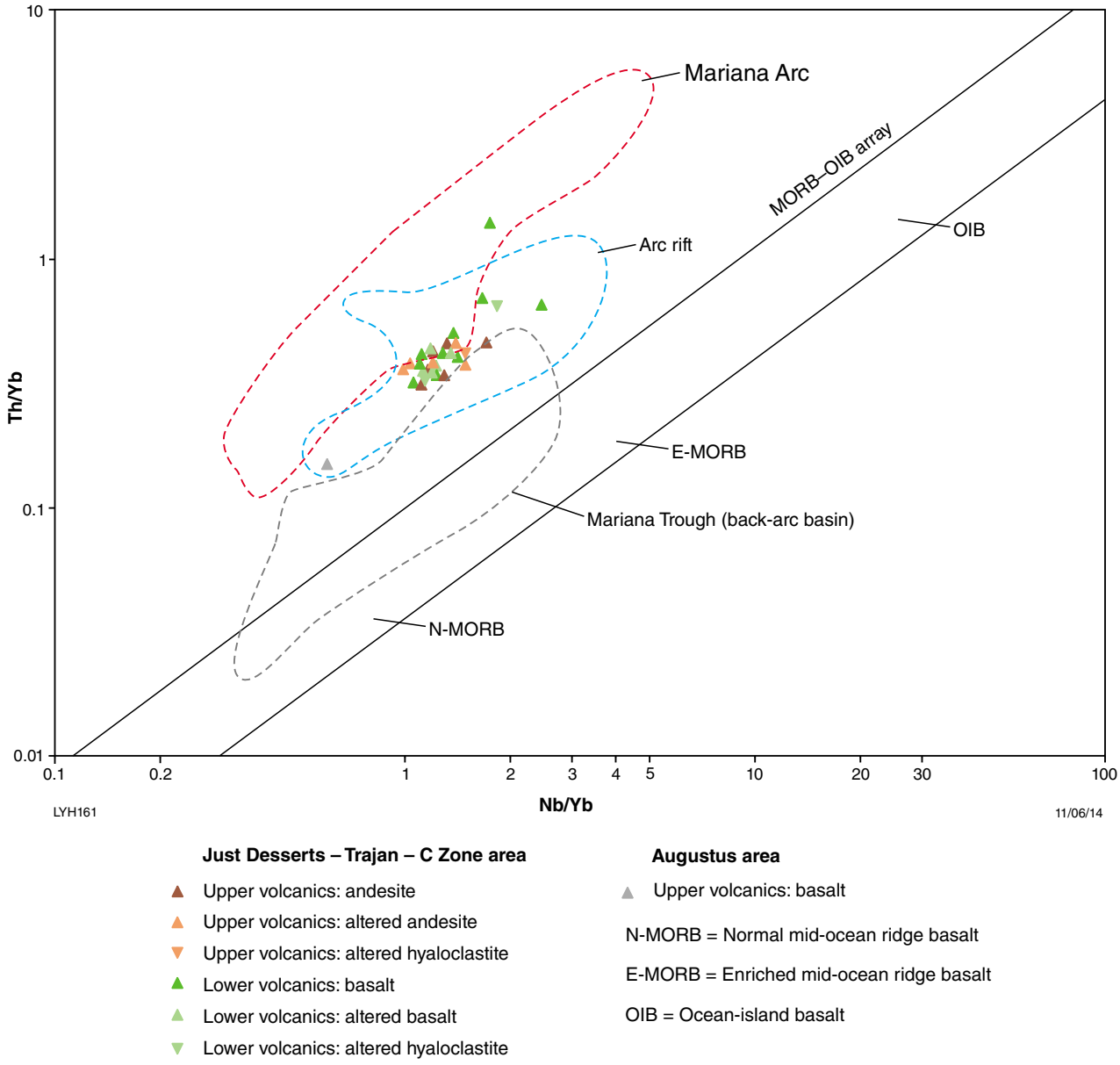

Figure 68. **Th/Yb vs Nb/Yb plot for Yuinmery volcanic rocks showing the MORB–OIB array and fields for the Mariana Arc, Mariana Arc-rift and Mariana Trough (back-arc basin) for comparison (after Pearce, 2008). The chemistry is consistent with the formation of the Yuinmery volcanic rocks in an arc-rift setting.**

Some mineralization in quartz–carbonate veins, particularly in the Augustus prospect area, may have been remobilized, possibly because of intrusion by gabbro and pyroxenite or during a later hydrothermal event. The small Marloo and Continental gold workings in quartz veins within the gabbro and pyroxenite are interpreted as the results of late-stage hydrothermal events.

Chemical sedimentary rocks or exhalites such as those associated with mineralization at Yuinmery are spatially associated with many VMS deposits. They are interpreted to have formed by precipitation of silica, iron, sulfides, and other minerals from hydrothermal vents during periods of volcanic quiescence (Sangster, 1972, 1978; Slack, 2012).

Alteration and metasomatism

Footwall alteration is a characteristic feature of VMS deposits. It occurs either as an alteration pipe which typically has an inner zone of chlorite and an outer zone of sericite or as a broad, diffuse, semiconformable chloritic and sericitic alteration zone (Sangster, 1972; Gibson and Kerr, 1993; Gibson and Galley, 2007). Some deposits such as the Brunswick No. 12 at Bathurst, Canada, also have extensive phengite and chloritic hangingwall alteration (Galley et al., 2007).

HyLogger data and petrographic studies indicate that the most abundant silicate mineral near the Just Desserts and

C Zone mineralization is talc. SEM analyses indicate that this talc is iron rich. Although talc is not typically associated with VMS mineralization, abundant talc has also been reported in association with VMS mineralization at the Archean Mattagami Lake Mine in Canada (Roberts and Rearden, 1978; Costa et al., 1983); the Paleozoic Woodlawn, Breadalbane, Mount Bulga, and Googong lead–zinc deposits in New South Wales (McLeod and Stanton, 1984); and the Devonian–Triassic Chu Chua deposit in British Columbia, Canada (Aggarwal and Nesbitt, 1984). Subordinate minnesotaite and Fe-talc is also present in the inner quartz–Fe-chlorite core of the Noranda deposits in Canada (Gibson and Galley, 2007). The talc at the Mattagami Lake Mine was interpreted by Roberts and Reardon (1978) to have formed by the transformation of chlorite to talc according to the reaction:

$$3 \text{ chlorite} + 10H_2S_{(g)} + 2.5O_2 + 11H_4SiO_4 + 5Mg^{2+} = 5 \text{ talc} + 5 \text{ pyrite} + 6Al(OH)_4^- + 19H_2O + 16H^+$$

This reaction occurred as a consequence of the discharge of large fluxes of thermal waters through the volcanic pile over a period sufficient to remove almost all the aluminium from the rocks. However, according to Costa et al. (1983) there is no evidence that talc replaced chlorite at the Mattagami Lake Mine; talc is in association with sulfides in stringers that crosscut the chloritic footwall rocks and is the main gangue mineral in the ore zone where it is associated with chlorite, stilpnomelane, amphibole, sulfides, and magnetite. Like the talc in the Yuinmery mineralization, the talc at the Mattagami Lake Mine is iron rich. Costa et al. (1983) noted that iron-rich talc was previously considered rare, although it had been reported from hydrothermal precipitates in the Guaymas Basin, Red Sea, East Pacific Rise, and Mid-Atlantic Ridge; Costa et al. (1983) concluded that the talc at the Mattagami Lake Mine was precipitated from a dynamic sea-floor brine pool. Aggarwal and Nesbitt (1984) and McLeod and Stanton (1984) also considered the talc at the Chu Chua deposit was chemically precipitated from hydrothermal vents on the sea floor. McLeod and Stanton (1984) proposed a similar origin for the talc in the Paleozoic deposits of New South Wales and noted that talc and white mica are mutually exclusive, possibly because muscovite precipitates under low pH conditions whereas precipitation of talc and phlogopite–biotite is favoured by higher pH conditions resulting from mixing of hydrothermal solutions with seawater. The talc in the iron formation at the Just Desserts and C Zone prospects is consistent with its forming on the sea floor by hydrothermal vent activity. However, there is evidence that talc replaces chlorite in the hyaloclastites between the mineralized horizons (Fig. 38). It is possible that not all of the Mg-rich hydrothermal fluids reached the sea floor. Some fluids may have ponded beneath the chemical sedimentary rocks, resulting in subsea-floor replacement of the underlying rocks by a reaction similar to that given by Roberts and Reardon (1978). At the present-day Hina Hina vent field in the Lau Basin, andesites directly below the sea floor have been altered to a silica–pyrophyllite–talc–pyrite – native sulfur – alunite assemblage by acidic volatile rich fluids. Sulfur isotopes suggest that magmatic volatiles were an important component of the hydrothermal fluids at Hina Hina (Herzig et al., 1998).

The presence of Ca-poor amphiboles in some of the chemical sedimentary rocks and altered host rocks at Yuinmery is another distinctive feature. According to Sangster (1972), cordierite–anthophyllite assemblages in the alteration zone commonly result from regional metamorphism, although they can be produced by thermal metamorphism. Trace element geochemistry (HFSE and REE; Pan and Fleet, 1995) demonstrated that cordierite–ortho-amphibole gneisses associated with VMS deposits at Manitouwadge, Canada, represented the metamorphosed equivalent of chlorite-rich rocks formed by hydrothermal alteration of basalts on the sea floor. Cordierite–anthophyllite rocks at Yuinmery have almost identical trace element geochemistry to the surrounding less-altered basalts and andesites. At the Lar deposit in Manitoba, Canada, anthophyllite and cummingtonite coexist with cordierite. Elliot-Meadows et al. (1999) interpreted the cordierite–anthophyllite–cummingtonite assemblage at Lar to have formed slightly above the pressure–temperature conditions at which anthophyllite reacts to form cordierite and cummingtonite (~3–4 kbar and 550–700°C) and the assemblage cordierite–anthophyllite is below these conditions. However, both the Manitouwadge and Lar deposits are in areas metamorphosed to upper amphibolite facies (Pan and Fleet, 1995; Elliot-Meadows et al., 1999) whereas the regional metamorphic grade at Yuinmery is lower greenschist (Stewart et al., 1983). At Yalwal in New South Wales, cordierite–anthophyllite is best developed in amygdales and in the matrix of brecciated mafic volcanic rocks, and is interpreted to have formed under low-temperature hydrothermal conditions (Vallance, 1967). The anthophyllite and cordierite in the matrix of some of the hyaloclastites at Yuinmery (Fig. 44) also may be the result of hydrothermal metasomatism; the anthophyllite forming along minute fractures in the chert infilling the matrix of the hyaloclastite (Fig. 45) could not have formed in any other way.

Calcium-poor amphiboles, including cummingtonite and Mn-rich amphiboles, and actinolite, are associated with talc in the upper part of the Mattagami Lake Mine. Costa et al. (1983) interpreted them as possibly deposited from sea-floor brine together with the talc and sulfides. In BIF from YRC10-13D, asbestiform anthophyllite is cut by later cummingtonite crystals (Fig. 43). Some of the larger grunerite crystals have grown across magnetite-rich layers, incorporating the magnetite within them; hence they post-date the initial deposition of the iron-rich laminae. However, these cummingtonite crystals are fractured and individual parts of the crystals displaced (Fig. 42). Thus, they may have formed and fractured while the BIF was still plastic. Evans and Ghiorso (1995) reported that cummingtonite forms over a wide range of conditions (400–800°C and <1–15 kbar). Maximum vent temperatures for modern-day mid-ocean ridge, back-arc basin, and back-arc spreading centres range from 220 to 380°C although temperatures up to 420°C have been recorded in higher salinity fluids (Barrie, 1999). If the venting solutions were highly saline it is thus possible that temperatures were just high enough to form cummingtonite. Another possibility is that the BIF was still plastic when it was overlain by the next lava flow and the heat of the lavas was sufficient to form the cummingtonite crystals, or alternatively,

that hydrothermal fluids heated to temperatures above 400°C by the underlying magma chamber formed the cummingtonite in the subsurface. Heat from the overlying lavas may also have been responsible for the formation of the rounded cloudy cummingtonite in silicate-facies BIF from YD09-01 (Fig. 48). Greenalite granules in the Gunflint Iron Formation of Ontario–Minnesota were replaced by grunerite (the iron end member of the grunerite–cummingtonite series) as the result of contact metamorphism by the Duluth Complex (Floran and Papike, 1978).

The presence of hypersthene in the basalt beneath the C Zone and in the andesites above the Just Desserts – Trajan mineralization (Figs 60, 62, and 63) is even more problematic to explain. The hypersthene appears a metasomatic rather than primary igneous phase because it forms large irregular plates adjacent to carbonate-filled fractures, and is associated with cordierite and cummingtonite. Wilson (1952) first reported metasomatic hypersthene, noting that hypersthene replaced augite in a rheomorphic vein in dolerite from the Kulgera Hills in central Australia. Wilson concluded that although hypersthene is normally thought of as a 'dry' mineral, it can form under 'wet' conditions. Hypersthene in iron formation from the Gunflint Formation is interpreted as the product of inversion of pigeonite that formed at temperatures of 800°C or more from contact metamorphism by the Duluth Complex (Simmons et al., 1974). However, if devolatization and vaporization of pore fluids are taken into account, the contact temperature could be more than 100°C lower than this (Floran and Papike, 1978). Although gabbro and pyroxenite intrude the volcanic rocks at Yuinmery, there is no evidence that they were responsible for the formation of the hypersthene; no hypersthene was noted in the contact zone in the logged drillcore. No mafic intrusive rocks were intersected in YD09-01D at C Zone and the hypersthene-bearing rock grades gradually into relatively unaltered basalt (Fig. 3) at depth in this drillhole, indicating that contact metamorphism could not be caused by an intrusion below the hypersthene-bearing rock, although an intrusion lateral to it and not intersected by the drillhole cannot be ruled out.

Hypersthene, cordierite, and anthophyllite exist only in isolated patches. Elsewhere, the talc alteration in the volcanic rocks grades downwards into chlorite–silica alteration more typical of the footwall alteration zone of VMS deposits that have undergone only low-grade metamorphism. Chloritic alteration is regional in extent and has affected all rock types, including the intrusive rocks that post-date the mineralization. The chlorite composition is partly controlled by the composition of the host rock, but where the host rock remains constant (e.g. in the basalts beneath the C Zone in YRC09–01D), the chlorite is more iron rich near mineralization (Appendix 7f), suggesting that this chlorite is the result of footwall alteration. The gradual increase in feldspar in the basalts downhole in YRC09-01D (Appendix 7a) also suggests that footwall alteration is largely responsible for the destruction of feldspar beneath the mineralization rather than later alteration associated with regional metamorphism.

Given the localized nature of the rocks containing cordierite–anthophyllite, and also hypersthene in places, it is possible that these minerals formed along feeder pipes through which hot hydrothermal fluids flowed. If this is the case, then the formation of these minerals in the andesite above and below the Just Desserts – Trajan mineralization could imply that there is another mineralized horizon stratigraphically higher, possibly equivalent to the B Zone.

Role of intrusions

Because the gabbros and pyroxenite intrude the andesites and basalts of the upper volcanics, they are clearly younger than the Just Desserts – Trajan – C Zone mineralization and could not be directly related to it. However, the intrusions indicate an extensive magma chamber beneath the region at the time they were emplaced. Thus, it is possible that this magma chamber was associated with a long-lived mantle plume and the volcanic rocks and associated mineralization were also related to it, with heat from the plume driving the hydrothermal system. A large gabbro, the Roquemaure Sill, intruding the Hunter mine caldera succession in the Abitibi greenstone belt of Canada was interpreted as forming during arc extension and crustal thinning (Mueller et al., 2009). This sill is stratigraphically below the Hunter mine mineralization, although other gabbros, interpreted as related to the magma chamber beneath the caldera, are present higher in the stratigraphy both above and below the mineralization. Together with the volcanic rocks, iron formation, and mineralization at the Hunter mine, these gabbros are all part of the caldera formational process interpreted as driven by an underlying mantle plume (Mueller et al., 2009).

The possibility that the pyroxenite and gabbro at Yuinmery caused the formation of cordierite, anthophyllite, cummingtonite, and hypersthene by contact metamorphism cannot be ruled out. However, it is considered more likely that the plume that resulted in the emplacement of the intrusions also drove the hydrothermal system, as discussed above.

All of the intrusions have the potential to have stoped out mineralization and remobilize it. In the Augustus prospect area, the pyroxenite and gabbro have stoped out almost the entire stratigraphic succession above the BIF, and a great amount of mineralization may have been lost. The base metal-rich quartz–carbonate veins intersected lower in YD10-01 may be mineralization that was mobilized during intrusion, although it could be related to a later hydrothermal event. The semiconformable granophyre that intrudes between the upper and middle mineralized horizons in YD09-01 at Just Desserts could be responsible for the much lower ore-grade intersections in YRC10-13D and YD09-03 as it intrudes the upper mineralized horizon.

The intrusive andesites may have been feeder pipes for the overlying andesites, although they show marked depletion in Nb and heavy REE. The intrusive andesites also have the potential to have stoped out mineralization in the Just Desserts – Trajan area. The andesitic intrusions are very

difficult to tell apart from the surrounding basalt in hand specimen although they stand out in the HyLogger plot because of abundant feldspar.

Comparison with other VMS deposits in the Murchison region

The Gossan Hill and Scuddles deposits at Golden Grove are world-class VMS deposits with pre-mine resources of 9.2 Mt grading 2.7% Zn, 2.6% Cu, 0.4 g/t Au, and 24 g/t Ag, and 10.5 Mt grading 11.7% Zn, 1.2% Cu, 0.8% Pb, 89 g/t Ag, and 1.1 g/t Au, respectively (MMG Golden Grove Pty Ltd, 2012). The stratigraphic succession at Golden Grove is dominated by felsic lava flows, volcaniclastic rocks, intrusive rocks, clastic sedimentary rocks with minor chemical sedimentary rocks, andesites, and basalts (Clifford, 1992). The Golden Grove VMS deposits were interpreted by Clifford (1992) to have formed in a rifted island-arc setting, although trace element geochemistry suggests that they were formed in an active continental margin (Kerrich and Said, 2011; Guilliamse, 2013, in prep.). Golden Grove thus fits the bimodal-felsic (incipient-rifted suprasubduction epicontinental arc) model of Franklin et al. (2005), whereas Yuinmery best fits the bimodal-mafic (incipient-rifted suprasubduction oceanic arc) model.

HyLogger data for six drillholes from Golden Grove showed chlorite and white mica as the dominant alteration minerals (Guilliamse, 2013, unpublished). Hardly any talc was detected by the HyLogger in the drillholes analysed by Guilliamse (2013), although Frater (1978) recorded zones with up to 60% talc associated with magnetite and sulfides at Gossan Hill. Ashley et al. (1988) recorded ferroan talc in strongly chloritic rock from the mineralized zone at Scuddles. It can be concluded that talc is locally present at Golden Grove, even though it is typically not the dominant alteration mineral as at Yuinmery. Amphiboles have also been reported from the Zn-rich zone and overlying chemical sedimentary rocks at Scuddles (Ashley et al., 1988), although cordierite and hypersthene have not been reported from Golden Grove.

If the volcanic rocks hosting the mineralization at Yuinmery were equivalent to the ≥2820 Ma to 2805 Ma Norie Group, then the mineralization would be considerably younger than that at Golden Grove, where sensitive high-resolution ion microprobe (SHRIMP) U–Pb zircon dating of rocks from the Gossan Hill Group gave an date of 2960–2945 Ma (Wang et al., 1998).

The 2977 ± 3 Ma Glenview base metal prospect, hosted by subaqueous felsic volcanic rocks and volcaniclastic rocks beneath a thick BIF horizon at Weld Range, is also interpreted by Guilliamse (2013, in prep.) to have formed during rifting in an active continental margin setting on the basis of trace element geochemistry. White mica and chlorite were the dominant alteration minerals identified by the HyLogger in drillcore analysed from this prospect (Guilliamse, 2013, in prep.); however, it is noteworthy that green shales interbedded with oxide-facies BIF higher in the succession contain minnesotaite, stilpnomelane, and chamosite–greenalite (Van Kranendonk et al., 2010), and thus bear some similarities to the iron formation in the Minnesota–Ontario area (Floran and Papike, 1978) and the silicate-facies BIF at Yuinmery.

The Austin VMS deposit, south of Meekatharra and north of Yuinmery, has a resource of 1.48 Mt grading 1.025% Cu, 1.39% Zn, 3.51% Ag, and 0.24 g/t Au (Silver Swan Group Limited, 2010). The deposit has been mapped within the Yaloginda Formation of the Norie Group (Van Kranendonk, 2011). Preliminary HyLogger studies on this deposit indicate that, as at Yuinmery, mineralization is closely associated with talc and amphiboles (Hassan, 2012).

Silver Lake Resources Ltd (2012) reported an inferred resource of 1.1 Mt grading 2.4% Cu, 0.5 g/t Au, and 13 g/t Ag at the Hollandaire deposit and interpret it as VMS mineralization hosted by felsite within a thick succession of mafic rocks that show chlorite and silica alteration. At the time of writing, no HyLogger data were available for this deposit.

Pincher Well is a VMS prospect southwest of Yuinmery on the western side of the Youanmi shear zone. Western Mining Corporation intersected high-grade zinc mineralization at Pincher Well in 1973 in rocks interpreted as acid to intermediate volcanic and volcaniclastic rocks and BIF (Western Mining Corporation, 1973b,c). Although the dominant alteration mineral is given as chlorite, DF Evans logged some talc in diamond drillhole MPWD12 (Western Mining Corporation, 1973c). Given the possible correlation of the host rocks at Pincher Well with those at Yuinmery, further work on this prospect is warranted.

Further west, O'Connor (1971) described several zinc-rich prospects in metabasalt and gossanous quartzite at Freddie Well on the western side of the Youanmi intrusion and interpreted them as remobilized VMS mineralization. These prospects are now known as the Manindi project and have a combined measured, indicated, and inferred resource of 1.354 Mt at 6.04% Zn, 0.25% Cu, 3.4 g/t Ag, and 0.25 g/t Au (Metals Australia Ltd, 2008). The remobilized mineralization at the Augustus prospect, which is also close to a gabbroic intrusion, may have a similar origin to the Freddie Well – Manindi mineralization. However, more work on both prospects is required to compare them adequately.

Other base metal prospects of possible VMS origin in the Murchison region include Wattagee Hill, Mount Mulcahy, Chunderloo (Yaloginda), and Dalgaranga (Ferguson, 1999). These prospects have not been investigated in detail in this report.

Vectors to mineralization

Trace elements are clearly useful for determining the original nature of altered rocks and the environment in which they formed. At Yuinmery, trace elements have shown that rocks considered by many exploration geologists as felsic volcanic rocks are calc-alkaline basalts and andesites with chemistries consistent with eruption in an oceanic rift setting; such a setting is highly favourable for VMS mineralization.

Iron formation near VMS deposits commonly has a positive Eu anomaly on a chondrite-normalized REE plot, whereas iron formation distant from mineralization or unrelated to mineralization has a flat pattern or negative Eu anomaly; this finding may be useful in exploring for VMS deposits (Gale et al., 1997). In the case of Yuinmery, two samples of oxide-facies BIF associated with mineralization showed a positive Eu anomaly whereas silicate-facies BIF showed an almost flat pattern (Fig. 69). The presence of the Eu anomaly in BIF could thus be a useful pointer to mineralization, although a negative result would not necessarily rule out VMS prospectivity, especially in silicate-facies BIF.

Gossan has traditionally been an indicator of mineralization. A sample of gossan (GSWA 204948) from Just Desserts assayed 0.11 ppm Au, 0.24 ppm Ag, 7.2 ppm As, 373 ppm Ba, 26.9 ppm Bi, 139.5 ppm Co, 4310 ppm Cu, 11.8 ppm Mo, 4.2 ppm Pb, 0.38 ppm Sb, 25.3 ppm Se, 1.1 ppm Sn, 32.8 ppm Te, 0.3 ppm W, and 511 ppm Zn. The high Bi and Te values suggest that these elements are useful pathfinders in addition to base metals and Au. The use of the electromagnetic method (EM) to detect sulfides is currently being applied in the search for extensions to mineralization under cover (Empire Resources Ltd, 2012).

Hyperspectral logging of drillcore or cuttings for talc could be used to indicate proximity to mineralization provided no ultramafic rocks were intersected; both SWIR and TIR readily identify talc. The widespread intrusion of the area by gabbro and pyroxenite makes MgOH advanced spaceborne thermal emission and reflection radiometer (ASTER) data difficult to interpret, although ASTER could be useful for finding talc alteration in areas not intruded by mafic intrusions. The 980 nm wavelength feature in SWIR could prove useful in recognizing Ca-poor amphiboles associated with mineralization and fluid pathways.

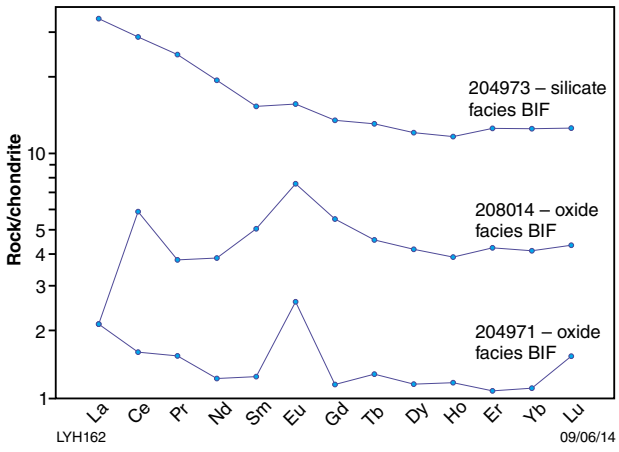

Figure 69. Chondrite-normalized REE plot for three banded iron-formation (BIF) samples from Yuinmery (GSWA 20473, 208014, 204971); normalization values from Sun and McDonough (1989)

Concluding discussion and mineralization model

The mineralization in the Just Desserts – Trajan area and C Zone is close to the contact between basaltic and andesitic rocks of calc-alkaline affinity. Both the basalt and andesite have trace element geochemistry consistent with their eruption in an intra-oceanic arc rift setting. The age of these volcanic rocks is uncertain although it is greater than the 2813 ± 5 Ma Courlbarloo Tonalite, which intrudes them. They may be equivalent to the ≥2820 to 2805 Ma Norie Group elsewhere in the Murchison, although in an arc setting there is not necessarily a 'layer-cake' stratigraphy. Horizons of oxide and silicate-facies iron-formation and chert within the uppermost part of the basalt succession indicate a period of relative quiescence before the eruption of the andesites. Textural evidence suggests that at least some of the sulfides were deposited on the sea floor by venting of hydrothermal fluids, whereas sulfides infilling the matrix of hyaloclastites and in fractures in chert may have been formed by subsea-floor replacement. Following deposition of the mineralization, there was eruption of andesites and intrusion of the mineralized horizon by intrusive andesite. The volcanic rocks were later intruded by gabbro. A pictorial representation of the sequence of events at Just Desserts is given in Figure 70.

Some mineralization is associated with recrystallized BIF at the Augustus prospect, although at this prospect, most mineralization is present in veins within the underlying basalt. Trace element geochemistry indicates that the basalt is tholeiitic, unlike the basalt beneath the Just Desserts – Trajan – C Zone mineralization, although it also has an oceanic-arc signature. There was probably rhyolite above the Augustus prospect, although it has been largely stoped out by a large mafic intrusion. Poor outcrop together with extensive faulting and the presence of mafic intrusions in the Augustus area make interpretation of geological relationships in this area difficult. However, the Augustus mineralization may correlate with the B Zone mineralization, which is stratigraphically above the Just Desserts – Trajan – C Zone horizon.

Talc dominates as the alteration mineral beneath the two upper mineralized horizons at Just Desserts and the mineralization at C Zone, whereas chlorite and silica alteration predominate elsewhere. Localized areas of cordierite + anthophyllite ± cummingtonite ± hypersthene appear metasomatic in origin and may be the pathways along which very hot hydrothermal fluids flowed. Mineral assemblages indicate that the solutions were rich in magnesium, iron, silica, and sulfur and also contained copper, zinc, lead, gold, silver, tellurium, bismuth, molybdenum, nickel, uranium, REE, boron, carbonate, and phosphorous. These solutions were probably heated by an underlying magma chamber or plume that drove the hydrothermal system, and was the source of the volcanic rocks and perhaps also the mafic intrusions if it was sufficiently long lived.

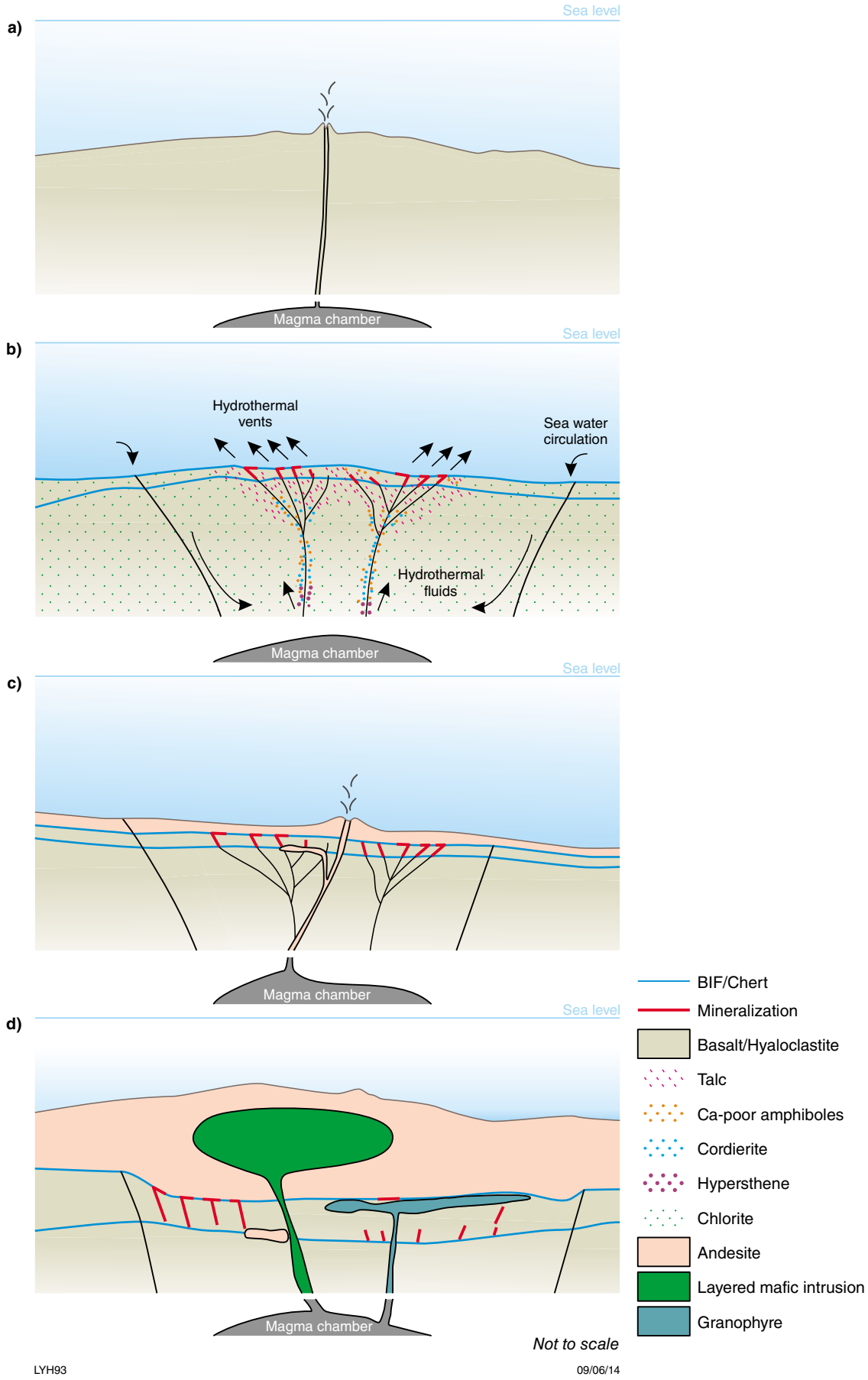

Figure 70. Model of interpreted sequence of events at Just Desserts. See text for detail

The main vector to VMS mineralization similar to that at Yuinmery on a regional scale is trace element geochemistry suggestive of formation in an arc environment. On a local scale, exploration should focus on horizons where there was a period of quiescence in volcanic activity marked by the accumulation of chemical sedimentary rocks or exhalites and a change in composition of the volcanic rocks. The presence of Eu anomalies in the chemical sedimentary rocks may indicate proximity to mineralization. The presence of gossans associated with the exhalites has been the main exploration tool in the past. In addition to base metals (which can be leached), gold, tellurium, and bismuth should be assayed. The presence of talc is characteristic of the Yuinmery mineralization and could be identified in drill cuttings or core by a portable HyLogger or HyChipper in the field. It may also be possible to detect the Ca-poor amphiboles using the 980 nm wavelength feature in the field.

Acknowledgements

Empire Resources Ltd is thanked for donating diamond drillcore to the Geological Survey of Western Australia (GSWA), providing accommodation during fieldwork, and for giving permission to publish the results of the study. The author is especially grateful to David Ross for pointing out the mineralized horizons in the field. Michael Verrall is thanked for assisting with SEM analyses, and Jon Huntington, Scott Halley, and Lena Hancock are thanked for demonstrating techniques that show variation in mineral chemistry using HyLogger data. Franco Pirajno and Stephen Wyche are thanked for peer reviewing this report.

References

Aggarwal, PK and Nesbitt, BE 1984, Geology and geochemistry of the Chu Chua massive sulfide deposit, British Columbia: Economic Geology, v. 79, p. 815–825.

Allen, RL, Weihed, P and Svenson, S 1997, Setting of Zn–Cu–Au–Ag massive sulfide deposits in the evolution and facies architecture of a 1.9 Ga marine volcanic arc, Skellefte district Sweden: Economic Geology, v. 91, p. 1022–1053.

Ashley, PM, Dudley, RJ, Lesh, RH, Marr, JM and Ryall, AW 1988, The Scuddles Cu–Zn prospect, an Archean volcanogenic massive sulfide deposit, Golden Grove District, Western Australia: Economic Geology, v. 83, no. 5, p. 918–951.

Bannister, WE 1974, Percussion and Diamond Drilling Logs for the year 1973–74, MC57/365–368, 458–476, 2726–2727, 2733–2734, 2788 & 2910–2929; Western Mining Corporation: Geological Survey of Western Australia, Statutory mineral exploration report, A5395 (unpublished).

Bannister, WE 1988, East Youanmi Project, Annual Report for the period 27/01/1987 to 26/01/1988, P57/282–285; Arboyne NL, Meekal Pty Ltd: Geological Survey of Western Australia, Statutory mineral exploration report, A23353 (unpublished).

Barley, ME, Brown, SJA, Krapež, B and Kositcin, N 2008, Physical volcanology and geochemistry of a Late Archaean volcanic arc: Kurnalpi and Gindalbie Terranes, Eastern Goldfields Superterrane, Western Australia: Precambrian Research, v. 161, p. 53–76.

Barnes, S-J, Van Kranendonk, MJ and Sonntag, I 2012, Geochemistry and tectonic setting of basalts from the Eastern Goldfields Superterrane, Yilgarn Craton: Australian Journal of Earth Sciences, v. 59, no. 5, p. 707–735.

Barrie, CT 1999, Heat and fluid flow in volcanic-associated massive sulfide-forming hydrothermal systems, *in* Volcanic-hosted massive sulfide deposits: processes and examples in modern and ancient settings *edited by* CT Barrie and MD Hannington: Society of Economic Geologists, Reviews in Economic Geology 8, p. 201–219.

Bédard, JH 2010, Falsification of the plate tectonic hypothesis for genesis of Archaean volcanic and plutonic rocks, and an outline of possible alternative mechanisms, *in* Fifth International Archean Symposium *edited by* IM Tyler and CM Knox-Robinson: Geological Survey of Western Australia; Fifth International Archean Symposium, Perth, 5 September 2010, Record 2010/8, p. 151–152.

Belford, S 1982, Yuinmery Project, Annual Report for the year ending 31st December 1982, MC57/4741–4758, 4968–4977, & MC57/5039–5041; Esso Australia Limited: Geological Survey of Western Australia, Statutory mineral exploration report, A11833 (unpublished).

Belford, S 1984, Yuinmery Project, Annual Report for the year ending 31st December 1983, E57/13; Esso Australia Ltd: Geological Survey of Western Australia, Statutory mineral exploration report, A13286 (unpublished).

Cas, RAF 1992, Submarine volcanism; eruption styles, products, and relevance to understanding the host-rock successions to volcanic-hosted massive sulfide deposits: Economic Geology, v. 87, no. 3, p. 511–541.

Cassidy, KF, Champion, DC, McNaughton, NJ, Fletcher, IR, Whitaker, AJ, Bastrakova, IV and Budd, AR 2002, Characterization and metallogenic significance of Archaean granitoids of the Yilgarn Craton, Western Australia: Amira International Limited, AMIRA Project no. P482/MERIWA Project M281 (unpublished report no. 222).

Clifford, BA 1992, Facies and palaeoenvironment analysis of the Archaean volcanic-sedimentary succession hosting the Golden Grove Cu–Zn massive sulphide deposits, Western Australia: Monash University, PhD thesis (unpublished), 343p.

Costa, UR, Barnett, RL and Kerrich, R 1983, The Mattami Lake Mine Archean Zn–Cu sulfide deposit, Quebec: hydrothermal coprecipitation of talc and sulfides in a sea-floor brine pool – evidence from geochemistry, $^{18}O/^{16}O$, and mineral chemistry: Economic Geology, v. 78, p. 1144–1203.

Dickson, JAD 1965, A modified staining technique for carbonates in thin section: Nature, v. 205, p. 587–587, doi 10.1038/205587a0.

Elliot-Meadows, SR, Froese, E and Appleyard, EC 1999, Cordierite–anthophyllite–cummingtonite rocks from the Lar deposit, Laurie Lake, Manitoba: Canadian Mineralogist, v. 37, p. 375–380.

Empire Resources Ltd 2009a, First resource estimate for Yuinmery copper–gold project in WA: Report to Australian Securities Exchange, 18 March 2009, 6p.

Empire Resources Ltd 2009b, Multiple copper zones in Empire's first hole in new WA drill schedule at Yuinmery: Report to Australian Securities Exchange, 14 December 2009, 4p.

Empire Resources Ltd 2010a, Quarterly report for the period ending 31 March 2010: Report to Australian Securities Exchange, 30 April 2010, 12p.

Empire Resources Ltd 2010b, Quarterly report for the period ending 30 June 2010: Report to Australian Securities Exchange, 27 July 2010, 9p.

Empire Resources Ltd 2011a, First high grade zinc mineralization discovered at Empire's A Zone prospect at Yuinmery Project, WA: Report to Australian Securities Exchange, 14 July 2011, 4p.

Empire Resources Ltd 2011b, Quarterly report for the period ending 31 December 2010: Report to Australian Securities Exchange, 28 January 2011, 12p.

Empire Resources Ltd 2012, Annual report 2012: Report to Australian Securities Exchange, 23 October 2012, 77p.

Evans, BW and Ghiorso, MS 1995, Thermodynamics and petrology of cummingtonite: American Mineralogist, v. 80, p. 649–663.

Ferguson, KM 1999, Lead, zinc and silver deposits of Western Australia: Geological Survey of Western Australia, Mineral Resources Bulletin 15, 314p.

Floran, RJ and Papike, JJ 1978, Mineralogy and petrology of the Gunflint iron formation, Minnesota–Ontario: Correlation of compositional and assemblage variations at low to moderate grade: Journal of Petrology, v. 19, no. 2, p. 215–288.

Franklin, JM, Gibson, HL, Jonasson, IR and Galley, AG 2005, Volcanogenic massive sulfide deposits, *in* Economic Geology 100th Anniversary Volume *compiled by* JW Hedenquist, JFH Thompson, RJ Goldfarb and JP Richards: Society of Economic Geologists, Littleton, Colorado, p. 523–559.

Frater, KM 1978, The Golden Grove copper–zinc deposit, Western Australia — an Archaean, exhalative, volcanogenic occurrence: The University of Newcastle, Newcastle, New South Wales, PhD thesis (unpublished), 177p.

Gale, GH, Dabek, LB and Fedicow, MAF 1997, The application of rare earth element analyses in the exploration for volcanogenic massive sulfide type deposits: Exploration and Mining Geology, v. 6, no. 3, p. 233–252.

Galley, AG, Hannington, MD and Jonasson, IR 2007, Volcanogenic massive sulphide deposits, *in* A synthesis of major deposit-types, district metallogeny, the evolution of geological provinces, and exploration methods *edited by* WD Goodfellow: Geological Association of Canada, Mineral Deposits Division, Special Publication 5, p. 141–161.

Gibson, HL and Galley, AG 2007, Volcanogenic massive sulphide deposits of the Archean, Noranda district, Quebec, *in* Mineral deposits of Canada: a synthesis of major deposit-types, district metallogeny, the evolution of geological provinces, and exploration methods *edited by* WD Goodfellow: Geological Association of Canada, Special Publication 5, p. 533–552.

Gibson, HL and Kerr, DJ 1993, Giant volcanic-associated massive sulfide deposits: with emphasis on Archean examples, *in* Giant ore deposits *edited by* BH Whiting, CJ Hodgson and R Mason: Society of Economic Geologists, Special Publication 2, p. 319–348.

Gibson, HL, Morton, RL and Hudak, GJ 1999, Submarine volcanic processes, deposits, and environments favourable for the location of volcanic-associated massive sulfide deposits, *in* Volcanic-hosted massive sulfide deposits: processes and examples in modern and ancient settings *edited by* CT Barrie and MD Hannington: Society of Economic Geologists, Reviews in Economic Geology 8, p. 13–51.

Green, AA, Schlodlok, M and Huntington, J 2012, Interpretation of thermal infrared HyLogger data: progress and challenges, *in* Proceedings 34th International Geological Congress — Unearthing our past and future *edited by* I Lambert and AC Gordon: Carillon Conference Management Pty Ltd; Brisbane, 5 August 2012, p. 3868.

Guilliamse, JN 2013, Investigation into the potential for volcanic-associated massive sulphide mineralisation at Weld Range by using Golden Grove as a comparative model: The University of Western Australia, Perth, MSc thesis (unpublished), 109p.

Hancock, EA, Green, AA, Huntington, JF, Schodlok, MC and Whitbourn, LB 2013, HyLogger-3: implications of adding thermal-infrared sensing: Geological Survey of Western Australia, Record 2013/3, 24p.

Hannington, MD, de Ronde, CEJ and Petersen, S 2005, Sea-floor tectonics and submarine hydrothermal systems, *in* Economic Geology 100th Anniversary Volume *edited by* JW Hedenquist, JFH Thompson, RJ Goldfarb and JP Richards: Society of Economic Geologists, Littleton, Colorado, p. 111–141.

Hassan, LY 2012, VMS projects — Murchison and Southwest (poster): Geological Survey of Western Australia; GSWA Open Day, Perth, 22 February 2012.

Herrmann, W, Blake, M, Doyle, M, Huston, D, Kamprad, J, Merry, N and Pontual, S 2001, Short wavelength infrared (SWIR) spectral analysis of hydrothermal alteration zones associated with base metal sulfide deposits at Rosebery and Western Tharsis, Tasmania, and Highway-Reward, Queensland: Economic Geology, v. 96, no. 5, p. 939–955.

Herzig, PM, Hannington, MD and Arribas, A 1998, Sulfur isotopic composition of hydrothermal precipitates from the Lau back-arc: implications for magmatic contributions to seafloor hydrothermal systems: Mineralium Deposita, v. 33, p. 226–237.

Ivanic, TJ, Wingate, MTD, Kirkland, CL, Van Kranendonk, MJ and Wyche, S 2010, Age and significance of voluminous mafic–ultramafic magmatic events in the Murchison Domain, Yilgarn Craton: Australian Journal of Earth Sciences, v. 57, p. 597–614.

Jenner, GA 1996, Trace element geochemistry of igneous rocks: geochemical nomenclature and analytical geochemistry, *in* Trace element geochemistry of volcanic rocks: application for massive sulphide exploration *edited by* DA Wyman: Geological Association of Canada, Short Course Notes 12, p. 51–77.

Kerrich, R and Said, N 2011, Extreme positive Ce-anomalies in a 3.0 Ga submarine volcanic sequence, Murchison Province: oxygenated marine bottom waters: Chemical Geology, v. 280, no. 1, p. 232–241.

Kerrich, R and Wyman, DA 1997, Review of developments in trace-element fingerprinting of geodyndamic settings and their implications for mineral exploration: Australian Journal of Earth Sciences, v. 44, no. 4, p. 465–487.

Le Maitre, RW (editor) 2002, Igneous rocks: a classification and glossary of terms, Recommendations of the International Union of Geological Sciences Subcommission on the Systematics of Igneous Rocks (2nd edition): Cambridge University Press, New York, 236p.

McLeod, RL, Gabell, AR, Green, AA and Gardavski, V 1987, Chlorite infrared spectral data as proximity indicators of volcanogenic massive sulphide mineralisation, *in* Proceedings: Pacific Rim Congress 87, Gold Coast, Queensland, 26 August 1987, p. 321–324.

McLeod, RL and Stanton, RL 1984, Phyllosilicates and associated minerals in some Paleozoic stratiform sulfide deposits of Southeastern Australia: Economic Geology, v. 79, p. 1–22.

Metals Australia Ltd 2008, Manindi zinc project – JORC upgrade: Report to Australian Stock Exchange (ASX), 25/03/2008, 7p.

MMG Golden Grove Pty Ltd 2012, Scuddles and Gossan Hill Archaean VHMS deposits (report): 36p (unpublished).

Morin-Ka, S 2012, Hyperspectral characterization of rare earth minerals: Geological Survey of Western Australia, Record 2012/12, 50p.

Morris, PA 2007, Composition of the Bunbury Basalt (BB1) and Kerba Monzogranite (KG1) geochemical reference materials, and assessing the contamination effects of mill heads: Geological Survey of Western Australia, Record 2007/14, 22p.

Mueller, WU, Stix, J, Corcoran, PL and Daigneault, R 2009, Subaqueous calderas in the Archean Abitibi greenstone belt: an overview and new ideas: Ore Geology Reviews, v. 35, no. 1, p. 4–46.

O'Connor, CK 1971, Freddie Well Joint Venture summary report of exploration February–August 1971 zinc–copper prospect Youanmi, WA; Conwest (Australia) NL: Geological Survey of Western Australia, Statutory mineral exploration report, A3885 (unpublished).

Pan, Y and Fleet, ME 1995, Geochemistry and origin of cordierite–orthoamphibole gneiss and associated rocks at an Archean volcanogenic massive sulphide camp: Manitouwadge, Ontario, Canada: Precambrian Research, v. 74, p. 73–89.

Pearce, JA 1996, A users guide to basalt discrimination diagrams, *in* Trace element geochemistry of volcanic rocks: applications for massive sulphide exploration *edited by* DA Wyman: Geological Association of Canada, Short Course Notes 12, p. 79–113.

Pearce, JA 2008, Geochemical fingerprinting of oceanic basalts with applications to ophiolite classification and the search for Archean oceanic crust: Lithos, v. 100, p. 14–48.

Pearce, JA and Cann, J 1971, Ophiolite origin investigated by discriminant analysis using Ti, Zr and Y: Earth and Planetary Science Letters, v. 12, p. 339–349.

Pearce, JA and Cann, J 1973, Tectonic setting of basic volcanic rocks determined using trace element geochemistry: Earth and Planetary Science Letters, v. 19, p. 290–300.

Pearce, JA, Stern, RJ, Bloomer, SH and Fryer, P 2005, Geochemical mapping of the Mariana arc-basin system: implications for the nature and distribution of subduction components: Geochemistry Geophysics Geosystems, v. 6, no. 7, p. 1–27.

Piercey, SJ 2011, The setting, style, and role of magmatism in the formation of volcanogenic massive sulfide deposits: Mineralium Deposita, v. 46, no. 5, p. 449–471.

Pontual, S 2008, GMEX spectral analysis guides for mineral exploration (3rd edition): AusSpec International Ltd, Australia, 10 vols.

Richards, AL and Elliot, PJ 1983, Smith Well Project, Final Surrender Report for the period 01/07/1981 to 31/01/1983, MC57/4649–4650, 475–4760, 4994–5008, 5011–5012, 5013–5021; Shell Company of Australia: Geological Survey of Western Australia, Statutory mineral exploration report, A12137 (unpublished).

Ridler, RH 1971, Analysis of Archean volcanic basins in the Canadian Shield using the exhalite concept: Canadian Institute of Mining and Metallurgy Bulletin, v. 64, no. 714, p. 20.

Roberts, RG and Rearden, EJ 1978, Alteration and ore-forming processes at Mattagami Lake Mine, Quebec: Canadian Journal of Earth Sciences, v. 15, p. 1–21.

Rollinson, HR 1993, Using geochemical data: evaluation, presentation, interpretation: Pearson Education Ltd, Harlow, 352p.

Sangster, DF 1972, Precambrian volcanogenic massive sulphide deposits in Canada: a review: Department of Energy and Resources, Ottawa, 44p.

Sangster, DF 1978, Exhalites associated with Archaean volcanogenic massive sulfide deposits, *in* Archaean cherty metasediments: their sedimentology, micropalaeontology, biogeochemistry and significance to mineralization *edited by* JE Glover and DI Groves: Extension Service, The University of Western Australia, Perth, Publication No. 2, p. 70–75.

Silver Lake Resources Ltd 2012, Copper exploration update: Report to Australian Stock Exchange, 15 June 2012, 10p.

Silver Swan Group Limited 2010, March Quarterly Activities Report: Report to Australian Securities Exchange, 30 March 2010, 5p.

Simmons, EC, Lindsley, DH and Papike, JJ 1974, Phase relations and crystallization sequence in a contact metamorphosed rock from the gunflint iron formation, Minnesota: Journal of Petrology, v. 15, p. 539–565.

Simpson, ES 1920, Hisingerite: Proceedings of the Royal Society of Western Australia, v. 5, p. 95–97.

Slack, JF 2012, Exhalites in volcanogenic massive sulfide occurrence model: US Geological Survey Scientific Investigations Report 2010-5070, no. 10, p. 159–163.

Stern, RJ 2005, Evidence from ophiolites, blueschists, and ultra high-pressure metamorphic terranes that the modern episode of subduction tectonics began in Neoproterozoic time: Geology, v. 33, p. 557–560.

Stevens, G, Moyen, J-F and Lana, C 2010, The metamorphic record of a paleoarchean crustal collision, *in* Fifth International Archean Symposium abstracts *edited by* IM Tyler and CM Knox-Robinson: Geological Survey of Western Australia; Fifth International Archean Symposium, Perth, 5 September 2010; Record 2010/18, p. 158–160.

Stewart, AJ, Williams, IR and Elias, M (compilers) 1983, Youanmi, Western Australia: Geological Survey of Western Australia, 1:250 000 Geological Series Explanatory Notes, 58p.

Sun, S-S and McDonough, WF 1989, Chemical and isotopic systematics of oceanic basalts: implications for mantle compositions and processes, *in* Magmatism in the Ocean Basins *edited by* AD Saunders and MJ Norry: Geological Society, London, Special Publication 42, p. 313–345.

Swinden, HS 1996, The application of volcanic geochemistry to the metallogeny of volcanic-hosted sulphide deposits in central Newfoundland, *in* Trace element geochemistry of volcanic rocks: application for massive sulphide exploration *edited by* DA Wyman: Geological Association of Canada, Short Course Notes 12, p. 329–358.

Vallance, TG 1967, Mafic rock alteration and isochemical development of some cordierite–anthophyllite rocks: Journal of Petrology, v. 8, p. 84–96.

Van Kranendonk, MJ 2010, Two types of Paleoarchean continental crust: oceanic-type plateaux and subdiction zone collages on early earth, *in* Fifth International Archean Symposium *edited by* IM Tyler and CM Knox-Robinson: Geological Survey of Western Australia; Fifth International Archean Symposium, Perth, 5 September 2010, Record 2010/18, p. 161–164.

Van Kranendonk, MJ 2011, Nowthanna, WA Sheet 2643: Geological Survey of Western Australia, 1:100 000 Geological Series.

Van Kranendonk, MJ, Ivanic, TJ, Wingate, MT, Kirkland, CL and Wyche, S 2013, Long-lived, autochthonous development of the Archean Murchison Domain, and implications for Yilgarn Craton tectonics: Precambrian Research, v. 229, p. 49–92.

Van Kranendonk, MJ, Ivanic, TJ, Wyche, S, Wilde, SA and Zibra, I (compilers) 2010, A time transect through the Hadean to Neoarchean geology of the western Yilgarn Craton — a field guide: Geological Survey of Western Australia, Record 2010/19, 69p.

Wang, Q, Schiøtte, L and Campbell, IH 1998, Geochronology of supracrustal rocks from the Golden Grove area, Murchison Province, Yilgarn Craton, Western Australia: Australian Journal of Earth Sciences, v. 45, p. 571–577.

Watkins, KP 1990, Yuinmery Joint Venture Annual Report 31/01/89–30/01/90 P/3/90; RGC Exploration Pty Ltd: Geological Survey of Western Australia, Statutory mineral exploration report, A29489 (unpublished).

Watkins, PJ and Nolan, J 1990, Determination of rare earth elements, scandium, yttrium and hafnium in 32 georeference materials using inductively coupled plasma-atomic emmission spectometry: Geostandards Newsletter, v. 14, p. 11–20.

Western Mining Corporation Ltd 1973a, Yuinmery Project, Percussion Drilling Data, MC57/365–368, 458–468 & 470–476; Western Mining Corporation Ltd: Geological Survey of Western Australia, Statutory mineral exploration report, A4270 (unpublished).

Western Mining Corporation Ltd 1973b, Annual tenements report 1972/73 Pincher Well Mineral Claims; Western Mining Corporation Ltd: Geological Survey of Western Australia, Statutory mineral exploration report, A4394 (unpublished).

Western Mining Corporation Ltd 1973c, Pincher Well – Youanmi M.C. Diamond drilling logs and assay data; Western Mining Corporation Ltd: Geological Survey of Western Australia, Statutory mineral exploration report, A4395 (unpublished).

Wilson, AF 1952, Occurence of metasomatic hypersthene, and its petrographic significance: American Mineralogist, v. 37, p. 633–636.

Winchester, JA and Floyd, PA 1977, Geochemical discrimination of different magma series and their differentiation products using immobile elements: Chemical Geology, v. 20, p. 325–343.

Wingate, MTD, Kirkland, CL and Ivanic, TJ 2012, 194751: metadolerite, Freddie Well; Geochronology Record 1015: Geological Survey of Western Australia, 4p.

Wood, DA 1980, The application of a Th–Hf–Ta diagram to problems of tectonomagmatic classification and to establishing the nature of crustal contamination of basaltic lavas of the British Tertiary volcanic province: Earth and Planetary Science Letters, v. 50, p. 11–30.

Wood, DA, Joron, J-L and Treuil, M 1979, A re-appraisal of the use of trace elements to classify and discriminate between magma series erupted in different tectonic settings: Earth and Planetary Science Letters, v. 45, p. 326–336.

Wroe, JA 1976, Yuinmery Prospect, Annual Report for the period 01/07/1974 to 29/06/1976, Mineral Claims 365B–368B, 58/2726, 2727, 2733, 2788, 2910–2929 and 4151–4168; Western Mining Corporation Ltd: Geological Survey of Western Australia, Statutory mineral exploration report, A6865 (unpublished).

Wroe, JA 1978, Yuinmery Project, Non-statutory Report: Annual Report for the period 30/06/1976 to 13/121977, MC57/365–368, 458–460, 462–464, 466–468, 2726–2727, 2733–2734 & 4151–4168; Western Mining Corporation: Geological Survey of Western Australia, Statutory mineral exploration report, A7475 (unpublished).

Wyche, S, Ivanic, T and Zibra, I (compilers) 2013, Youanmi and southern Carnarvon seismic and magnetotelluric (MT) workshop (preliminary edition): Geological Survey of Western Australia, Record 2013/6, 171p.

Wyman, DA and Kerrich, R 2012, Geochemical and isotopic characteristics of Youanmi terrane volcanism: the role of mantle plumes and subduction tectonics in the western Yilgarn Craton: Australian Journal of Earth Sciences, v. 59, no. 5 (Archean evolution — Yilgarn Craton), p. 671–694, doi:10.1080/08120099.2012.702684.

The Yuinmery project, which includes the Just Desserts deposit and several other prospects, is one of several Archean volcanogenic massive sulfide (VMS) projects in the Murchison region being studied by the Mineral Exploration section of the Geological Survey of Western Australia (GSWA). The aim is to build genetic models for the environment of ore formation, and provide useful vectors for exploring in greenfields areas.

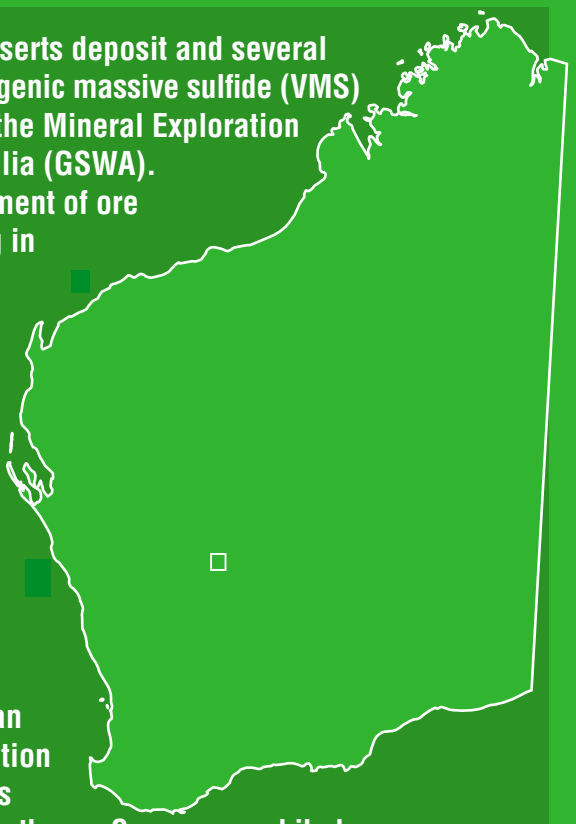

Conclusions are that deposition of mineralization at Yuinmery took place around hydrothermal vents on the sea floor and in fractures and voids in the rocks of the subsea floor accompanied by widespread precipitation of banded iron-formation (BIF) and chert during periods of relative volcanic quiescence. The Just Desserts deposit, Trajan prospect, and C Zone are at the same stratigraphic level and are underlain by calc-alkaline basalt and overlain by andesite. Trace element geochemistry suggests that the volcanic rocks were extruded in an oceanic arc-rift setting. Talc is the dominant alteration mineral proximal to mineralization while chlorite is abundant more distally. Localized patches of hypersthene, Ca-poor amphiboles (anthophyllite and cummingtonite), and cordierite are interpreted to have formed along fluid pathways by extremely hot hydrothermal fluids heated by underlying magma. The Yuinmery prospects are very different from the Golden Grove deposits, which are hosted by felsic volcanic rocks in a continental margin arc setting, and have chlorite and white mica as the dominant alteration minerals.

The HyLogger proved useful for studying the alteration assemblages. A portable HyLogger could be used on drillcore and cuttings in the field as an exploration tool to identify talc and Ca-poor amphiboles that could indicate proximity to mineralization. Trace element geochemistry indicative of an oceanic-arc setting and a change in volcanic composition are important regional vectors to mineralization of the Yuinmery type.

Further details of geological products and maps produced by the Geological Survey of Western Australia are available from:

Information Centre
Department of Mines and Petroleum
100 Plain Street
EAST PERTH WA 6004
Phone: (08) 9222 3459 Fax: (08) 9222 3444

www.dmp.wa.gov.au/GSWApublications

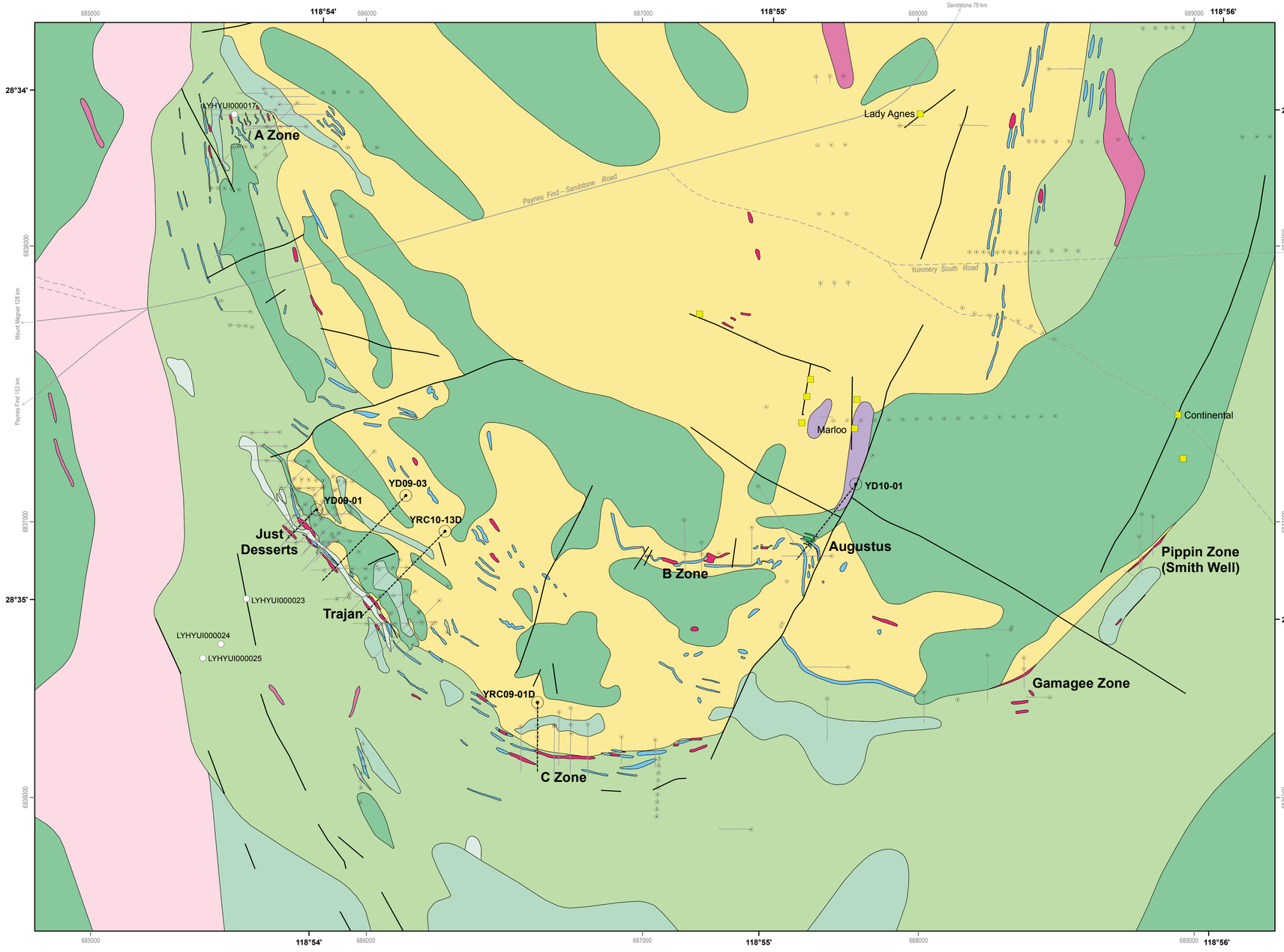

Courbaroo Tonalite
- Tonalite
- Dolerite
- Felsic porphyry

Ammeen Supersuite
- Granophyre
- Leucogabbro
- Gabbro
- Pyroxenite

Norie Group ?
- Upper volcanics
- Mineralization
- BIF/chert
- Lower volcanics

- Marloo — Gold workings
- Trajan — Prospect name
- YD10-01 — Diamond drillholes studied
- LYHYUI000023 — Sample sites
- Drilholes used
- Studied drillhole trace
- Drillhole trace
- Faults
- Road
- Track

Refer to GSWA Report 131 for further details

Compiled by L Hassan

Cartography by I Lesiak

Edited by M Ferland

Published by the Geological Survey of Western Australia

This map is published in digital format (PDF) and is available online at <www.dmp.wa.gov.au/GSWApublications>.
Copies are available from:
Information Centre
Department of Mines and Petroleum
100 Plain Street, East Perth WA 6004
Phone: +61 8 9222 3459 Fax: +61 8 9222 3444
Website: www.dmp.wa.gov.au/gswa Email: geological.survey@dmp.wa.gov.au

The recommended reference for this plate is:
Hassan, LY 2013, Interpreted geological map of the Yuinmery prospects showing drillholes and sample location, *in* The Yuinmery volcanogenic massive sulfide prospects: mineralization, metasomatism, and geology *by* LY Hassan: Geological Survey of Western Australia, Report 131, Plate 1.

Government of **Western Australia**
Department of **Mines and Petroleum**

HON. BILL MARMION MLA
MINISTER FOR MINES AND PETROLEUM

Geological Survey of Western Australia

RICK ROGERSON
EXECUTIVE DIRECTOR

0 250 500
Meters

UNIVERSAL TRANSVERSE MERCATOR PROJECTION
HORIZONTAL DATUM: GEOCENTRIC DATUM OF AUSTRALIA 1994
VERTICAL DATUM: AUSTRALIAN HEIGHT DATUM
MAP GRID AUSTRALIA ZONE 50

GEOLOGICAL SURVEY OF WESTERN AUSTRALIA

REPORT 131 PLATE 1

INTERPRETED GEOLOGICAL MAP OF THE YUINMERY PROSPECTS SHOWING DRILLHOLES AND SAMPLE LOCATIONS